Charged Hadron Distributions in 19.6-GeV Au+Au Collisions

By

ROPPON PICHA
B.S. Physics (University of California, Irvine) 2000
M.S. Physics (University of California, Davis) 2002

DISSERTATION

Submitted in partial satisfaction of the requirements for the degree of

DOCTOR OF PHILOSOPHY

in

Physics

in the

OFFICE OF GRADUATE STUDIES

of the

UNIVERSITY OF CALIFORNIA
DAVIS

Approved:

Committee in Charge

2005

Abstract

Charged Hadron Distributions in 19.6-GeV Au+Au Collisions

by

ROPPON PICHA

Experimental results from a low-energy heavy ion run in year 2001 at the Relativistic Heavy Ion Collider (RHIC) using the Solenoidal Tracker at RHIC (STAR) detector are presented. From the collisions of gold ions at $\sqrt{s_{\mathrm{NN}}} = 19.6$ GeV, six species of particles ($\pi^{\pm}$, $K^{\pm}$, p, and $\bar{p}$) are identified via energy loss mechanism and their transverse mass spectra are analyzed at midrapidity ($|y| < 0.5$) and $m_T - m_0 < 1.0$ GeV/c^2. Rapidity distributions, particle ratios, and hadronic freeze-out conditions are discussed. This study provides a low energy measurement at RHIC which is very close to that at the SPS for cross comparison between collider experiments and fixed target experiments. The analysis provides a good reference to study excitation functions of strangeness production, net baryon, and collective flow inside heavy ion collisions.

This thesis is dedicated to
Mom, Dad, and Aim.

Contents

List of Figures

List of Tables

Acknowledgements

I would like to express my deepest gratitude to everyone who helped me in this research, both intellectually and emotionally. I definitely could not have completed this work without your support.

I would like to thank Dr. Daniel Cebra for being my advisor for the last three and a half years. Thank you Daniel for providing me a place to learn and for guiding me through those important first steps in research. Thank you Dr. Juan Romero, for helping me get started in doing data analysis. You were always a great resource when I had questions. I thank Dr. Thomas Gutierrez and Dr. Jennifer Klay for being supportive, and for helping me prepare for the qualifying exam.

I would also like to thank Dr. Ramona Vogt, Dr. Jim Draper, and Dr. Paul Brady for the encouragement and advices they constantly provided me. Thank you Dr. Daniel Ferenc for being my first advisor when I arrived at the university and for chairing the committee of my oral exam, which was the most unique and intense experience I had in graduate school.

I gratefully acknowledge my dissertation committee: Dr. Brady, Dr. Cebra, and Dr. Draper, for carefully reviewing the drafts. Thank you very much for improving this thesis in many ways with your comments.

To my student colleagues: Stephen Baumgart, David Cherney, Orpheus Mall, Matthew Searle, Brooke Haag, and Daniel Collins, thank you for making the Nuclear Group a friendly and stimulating learning environment for all of us. It has been my pleasure to know you and work with you.

I would like to express my appreciation to the STAR Collaboration for having me as a part of their exciting scientific exploration. I thank especially the Spectra working group for their patience and guidance. I also want to acknowledge RHIC and STAR scientists and engineers, whose hard work made possible the high quality data for this analysis.

I would like to acknowledge the U.S. National Science Foundation for the research grant (PHY 99-71845) and the Royal Thai Government for the financial support throughout the entire length of my stay in the United States.

As I was trying to finish the thesis, my final months in Davis (and the U.S.) had been made much more enjoyable by my small circle of friends. There are several people I want to thank in particular. Monticha, thank you for your delicious meals. Nattapol and Siripoj, thanks for being my sports buddies. Tipawan, when you were not feeding me with your fine cooking, you entertained me with your forehands at the tennis courts. I thank you all, very much, for having shared many memorable experiences in Davis with me.

I also take this opportunity to thank my longtime friend, Piyanan Visartavakin, for simply being herself. Piyanan, you have a special ability to make me feel that everything is all right. Although many miles have kept us half the world apart, you have always been a quiet source of inspiration for me to stay positive and to overcome any obstacles in life.

Finally and most importantly, I would like to thank my family for their unwavering support. Without the love from my wonderful parents and sister, Aim, the completion of this long journey would not be possible. I look forward to being home.

Chapter 1

Introduction

This work presents the experimental results from the study of particle spectra from the collisions of Au+Au at center of mass energy of 19.6 GeV. In this chapter concepts relating to this study will be introduced. The thesis outline will be given at the end of the chapter.

1.1 Nuclear Physics Overview

When two nuclei collide at a very high energy, interesting things happen. Before we look into the collisions, we first review underlying physics of the nucleus.

All known freely-existing particles in our universe can be classified into three catagories: baryons, mesons, and leptons. An atom is a combination of baryons (protons and neutrons) and leptons (electrons). Mesons are unstable particles and are not part of everyday matter. The electron can escape if it has enough energy to overcome the electromagnetic force that binds it to the nucleus. This amount of energy is called the ionization energy. The first ionization energy is about 5-20 electron volts (eV) for most atoms. The nucleus, however, is much harder to break up. The energy that binds protons and neutrons is on the order of MeV. Nuclear physics is the study of the atomic nucleus.

Although it occupies a very small space inside an atom, the nucleus holds more than 99.9% of the atom's mass. As previously mentioned, the nucleus is made up of two types of baryons: protons (p) and neutrons (n), both of which are collectively called nucleons. Under current theory, both p and n are composed of even smaller constituents called quarks. Any particle containing quarks is called a hadron, the collective term for a baryon, which contains three quarks (qqq), and a meson, which is made of a quark and an antiquark ($q\bar{q}$). Any hadron can be modelled as a collection of different types of quarks, arranged in different orbits and spin orientations.

The proton is the lightest stable hadron with a radius of 0.895 ± 0.018 fm [36]. While a neutron is electrically neutral, a proton carries a charge of $+1e$, resulting in the nucleus being positively charged. Other types of baryons are highly unstable and eventually decay into protons or neutrons. While a free proton is stable, an unbound neutron has a lifetime of $\sim$ 887 seconds [37] and decays into a proton via a beta emission process ($n \rightarrow pe^{-}\bar{\nu}_{e}$).

At the present, quarks, whose existence was proposed in the 1960s, independently by Murray Gell-Mann and George Zweig [38, 39], and leptons are the most fundamental particles known to exist. A "strong" force between the quarks binds them together inside each hadron.

A nucleus can be characterized by its charge or atomic number Z (number of protons) and mass number A (number of protons plus neutrons). The radius of a nucleus with a mass number A can be estimated as $R \approx 1.2A^{1/3}$ fm.

To learn about properties of the nuclear matter, we break the nuclei apart by using a particle accelerator. When two nuclei collide at a high center-of-mass energy, some of the initial neutrons and protons will be vaporized and the interactions may result in products different from the initial nuclei. On an event-by-event basis, baryon number (number of baryons minus number of antibaryons) and charge, among other quantum numbers, will be conserved, as well as momentum and energy.

When we study a system (collision) producing something as small and as fast as particles from ultrarelativistic collisions, it is convenient to use the units that accommodate measurements. The units used in this study numerically and dimensionally set $c = \hbar = k_{\mathrm{B}} = 1$. In SI units, c (the speed of light in vacuum) is 3.0×10^8 m s^{-1}; $\hbar$ (the reduced Planck constant) is 1.054×10^{-34} J s; and k_{B} (the Boltzmann constant) is 1.380×10^{-23} J K^{-1}. The use of natural units simplify calculations. For example, the relativistic energy, $E = mc^2$ becomes $E = m$. $\hbar c$ ($= 197.3$ MeV $\cdot$ fm), which has dimensions of force × area (N $\cdot$ m^2) is also the unit of the electromagnetic fine structure constant (α) and is often used as a conversion factor. Under the equipartition theorem, each component of the kinetic energy of an ideal gas at the temperature T, $E \propto k_{\mathrm{B}}T$ becomes $E \propto T$. Under this system, 1 second is equivalent to 3.0×10^8 meters (a light second). One needs to keep in mind, however, that the ignored units must be put back in the final steps to obtain the actual results.

1.2 Nuclear Phase Transition

In terms of thermodynamics, an n$^{\mathrm{th}}$-order phase transition occurs when $\partial^n G/\partial T^n$ becomes discontinuous [40]. G is the Gibbs free energy, defined as: $G = U - TS + PV$, where U is internal energy, T is temperature, S is entropy, P is pressure, and V is volume. dG is a measure of the spontaneity of a process [1]. From $U = TS - PV + \mu N$, where μ is chemical potential, it follows that $dG = \mu N - S\,dT + V\,dP$. At a phase transition, the temperature (T_c) has to stay constant and the two phases have to have an equal pressure, $P_1(T_c) = P_2(T_c)$.

From these conditions, $dT = dP = 0$ and therefore, $dG = \mu\,dN$. It follows that at equilibrium ($dG = 0 = dG_1 + dG_2$) of a closed system ($dN_1 = -dN_2$), chemical potentials of the two phases must be equal as well: $\mu_1(T_c) = \mu_2(T_c)$

---

[1] A spontaneous process gives off energy and has $dG < 0$.

Water is a familiar example of matter. At room temperature and pressure, water is in its liquid state. If heat is taken away from the water so that its temperature falls to its freezing point (273 K), water will turn into solid (ice). It can also turn to its gaseous state (steam) if the temperature reaches its boiling point (373 K). Water can also change phases by a change in pressure. At the phase change, the temperature does not keep increasing or decreasing. Instead, the energy being added or removed from the system goes into overcoming the latent heat of fusion at the melting point or of vaporization at the boiling point.

Likewise, nuclear matter also exhibits changes in phase via changes in temperature or pressure. The conditions at which nuclear matter changes phases, however, are much more extreme. Unlike water for which we have ways to directly measure its temperature, using a thermometer, and pressure, using a barometer, to understand what goes on inside the nuclear collisions we have to make use of observables such as properties of the produced particles and shapes of their energy distributions.

1.3 Quantum Chromodynamics

Elementary particles and their interactions are governed by the Standard Model [41]. The fundamental forces can be described by unitary groups of different dimensions: $U(1) \times SU(2) \times SU(3)$. Numbers 1, 2, and 3 correspond to the dimensions of the unitary matrices which represent the groups. Physically, 3 in $SU(3)$ stands for the three colors. $U(1)$ and $SU(2)$ combine to describe the electromagnetic and weak interactions. $SU(3)$ is the gauge group of the strong interactions known as quantum chromodynamics (QCD). In this section the QCD framework will be introduced.

Nucleons are bound inside the nucleus via the strong interaction, which is also called the "color" force, for a reason which will be described shortly. This type of interaction is described by the QCD theory in which quarks and antiquarks of different flavors ("species" of quarks) exchange gluons which carry color charges.

The mediator (force carrying particles) of the electromagnetic interactions is the photon (γ). For the weak interactions, the mediators are W^+, W^-, and Z^0 bosons. The weak and electromagnetic interactions can be collectively described by the electroweak model [42]. Gluons mediate the strong interactions. Like other mediators, gluons are bosons with a spin of 1. Feynman diagrams of the fundamental interactions are shown in Figure 1.1 [2].

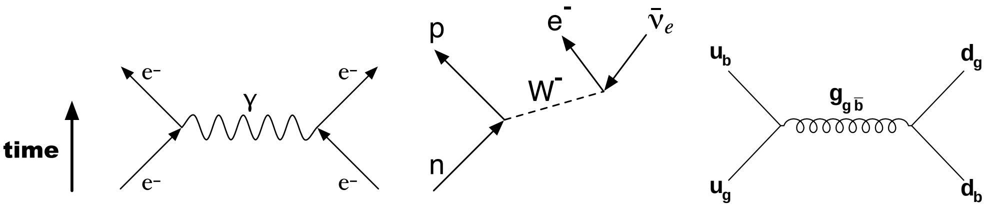

Figure 1.1. Feynman diagrams representing fundamental interactions between particles. From left to right: electromagnetic, weak, and strong.

The nuclei of all the existing matter around us consist of nucleons containing up (u) and down (d) quarks–the two lightest members of the quark family. If the energy is high enough, production channels of other flavors become available and more exotic hadrons can be produced. The other flavors are called charm or center (c), strange or sideways (s), top or truth (t), and bottom or beauty (b). Each of the quarks carries a fractional electric charge. The lightest of these four heavy flavors is the strange quark which has identical charge ($-1/3$) to the down quark. Each quark possesses a baryon number of $+1/3$ and a spin quantum number of $1/2$. The properties of the six quarks are summarized in Table 1.1.

According to the Pauli Exclusion Principle, two fermions (particles with half-integral spin) with identical quantum numbers cannot be in the same state or form a single system. The Ω^- baryon (mass = 1.672 GeV/c^2, spin = $+3/2$) is made of

---

[2] Note: For the strong interaction, 3-gluon and 4-gluon vertices are also possible.

flavor	year	charge (e)	I_3	mass (GeV/c^2) [43]
up	-	$+2/3$	$+1/2$	0.0015-0.0040
down	-	$-1/3$	$-1/2$	0.004-0.008
strange	1947	$-1/3$	0	0.080-0.130
charm	1974	$+2/3$	0	1.15-1.35
bottom	1977	$-1/3$	0	4.1-4.9
top	1995	$+2/3$	0	$178.1^{+10.4}_{-8.3}$

Table 1.1. Properties of quarks and the years of their discoveries.

three strange quarks, each with a spin +1/2. This system provides a motivation for the existence of an extra quantum number besides flavor, spin, and orbital angular momentum. Two other spin-3/2 baryons, the Δ^{++} (uuu) and Δ^{-} (ddd) also present the same dilemma. Therefore, the quarks have to possess a property that distinguishes them from each other and such property must have at least three different values. Color was therefore proposed to be the new quark label.

A strong evidence for quark colors comes from electron-positron annihilation ($e^-e^+ \to \ldots$) experiments. The cross section ratio (the hadronic R-ratio) is defined as

$$R \equiv \frac{\sigma(e^+e^- \to \text{hadrons})}{\sigma(e^+e^- \to \mu^+\mu^-)} \tag{1.1}$$

R is proportional to the sum of the squares of quark charges, $R = (\#\text{ colors}) \times \sum_i q_i^2$ [44]. The experimental results of R as a function of $\sqrt{s}$ [3] are shown in Figure 1.2.

Let's consider the energy range where u, d, and s quarks exist (the first plateau in Figure 1.2, from $\sqrt{s} \approx$ 2-3.5 GeV), where $R = 2$,

$$\begin{aligned} R &= (\#\text{ colors}) \times (q_u^2 + q_d^2 + q_s^2) && (1.2)\\ &= (\#\text{ colors}) \times \left(\left(\frac{2}{3}\right)^2 + \left(-\frac{1}{3}\right)^2 + \left(-\frac{1}{3}\right)^2\right) && (1.3)\\ &= (\#\text{ colors}) \times \frac{2}{3} && (1.4)\end{aligned}$$

Thus, for $R = 2$, the number of colors have to be 3.

---

[3] s is defined as $s = (p_1 + p_2)^2$, where p_1 and p_2 are the four-momenta of the incoming projectiles.

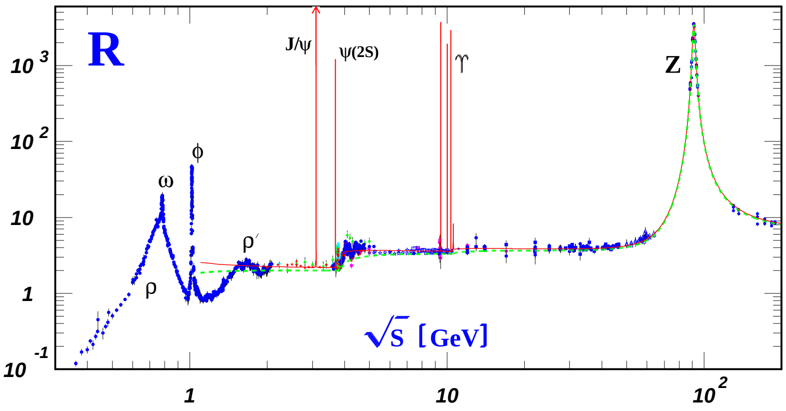

Figure 1.2. The ratio of the cross sections between $e^+e^- \rightarrow q\bar{q}$ and $e^+e^- \rightarrow \mu^+\mu^-$ [1].

The three colors used to describe quarks are red (r), green (g), and blue (b). A quark carries one of these three colors. An antiquark carries either anti-red ("cyan"), anti-green ("fuchsia"), or anti-blue ("yellow"). All of the hadrons must be color neutral (no net color)–that is, rgb or $\bar{r}\bar{g}\bar{b}$ for a baryon and $r\bar{r}$, $g\bar{g}$, or $b\bar{b}$ for a meson. This color neutrality in fact applies to leptons as well, in some sense, since leptons carry no colors. Thus, all observed particles in nature are color neutral (colorless).

There are eight different types of gluons, each characterized by the color and anticolor that the gluon carries. Gluons can thus change the color of a quark, but not its charge or flavor. For example, when a red up quark absorbs a blue/anti-red gluon, it will turn into a blue up quark. The color exchange is the underlying principle of the strong interaction.

The gluon exchange is analogous to the electromagnetic interaction between charged particles, governed by quantum electrodynamics (QED) theory. In QCD, color plays the role of QED charge. One of the distinctions between QED and QCD is that, while the photon of QED is neutral, the QCD gluons have color charges. As a result, all QED processes can be reduced to an elementary Feynman diagram of a charged particle entering a vertex (interaction point), emitting a photon, and exiting. Photons cannot interact with itself. In QCD, however, direct gluon-gluon coupling is also possible [44].

QCD interactions can be described by the following Lagrangian density [43]:

$$\mathcal{L}_{\mathrm{QCD}} = -\frac{1}{4}F^{(a)}_{\mu\nu}F^{(a)\mu\nu} + i\sum_q \bar{\psi}^i_q \gamma_\mu (D_\mu)_{ij}\psi^j_q - \sum_q m_q \bar{\psi}^i_q \psi_{qi} \tag{1.5}$$

In equation (1.5), m_q are the quark masses. The field strength tensor and covariant derivative are defined as

$$F^{(a)}_{\mu\nu} = \partial_\mu A^a_\nu - \partial_\nu A^a_\mu - g_s f_{abc} A^b_\mu A^c_\nu \tag{1.6a}$$

$$(D_\mu)_{ij} = \delta_{ij}\partial_\mu + i g_s \sum_a \frac{\lambda^a_{i,j}}{2} A^a_\mu \tag{1.6b}$$

g_s is the QCD coupling constant, f_{abc} $(a, b, c = 1, 2, \ldots, 8)$ are the $SU(3)$ structure constants related to commutation relations of the Gell-Mann λ matrices, $\psi^i_q(x)$ are the Dirac four-spinors for each quark field of color i and flavor q, and $A^a_\mu(x)$ are the Yang-Mills (gluon) fields.

From the definitions of the variables, we can see that the first term of $\mathcal{L}_{\mathrm{QCD}}$ describes gluons, the second term has to do with quark kinetic energy and quark-gluon interaction, and the last term corresponds to quark masses.

Quantum chromodynamics obeys local gauge symmetry. That is, the action $S_{\mathrm{QCD}} \equiv \int d^4x\, \mathcal{L}_{\mathrm{QCD}}$ (which determines the physical aspect of the theory) remains unchanged when the color fields are changed independently at any point in space-time, for example, $\psi(x) \to e^{i\alpha(x)}\psi(x)$, where α serves as the rotation angle.

The third term of $F^{(a)}_{\mu\nu}$ in equation (1.6a) makes possible gluon self-interactions and make QCD "non-Abelian" [45]. (Mathematically speaking, this means that the generators of the QCD SU(3) group (λ's) do not commute.) This property is what distinguishes QCD and QED. In QED, an Abelian theory, the mediators (photons) do not carry the (electric) charge themselves and thus cannot interact among themselves.

Unique characteristics of quantum chromodynamics are contained within the dimensionless effective coupling constant ($\alpha_s = {g_s}^2/4\pi$)–a parameter which determines the strength of the interaction [46]. (In a Feynman diagram, the coupling constant shows up at each vertex.) α_s is a running coupling constant (its magnitude depends on energy) whose first term is [43]

$$\alpha_s(Q) \propto \frac{1}{\beta_0 \ln(Q^2/\Lambda^2)} \tag{1.7}$$

$Q^2 = p^2_{\text{initial}} - p^2_{\text{final}}$. β_0 is the first term of the QCD beta function [4] and has a form of $\beta_0 = 11 - (2/3)n_f$ [47]; where n_f is the number of quarks with mass less than Q. Λ is the scale cutoff parameter, which sets the lower bound of the energy range where QCD can predict α_s, since $\alpha_s \to \infty$ when $Q^2 \sim \Lambda^2$. The value of Λ depends on the number of active quark flavors and the renormalization scheme [48].

The strong coupling constant becomes very large at larger distances ($d > 1$ fm) or small momentum transfer ($Q < 1$ GeV/c). This behavior of α_s is why we never see isolated quarks, since they are always confined within a hadron by the large coupling at large distance. If somehow the quarks are pulled far enough apart, the gluon string would be converted to quark-antiquark pair, resulting in two separate hadrons and confinement persists. At small distances or high momentum transfers [5] however, α_s becomes so small that quarks and antiquarks can roam free within the hadrons. This is a QCD nature called asymptotic freedom [49, 50], an idea that led to the 2004 Nobel Prize in Physics. Within this regime, partonic interactions are "perturbative," that is, the coupling constant is $\ll 1$ so few-vertices Feynman diagrams are dominant, and thus the processes are calculable. At longer distances, one can employ the lattice QCD approach, in which the space-time continuum is mapped down onto a grid [51].

The effective coupling constant (α_s) as a function of momentum transfer (Q), measured from various experiments, is shown in Figure 1.3.

Numerical calculations using lattice QCD [52, 53, 51] have predicted that under extreme conditions, a hadronic gas, where quarks and antiquarks are confined inside

---

[4] The beta function describes how the coupling constant varies with energy.

[5] In quantum mechanics, a small wavelength is associated with a large momentum.

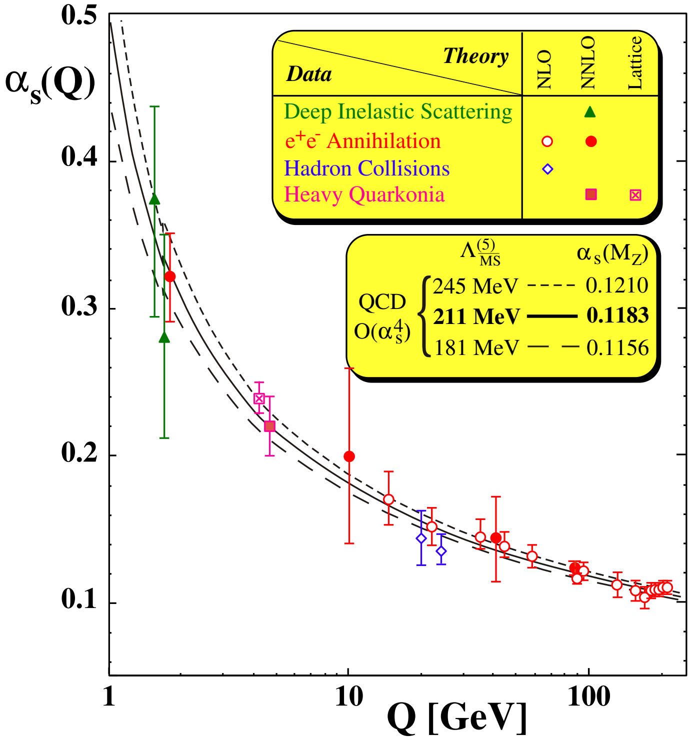

Figure 1.3. Strong coupling as a function of momentum transfer [2].

individual hadrons, will transition into a deconfined phase called the quark-gluon plasma (QGP). The STAR experiment descriptively defined the QGP as “a (locally) thermally equilibrated state of matter in which quarks and gluons are deconfined from hadrons, so that color degrees of freedom become manifest over nuclear, rather than merely nucleonic, volumes. [54]” For zero baryon density, this phase transition is expected to occur at a critical temperature $T_c \approx 175$ MeV.

Figure 1.4 shows the phase diagram of nuclear matter. The lower left (low temperature, low density) is the hadronic matter region, the upper right (high temperature, high density) is the plasma phase. The black semicircle on the horizontal axis (at $\mu_B =$ nucleon mass) represents normal nuclear matter. The black rectangular to the right represents conditions inside neutron stars, where density inside the core can be several times the density of an atomic nucleus. The phase diagram also indicates one of the phenomena predicted to occur at the phase transition: the restoration of “chiral" [6] symmetry. The restoration of chiral symmetry happens when quarks become massless [7]. When this happens, $\mathcal{L}_{\mathrm{QCD}}$ is invariant under independent rotations of left- and right-handed quark fields [55, 56].

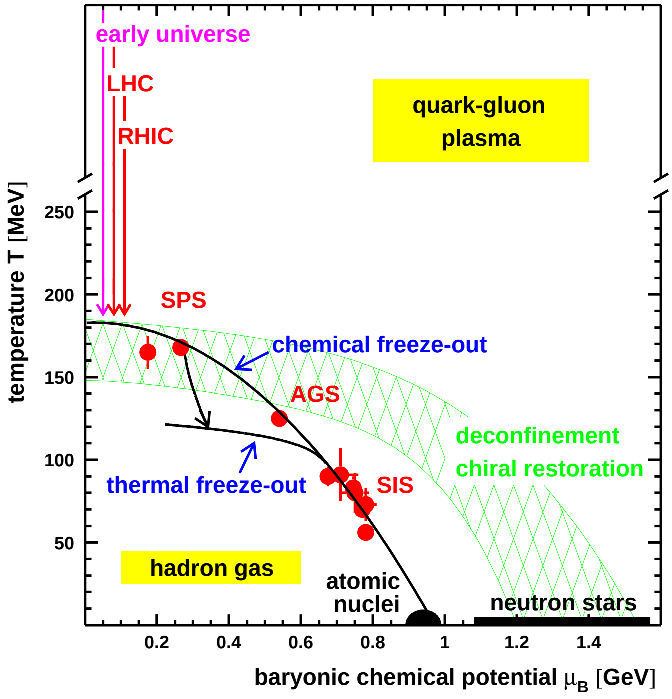

Figure 1.4. Nuclear phase diagram [3]. The hatched band is the expectation of the phase boundary based on lattice QCD calculations. Points and arrows with accelerator programs (LHC, RHIC, SPS, AGS, SIS) indicate freeze-out regions from data analyses and predictions.

1.4 Relativistic Heavy Ion Collisions

Throughout history, physicists have always tried to explore the fundamental constituents–the smallest ingredients–of things around us. For quite some time, the atom was

---

[6] The term "chiral" was first coined by Lord Kelvin (William Thomson). A geometrical object is chiral if it cannot be superimposed on its own mirror image. In QCD context, chirality refers to handedness of quarks.

[7] Unique handedness requires speed $= c$ (so mass $= 0$).

believed to be indivisible until Joseph J. Thomson discovered the electron and determined its charge-to-mass ratio in 1897 by studying the electric and magnetic forces on cathode rays. After the electron discovery, it was realized that there must be some positively charged particles inside the atom to balance the negative charge but nobody was quite sure what it was.

In 1911, Ernest Rutherford reconstructed the model of the atom from the scattering of α-particles ($^4\mathrm{He}^{2+}$) from a thin gold foil, performed by Hans Geiger and Ernest Marsden. Geiger and Marsden found that alpha particles were sometimes deflected at large angles. From this experiment, the nucleus was discovered and its size was estimated. Also in 1911, Robert Andrews Millikan, carrying on Thomson's result, precisely measured the charge of the electron by studying the motion of charged oil droplets inside an electric field.

After a series of experiments of transmuting one atom to another, Rutherford discovered that hydrogen nuclei were emitted. It appeared that every atomic nucleus consists of an integral number of charges in the hydrogen nuclei. The term "proton" was coined by Rutherford in early 1920s to refer to this fundamental nucleus. The determination of the atomic nucleus family was complete in 1932 when James Chadwick discovered the neutron by studying the scattering of beryllium nuclei ($^9\mathrm{Be}^{4+}$) and α particles with an ionization counter and a cloud chamber [57].

The goal of relativistic heavy ion experiments is also to understand the evolution phases and building blocks of the universe. From the alpha scattering experiments, Rutherford established that the diameter of the nucleus is of the order of 10^{-14} m. This scale is much too small for direct observations using the microscopes. As an indirect method, nuclear collisions are used as a tool to investigate into the internal structure of the nuclei at both hadronic (baryons and mesons) and partonic (quarks and gluons) levels. By accelerating two heavy nuclei to ultrarelativistic speeds and then colliding them, extreme conditions can be created inside a laboratory. In such high energy density conditions, we look for a formation of the QGP state. In this new state of matter where quarks and gluons are no longer confined, we could learn how these fundamental particles interact.

Another significance of the QGP study is the understanding of the early universe. The QGP is believed to be the state of the universe microseconds after the Big Bang, before hadronization occurred [58]. By looking into the high-energy nuclear collisions, we hope to have a glimpse of the universe billions of years ago. While the isotropy of cosmic microwave background (CMB) radiation implies that there was a hot Big Bang, it only takes us back to when the universe is a few hundred thousand years old and dilute enough that the primordial photons no longer scattered. There have been no hard evidences that the universe went through a phase transition from a QGP to hadrons, therefore if we could observe such transition in the laboratory, we may be able to understand the early universe better.

The evolution of a nucleon-nucleon collision in a nuclear collision can be conceptualized by Figure 1.5 [59]. In the diagram, the two incoming nuclei approach each other in $t < 0$ region and collide at $t = 0$. The system expands and cools as t increases. The state of matter that we look for is predicted to occur right after the pre-equilibrium but before the hadronization.

The spectra analysis is an important tool for studying the state and evolution of the nuclear matter at high energy density. Transverse mass spectra give us insights into how the energy and momentum of the produced particles are distributed as we look along the beam direction. The spectra contain the information about the system when elastic collisions stop. Majority of the particles are produced at low transverse momentum ($p_T < 1$ GeV/c). In this region, the analysis of particle spectra allow one to extract the bulk properties such as the degrees of thermalization and collectivity of the system.

In this analysis we take a look at the collisions of gold ions ($^{197}\mathrm{Au}^{79+}$). The center-

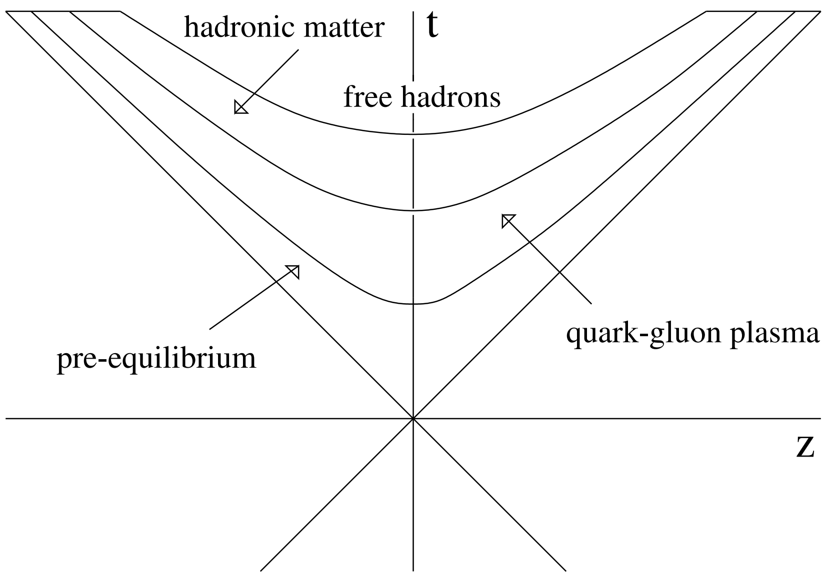

Figure 1.5. The evolution of a nuclear collision. z is the location along the beam direction. t is the proper time.

of-mass energy is $\sqrt{s_{\mathrm{NN}}} = 19.6$ GeV. s is a Mandelstam variable. The subscript NN indicates a system of two nucleons. s_{NN} is defined as a function of four-momentum (p),

$$\begin{aligned} s_{\mathrm{NN}} &= (p_1 + p_2)^2 \\ &= ((E_1 + E_2) - (\vec{p}_1 + \vec{p}_2))^2 \end{aligned} \tag{1.8}$$

The momentum vector sum is zero (in both lab frame and center-of-mass frame) for our symmetric system of Au+Au. Therefore, for $\sqrt{s_{\mathrm{NN}}} = 19.6$ GeV, the energy per nucleon, E_N, is 9.8 GeV (or 1.9 TeV per nucleus) [8]. We can approximate the relativistic γ factor to be $E_N/m_N = 10.5$ (m_N is the mass of a bound nucleon = 1 atomic mass unit (amu) = 0.9315 GeV/c^2). This gives us an idea of how much the nuclei (viewed from the lab frame) are contracted along the beam direction. Figure 1.6 shows the degrees of contraction between two different energies, 19.6 ($\gamma = 10.5$) and 200 GeV ($\gamma = 107.4$).

---

[8] In nuclear collisions the unit of the beam energy is sometimes denoted as AGeV, with A referring to the mass number. In this case of Au ion, 9.8 AGeV = 1.9 TeV.

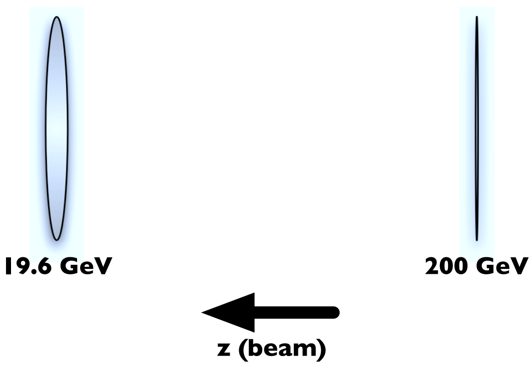

Figure 1.6. A quantitative comparison of the gold nucleus aspect ratios at two different energies, 19.6 and 200 GeV.

At $\sqrt{s_{\mathrm{NN}}} = 19.6$ GeV, each nucleon is traveling at $\beta \approx 99.547\%$ the speed of light (as compared to 99.996% at $\sqrt{s_{\mathrm{NN}}} = 200$ GeV). $\sqrt{s_{\mathrm{NN}}} = 19.6$ GeV is equivalent to a fixed-target collision with a beam kinetic energy of about 204 GeV/nucleon.

In this study, the particle species we look at are positive pions, negative pions, positive kaons, negative kaons, protons, and antiprotons. Their properties are tabulated in Table 1.2.

hadron	quark content	charge (e)	strangeness	mass (MeV/c^2)
π^+	$u\bar{d}$	$+1$	0	139.57 ± 0.00035
π^-	$\bar{u}d$	-1	0	139.57 ± 0.00035
K^+	$u\bar{s}$	$+1$	$+1$	493.677 ± 0.016
K^-	$\bar{u}s$	-1	-1	493.677 ± 0.016
p	uud	$+1$	0	938.272 ± 0.00008
$\bar{p}$	$\bar{u}\bar{u}\bar{d}$	-1	0	938.272 ± 0.00008

Table 1.2. The hadrons which are analyzed in this study.

At 19.6 GeV, we study the collisions of nuclei in the similar energy density as one of the heavy-ion runs at the Super Proton Synchrotron (SPS). The SPS, located at CERN in Geneva, Switzerland, began its first Pb-run in 1994. At its top energy, SPS collided lead ions ($^{208}\mathrm{Pb}^{82+}$) into thin foils of metallic lead, ^{208}Pb, at the beam energy of 158 GeV per nucleon, which corresponds to center-of-mass energy $\sqrt{s_{\mathrm{NN}}} = 17.3$

GeV. The results from our analysis will be compared to various SPS experiments such as NA44, NA49, and WA98, along with the higher energy experiments at the Relativistic Heavy Ion Collider (RHIC).

Back to the water analogy, the properties of water change significantly between different phases due to the change in its equation of state (EoS) [60]): from a well-confined solid to a flowing, yet interacting, liquid to a gaseous state where the molecules can disperse freely. The equation of state is the relationship between the pressure and density of matter. A simple test of EOS of matter is to apply a pressure to it and see how its volume (which is directly related to its density via its mass) changes. Liquid water can easily change its shape, but the volume doesn't change, even with a great amount of pressure applied. Air, on the other hand, can fill any volume of its container. Thus one can say that water has a stiff EoS while air has a soft one. In essence, the equation of state tells us about how easily the matter can be compressed.

It is educational to study phases of water by observing a liquid water, an ice cube, or a hot gas; but much more interestingly we can look at boiling water and learn about what happen at the phase transition. The jump in the center-of-mass energy from SPS to RHIC is over a factor of ten. However, one may ask, is there something interesting in between? Are we only learning about a cold hadron gas and a hot plasma, but missing the phase transition? Can we observe the transition? How are the two different systematics between RHIC and SPS compare at the similar energies? The results will contribute to that finding.

1.5 Signals of the Quark-Gluon Plasma

Rich experimental data from heavy ion collisions at ultrarelativistic energies have led to many new and exciting discoveries. Different physics working groups look at the data from different angles to learn about the nature of the quark-gluon plasma formation and evolution. This section will highlight a small subset of the topics physicists study to accomplish that goal.

1.5.1 Strangeness Production

Nuclear matter at normal pressure and temperature contains almost only up and down quarks. Strangeness, if present in the final particle yields, has to be produced from the collisions.

Although strangeness can be produced in a hadron gas, other quarks must be created as well in order to form baryons or mesons. When the QGP is formed, a large increase of strange hadrons is expected because gluons can self-interact and create strange-antistrange pairs. The threshold of such process is relatively low ($\sim$ 300 MeV). Later on, when the plasma transitions into a hadronic phase, those strange quarks combine with other quarks to form strange hadrons.

In Au+Au collisions, the strangeness yields have been found to increases with centrality as well as with energy [15, 17, 61, 62]. The kaon yields relative to pions are enhanced over those from p+p and $\bar{\text{p}}$+p collisions at similar energies. Such results are consistent with the numerical study in [63] where the kaon/pion production in a QGP was predicted to triple the rate in proton-antiproton collisions at the same energy.

1.5.2 High p_T Phenomena

Different regions of particle spectra are dominated by different processes. High transverse momentum particles presumably come from parton-parton hard scattering. Measurement of particle yields in the high p_T region is a useful tool to study the dense nuclear medium effects [64]. Due to the high gluon density inside the quark-gluon plasma, partons traversing the plasmas are expected to lose a large amount of energy.

The partonic energy loss due to interactions with color charged gluons in the medium can be studied by looking at hadron transverse momentum spectra in the high p_T region.

Nuclear modification factor (R_{AA}), which measures the particle yield from ion-ion (AA) collisions (dense QCD medium) relative to that from nucleon-nucleon (NN) collisions (QCD vacuum), is defined as

$$R_{\mathrm{AA}}(p_T) = \frac{\dfrac{d^2N_{\mathrm{AA}}}{dp_T\,dy}/\mathrm{norm}}{\dfrac{d^2N_{\mathrm{NN}}}{dp_T\,dy}} \tag{1.9}$$

where:

- N_{AA} and N_{NN}, for the case of RHIC, are the yields from the Au+Au collisions and p+p collisions, respectively,

- norm is the normalization term. $T_{\mathrm{AA}}(b)\sigma_{\mathrm{NN}} = \langle N_{\mathrm{coll}}(b)\rangle$ is usually used. This is the nuclear overlap function at an impact parameter b, calculated from the Glauber model (see Appendix E),

- N_{coll} is the average number of binary (nucleon-nucleon) collisions in an AA collision and σ_{NN} is the inelastic cross-section of a nucleon-nucleon collision.

If there are no nuclear modification effects, R_{AA} should be equal to 1 at high p_T where hard scattering dominates. From experimental data, however, R_{AA} tends to tail off below unity at high p_T [65, 66, 67, 68, 69]. This provides an evidence of high p_T suppression in heavy ion collisions as compared to p+p collisions. The suppression also becomes greater as the collisions become more central.

A collection of fast hadrons emerging from an event, associated within a small solid angle, is called a "jet." Jets are used as a tomographic probe of medium properties and early stages of the collisions. The suppression of high p_T particles is called jet quenching [70]. Di-jets studies [71, 72] have observed the disappearance of the away-side jets. One possible explanation is that the scattered quarks are dispersed and absorbed inside the dense nuclear medium, hence fewer away-side high p_T particles are detected. Furthermore, these away-side correlations of associated particles have been found to be more suppressed when the trigger particle travels perpendicular to the reaction plane (out of plane) than when it goes across the shorter width (in plane of almond shaped overlap) [73]. Therefore, the amount of jet energy loss increases with the distance it travels inside the medium.

The suppression of high p_T particles, however, could possibly be due initial state gluon shadowing effects [74, 75, 76]. The effect happens when there are several nucleons are close together. Due to the uncertainty principle, a parton from one nucleon can briefly enter into a neighboring nucleon and interact with another parton. This phenomenon, which can modify the properties of the nucleons prior to the collision, is most probable at a low momentum ("small x"), where the gluon density is large. A control system of nucleon-ion collisions, which removes the post-collision nuclear medium, was suggested [64] to separately investigate the contribution from initial-state gluon saturation and final-state [9] jet quenching to the ion-ion system. Recent results from the 2004 d+Au run at RHIC [77, 78, 79, 80]–where we created "cold" nuclear matter environments–show the lack of the suppressions observed in Au+Au, supporting the notion that jet quenching is a final state effect.

1.5.3 Event Azimuthal Anisotropy

If thermalization occurs in nuclear collisions, collective effects such as flow should determine how the system develops in later stages. Not only does flow indicate whether the system is thermalized or not, it may also tell us about the initial state,

---

[9] A final state effect refers to a measurement which is affected by the nuclear medium created after the collision.

the equation of state and freeze-out condition of the system [60]. Unlike in nucleon-nucleon collisions, geometry (centrality) plays an important role in heavy ion collisions. Azimuthal anisotropy in momentum space in a peripheral collision provides a signature of transverse collectivity [81] and early stages of the collisions [82, 83].

The measurement of the azimuthal distribution of particle yield on an event-by-event basis can be broken down into different Fourier components.

$$\frac{dN}{d\phi} \propto \frac{1}{2\pi}(1 + 2v_1 \cos(\phi) + 2v_2 \cos(2\phi) + \ldots) \tag{1.10}$$

where ϕ is the azimuthal angle of the p_T vector with respect to the reaction plane of the given event. The first term (1) is called the "isotropic" flow, v_1 the "directed" flow, and v_2 the "elliptic" flow. In a non-central collision, the largest component is the second anisotropy coefficient, v_2. This elliptic flow can be calculated from transverse momentum and its polar angle:

$$v_2(p_T) \equiv \langle \cos(2\phi) \rangle_{p_T} \tag{1.11}$$

(For other components, $v_n \equiv \langle \cos(n\phi) \rangle$.)

Specifically, as its name implies, v_2 measures the ellipticity of the source evolution. In a non-central heavy ion collision, the system has an almond shape to begin with. This particular spatial anisotropy is largest right after the collision. From the shape of the source, the pressure gradient, i.e., force, is greater along the reaction plane than perpendicular to it. Non-zero v_2 measurements [84, 85, 86, 87, 88], which decrease with increasing centrality, imply that the interactions occur early, possibly in the partonic phase. v_2 has been measured for a wide range of particles, including Ξ, Ω, π^0, photons, and electrons [89, 90], to study mass and baryon-meson effects of the collective flow.

The elliptic flow and jet suppression phenomena provide evidences that the plasma is a dense liquid-like medium, as opposed to a gas of quarks and gluons [91].

1.5.4 Charm Measurements

The charm quark is expected to be formed at an early stage (where the energies of the interacting partons are still high) mostly via the gluon fusion and quark-antiquark annihilation channels. Measurement of charm quark production, along with other heavy flavors, is important for heavy ion collisions. Due to the large masses of heavy quarks, perturbative QCD (involving hard hadronic processes) can be used to calculate the cross-sections of these quarks [92]. Also since they are produced early and are expected to lose energy inside the high-density QCD matter [93, 94], heavy quarks are useful probes of the initial state of the system.

A suppression in J/Ψ (a $c\bar{c}$ bound state) production is expected if a QGP is formed. This is due to the Debye color screening [95, 96, 97], where a $c\bar{c}$ pair is weakly bound and broken up into open charm (non-zero charm number, that is, a c or a $\bar{c}$, but not both) particles by other smaller quarks inside the deconfined medium.

Productions of charmed hadrons, both open charms such as D^0, $D^{\pm}$, and D^*, and charmoniums such as J/Ψ, have been measured both directly and indirectly, via semi-leptonic decays of D mesons and invariant mass [10] reconstruction [98, 99, 100, 101, 102, 103]. A preliminary elliptic flow result from RHIC [98] also indicates a possible existence of heavy quark coalescence [104]. This is still an open question whether charm quarks "flow." If this non-zero charm flow is confirmed, one could gather that the collective motion already develops in the partonic phase and these partons perhaps thermalize, which would be a signature of the QGP formation.

---

[10] $m = \sqrt{(\sum_i E_i)^2 - (\sum_i \vec{p_i})^2}$, where i refers to each decay daughter particle. m is invariant in all frames of reference.

1.5.5 Direct Photons

Since photons do not participate in strong interaction, they can traverse the dense medium while losing much less energy than hadrons do. Therefore, photon signals can provide a probe of the state of the system very early on. Production of high-p_T photons (via $gq \rightarrow \gamma q$) in 200 GeV Au+Au was first measured by PHENIX [105] and found to be enhanced in the high p_T region relative to background photons (e.g., from the decays of π^0 and η). This implies an existence of a medium in the final-state that suppresses high-p_T partons but not photons–a predicted property of a color medium such as the QGP [106].

1.6 Outline of Experimental Aspects

This portion of the thesis is organized as follows. It will begin by introducing the nature of the experiment, both the accelerator and the detector (Chapter 2). The details of the analysis methods, including data selection criteria, centrality selection (Chapter 3), particle identification (Chapter 4), and yield corrections (Chapter 5), will be discussed. Finally, the results and discussions of transverse mass spectra, particle ratios, mean transverse momentum, rapidity density, and freeze-out conditions will then follow (Chapter 6). Conclusion will then be presented (Chapter 7).

Chapter 2

The Experiment

In this chapter the aspects of the analysis involving the accelerator and the detector systems will be described in detail.

2.1 The Relativistic Heavy Ion Collider

The data for this analysis were taken at the Relativistic Heavy Ion Collider (RHIC) [107, 4]. RHIC is located at Brookhaven National Laboratory (BNL). Founded in 1946, Brookhaven is a multidisciplinary scientific research laboratory located in Long Island, New York. Besides RHIC, Brookhaven also houses many other world-class facilities, such as the Center for Functional Nanomaterials, the National Synchrotron Light Source, and the Accelerator Test Facility. To date, six Nobel Prizes (five in Physics and one in Chemistry) have been awarded to BNL research.

RHIC–its top-view layout is shown in Figure 2.1–is the first heavy-ion collider in the world. A particle collider offers a vast energy advantage over a fixed-target accelerator. Figure 2.2 compares the p_{lab} vs. $\sqrt{s_{\mathrm{NN}}}$ between the two systems. To achieve an equivalent center of mass energy, an accelerator for a fixed-target experiment has to do much more work in accelerating the beam.

$$\text{fixed-target} \qquad p_{\text{lab}} = \sqrt{s_{\text{NN}}\left(\frac{s_{\text{NN}}}{4m_{\text{N}}^2} - 1\right)} \tag{2.1}$$

$$\text{symmetric collider} \qquad p_{\text{lab}} = \sqrt{\frac{s_{\text{NN}}}{4} - m_{\text{N}}^2} \tag{2.2}$$

Table 2.1 lists some values of laboratory momentum at different center $\sqrt{s_{\text{NN}}}$. The difference becomes larger as the energy increases.

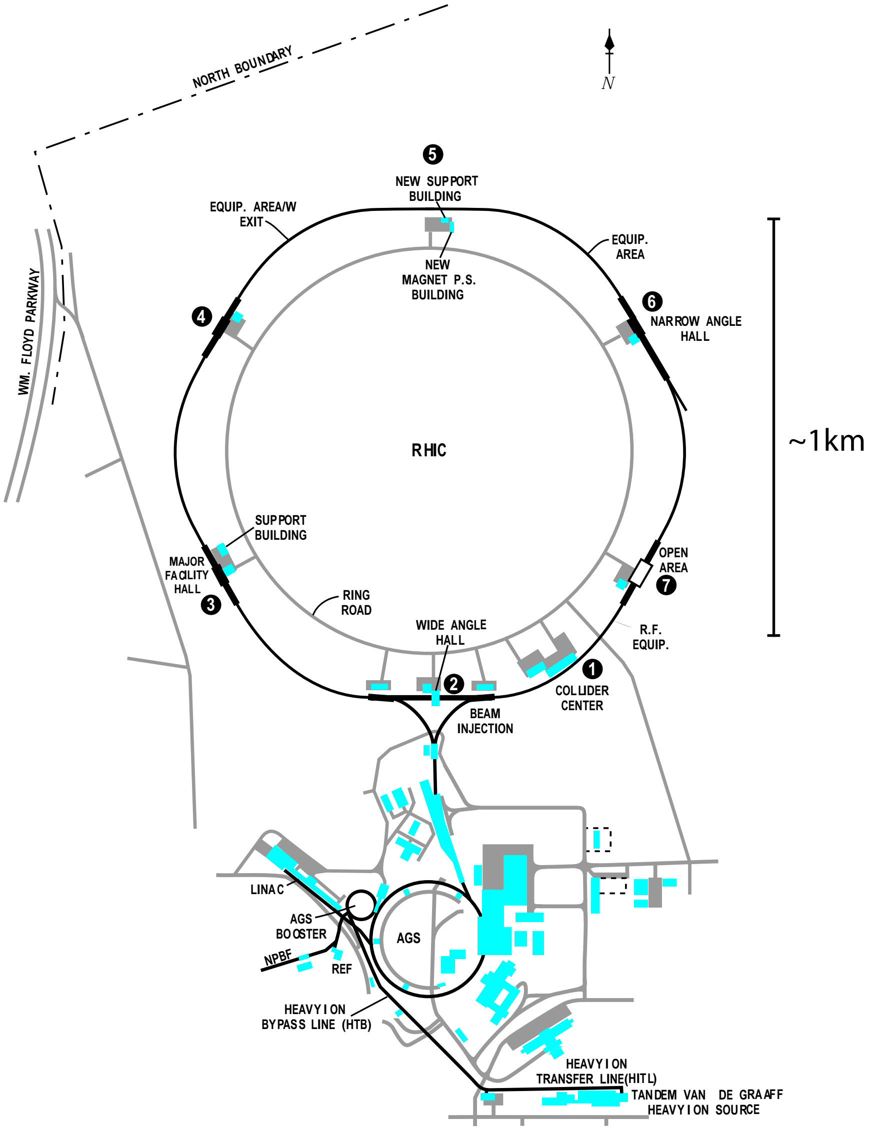

Figure 2.1. The layout of the RHIC complex [4]. The STAR experiment is located at the six o'clock position of the main ring (labeled number 2 in the map).

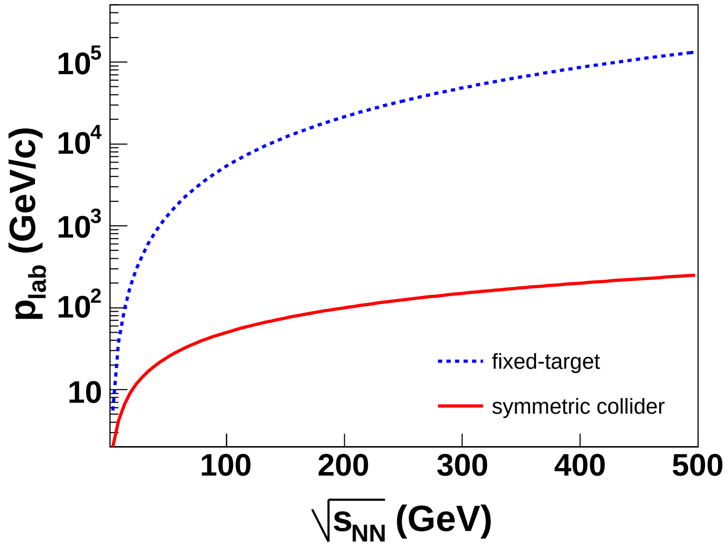

Figure 2.2. The lab momentum per nucleon of the beam as a function of $\sqrt{s_{\mathrm{NN}}}$. The two graphs represent a fixed-target system and a symmetric collider system.

$\sqrt{s_{\mathrm{NN}}}$ (GeV)	p_{lab} (GeV/c)		p_{lab} ratio
	symm. collider	fixed-target	(fixed/collider)
19.6	9.76	205.27	21.04
200	100.00	2.15×10^4	214.71
1×10^3	500.00	5.37×10^5	1073.54

Table 2.1. The comparison of the momentum per nucleon in symmetric colliders and fixed-target systems at different $\sqrt{s_{\mathrm{NN}}}$.

The collider's goal is to search for quark-gluon plasma and study the conditions of the early universe. RHIC is a flexible accelerator which can collide many kinds of species from $A = 1$ (p) to $A = 197$ (Au). Colliding different projectile masses provides different initial states for the collisions. The species scan allows measurements of different nuclear medium effects on particle production. An energy scan at RHIC makes possible the systematic study of various excitation functions.

The difference in possible operating energies for various ions is determined by the charge-to-mass ratio ($q/m \sim Z/A$) of the projectile particle. For gold-on-gold collisions, the center-of-mass energy can go from 20 to 200 GeV per nucleon pair; whereas a kinetic energy of 125 GeV per nucleon for lighter ions–such as oxygen, copper, and iodine–and 250 GeV for protons can be achieved [4] [1]. Table 2.2 summarizes RHIC physics runs over the years.

RHIC Run	Run Period	Species	Energy (per nucleon pair)
Run-1	2000	Au+Au	55.8 GeV
		Au+Au	130.4 GeV
		p (single ring, no collisions)	24.3 GeV (per proton)
		p (single ring, no collisions)	25.1 GeV (per proton)
Run-2	2001-2002	Au+Au	200 GeV
		Au+Au	19.6 GeV
		p+p	200 GeV
Run-3	2002-2003	d+Au	200 GeV
		p+p	200 GeV
Run-4	2003-2004	Au+Au	200 GeV
		Au+Au	62.4 GeV
		p+p	200 GeV
Run-5	2004-2005	Cu+Cu	200 GeV
		Cu+Cu	62.4 GeV
		Cu+Cu	22.4 GeV
		p+p	200 GeV

Table 2.2. History of physics running at the Relativistic Heavy Ion Collider. Our analysis looks into Run-2 19.6 GeV Au+Au. The data are from [34].

---

[1] However, only p+p at 200 GeV has been run, since it is more important to have a reference system for Au+Au at 200 GeV than to run 500 GeV p+p, which is still of lower energy than p+$\bar{\text{p}}$ at Fermilab Tevatron. (However, spin-polarized protons are unique at RHIC.)

RHIC is also capable of colliding proton beams of different spin polarizations. The goal of the spin program is to study the internal spin structure of the proton [108, 109, 110, 111]. We will mainly discuss the Au+Au collisions in this chapter and throughout the paper.

2.1.1 The Pre-Accelerators

Gold (atomic weight 196.97, $Z = 79$, melting point 1337.33 K, boiling point 3129.15 K [112]) has only one stable isotope: Au-197. This fact is beneficial since it provides a unique charge/mass (ratio) uniformity for acceleration of the colliding nuclei. Before gold ions can be sent to RHIC for collisions, they have to be prepared by other accelerators.

The gold ions which are used in the collisions begin their lives inside the Tandem Van de Graaff (TVdG) accelerator [113]. The ions are first generated as singly charged Au^{1-} from a pulsed cesium ($_{55}Cs$) sputtering source. The negative ions are accelerated toward a high-voltage terminal of +14 million volts. The ions are passed through a thin carbon foil (areal density of 2 $\mu g/cm^2$), which strips off some electrons. The resulting positive ions are then accelerated away from the positive terminal, and, before they leave the Tandem Van de Graaff, go through a 15 $\mu g/cm^2$ carbon electron-stripper foil.

By the time the ions leave the Tandem, they will have an energy of approximately 1 MeV per nucleon and be in +32 charge state. The Au^{32+} ions are then transferred to a synchrotron called the Booster, via the Tandem-To-Booster (TTB) line. The TTB consists of a series of bends arranged in pairs: two 90°, two 24°, and two 13° bends. The first bend pair selects the ions with desired momentum while the other two pairs are arranged in an achromatic fashion [114] (so that ions of different momenta would emerge at same direction).

The Booster synchrotron has a circumference of 201.8 m. A series of bending magnets around the ring is used to confine the charged beam. Inside a synchrotron, a magnetic field is parallel to the path of the ions. From the Lorentz magnetic force law, $\vec{F_B} = q(\vec{v} \times \vec{B})$, the energy-force relation, $E(r) = \int \vec{F} \cdot d\vec{r}$, and since $\vec{r} \parallel \vec{v}$, the energy $E(r)$ gained from magnetic force will be zero. An electric field is used to accelerate particles. This function is served by a radio-frequency (RF) cavity. The geometry of the RF cavity determines the resonant frequency of the electromagnetic field. When charged particles go in a circular orbit around the ring, they emit photons in a process called the "synchrotron radiation." According to the Larmor formula (equation (2.3)), the radiation rate increases rapidly with the particle's velocity,

$$\frac{dE}{dt} \propto \frac{\beta^4 \gamma^4}{R^2} \tag{2.3}$$

where β is the speed of the particle, $\gamma \equiv (1 - \beta^2)^{-1}$, and R is the radius of curvature. Therefore, a fast particle in a small synchrotron emits the largest radiation.

The RF system both restores the energy loss due to the synchrotron radiation and accelerates the beam along the ring.

Since the radius of curvature R of a particle with charge q and momentum p, moving in a magnetic field B, is given by $R = p/(qB)$, the magnetic field has to be synchronized (thus the name synchrotron) to the change in beam momentum to keep the radius of curvature constant. The higher the energy, the higher the magnetic field. Inside the Booster, the ions are put into six bunches, accelerated to about 37% the speed of light, and put through another electron stripper.

From the Booster, the gold ions are transferred by the Booster-To-AGS (BTA) line into a larger synchrotron, with four-time the radius of the Booster, called the Alternating Gradient Synchrotron (AGS). Dealing with very high-energy beams, the AGS relies on the principle of alternating gradient (AG) focusing [115], where the B field radial gradients ($\partial B/\partial r$) alternate along the ring, to keep the beam focused.

It takes four batches of ions from the Booster to fill one AGS cycle. Inside the AGS, the gold ions with charge $+77e$ are rebunched into four bunches and further accelerated to 99.7% the speed of light. Finally, the gold ions are fully stripped off electrons as they exit the AGS. Via the AGS-To-RHIC (ATR) line, the Au^{79+} beam is injected into the RHIC collider, whose radius is 19/4 times that of the AGS.

The charge states of the ions as they travel inside the accelerator complex are summarized in Table 2.3.

accelerator	charge in	charge out
TVdG	-1	$+32$
Booster	$+32$	$+77$
AGS	$+77$	$+79$

Table 2.3. Charges of the Au ions at various stages of the acceleration cycle.

2.1.2 The Main Accelerator

RHIC consists of two underground counter-rotating rings of beam, named Blue (clockwise) and Yellow (counter clockwise). The incoming ion beam is split into two beams, each traveling inside a beam pipe in the center of each ring. The beams are not continuous. For each beam, the gold ions are put into 55-60 bunches (this number can vary), each of 20 cm length, with approximately 0.6×10^9 ions per bunch. Thus for each fill, approximately 2.2×10^{-11} grams of gold are used.

Each of RHIC rings is divided into 12 regions. Six of those are the arc regions, where Blue and Yellow rings are parallel and separated by 90 cm radially, and the other six are the insertion regions, where the two rings cross. The RHIC magnet system [116], which guides and focuses the beams, includes many types of magnets. There are 288 arc dipoles, 108 insertion dipoles, 276 arc quadrupoles, and 216 insertion quadrupoles. The arc magnets are mainly used to bend and focus the beam. The insertion magnets are used to focus the beam at the six interaction regions. In addition, there are 72 trim quadrupoles, 288 sextupoles, and 492 correctors. The purpose of the corrector magnets is to compensate the alignment and field errors of the main magnets. RHIC makes use of superconducting magnets, which minimize heat output and lower power requirement. In operation, the magnets are cooled by supercritical (gas and liquid mixed phase) helium to a temperature below 4.6 K.

Inside RHIC rings, the ion beams are accelerated to the desired collision energy and stored for data taking. When the luminosity (i.e. beam quality) drops below a certain level, the beams are "dumped" (removed from the rings) by the RHIC Beam Abort system [117]. Then the cycle restarts inside the TVdG.

The rate of interaction (R) between the colliding beams depend on two factors: luminosity ($\mathcal{L}$) and cross section (σ). The parameter that experimenters can control and optimize is the luminosity. If Blue beam has n_{B} particles per bunch and Yellow beam has n_{Y}, each beam with B bunches per revolution, circling the machine at frequency f, the luminosity can be calculated as [118]

$$\mathcal{L} \simeq \frac{f B n_{\mathrm{B}} n_{\mathrm{Y}}}{A} \tag{2.4}$$

with A being the crossing area. The crossing area depends on the horizontal and vertical profiles of the beam, which can be estimated via a technique called the van der Meer (or Vernier) scan. The luminosity RHIC has achieved for Au+Au is 4×10^{26} $\mathrm{cm}^{-2}\ \mathrm{s}^{-1}$ [43].

2.1.3 Heavy Ion Experiments

RHIC rings are 3,833.9 m in circumference with the average radius of 610.2 m. The RHIC RF system consists of accelerating cavities (at frequency 26.7 MHz) which capture and accelerate the bunches to top energy and storage cavities (196.1 MHz) which compress the bunches to optimize the luminosity. There are two accelerating cavities and two storage cavities in each ring. Along the rings, there are six common cavities, called the interaction regions (IR). The RF system resides at one of the non-experimental crossing point (four o'clock position). Located at other crossing points are four heavy-ion experiments named BRAHMS, PHOBOS, PHENIX, and STAR, and one empty hall at the 12 o'clock position.

The Broad RAnge Hadron Magnetic Spectrometers (BRAHMS) [119] is located at the two o'clock position of RHIC. BRAHMS measures charged hadrons over a wide rapidity [2] and transverse momentum range in the forward direction (y up to ≈ 4). BRAHMS utilizes two spectrometers, called the Forward Spectrometer (FS) located along the beam axis and the Mid-Rapidity Spectrometer (MSR) perpendicular to it. The spectrometer arms can be rotated to allow measurements of charged hadron production in different acceptance regions.

At 10 o'clock position is PHOBOS [120], an experiment which studies a large number of unselected collisions. With high trigger and data acquisition rates, along with a large coverage in pseudorapidity, PHOBOS specializes in giving a global picture of the event using many silicon pixel and strip detectors near the collision region. PHOBOS identifies particles using time of flight and energy loss measurements.

The Pioneering High Energy Nuclear Interaction eXperiment (PHENIX) [121] is located at eight o'clock. PHENIX looks into rare, hard probes (large-mass particles, high momentum transfer). Some of the probes include electrons, muons, and direct photons which emerge from the collision unaffected by the strong force. PHENIX consists of four spectrometers, two at midrapidity ($y = 0$) to detect charged hadrons, electrons, and photons, and two at forward rapidities for muons.

Finally, the STAR experiment is located at six o'clock. Its facility layout is illustrated in Figure 2.3. The detector's large and cylindrically symmetric coverage makes possible the analyses of event-by-event quantities. STAR will be discussed in more detail in the next section.

All of the heavy-ion experiments utilize one common detector subsystem: the Zero Degree Calorimeter (ZDC). Each experiment uses a pair of ZDCs to measure the energy of spectator neutrons [122] residing within a small solid angle from the

---

[2] Definitions of kinematic quantities such as rapidity, pseudorapidity, and transverse mass are given in Appendix A.

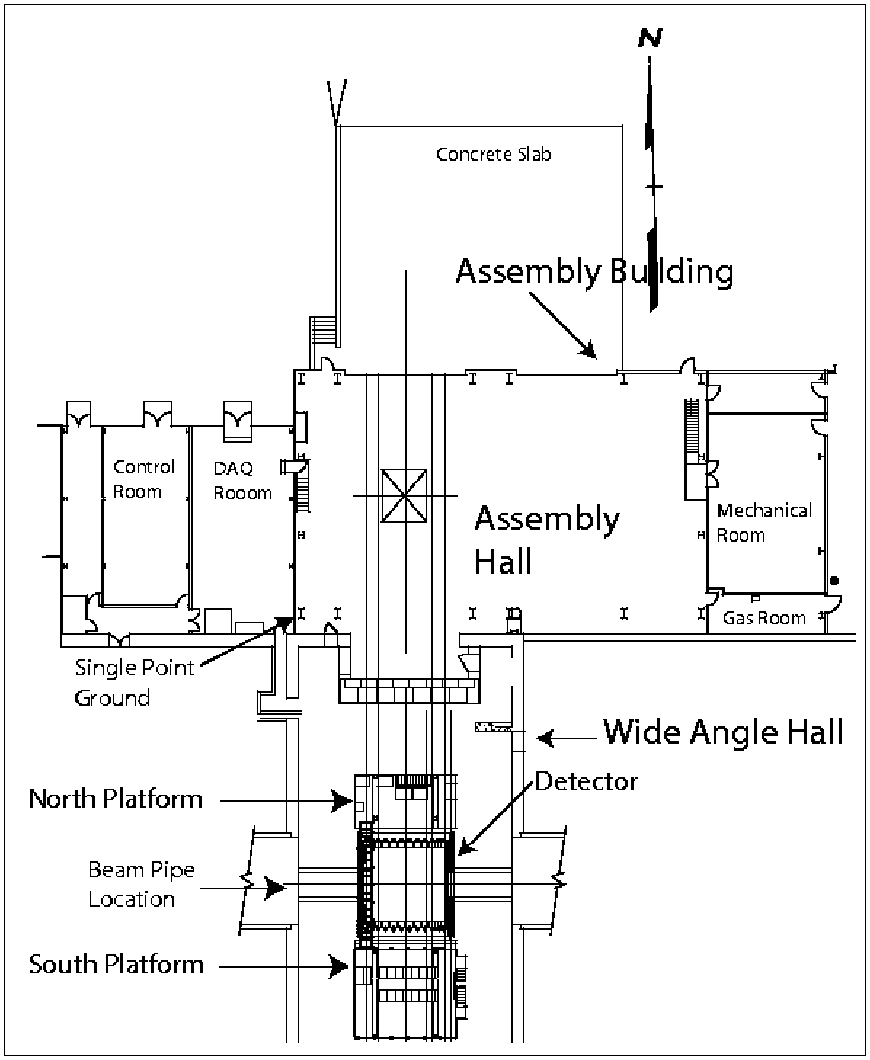

Figure 2.3. The layout of STAR facility [5]. The 1,100 tonne detector must move 33 m between the Assembly Hall for maintenance to the Wide Angle Hall for operation. The move between the halls typically occurs once a year.

beam to provide universal characterization of the collision centrality across RHIC experiments. The 12 ZDCs are located ±18.25 m on each side of the six interaction regions. Since the charged particles are deflected by the dipole magnets, only the neutrons can reach the ZDCs.

RHIC has been colliding both ions and protons since 1999 and had its first Au+Au event (at $\sqrt{s_{\rm NN}} = 56$ GeV) in June 2000. Its next major upgrades [123] (such as RHIC II [124] and eRHIC [125]), with new and exciting physics possibilities, are planned to start around year 2008, the time when the Large Hadron Collider (LHC) begins its first Pb+Pb collisions at $\sqrt{s_{\rm NN}} = 5.5$ TeV. Connections between LHC and RHIC results will certainly complement each other and provide valuable insights into the physics of nuclear interactions at relativistic energies.

2.2 The STAR Detector

The data presented in this study have been obtained from the Au+Au collisions at the Solenoidal Tracker at RHIC (STAR). The data from Au+Au collisions at $\sqrt{s_{\rm NN}} = 19.6$ GeV were collected during RHIC Run II, for a duration of approximately only one day during 25-26 November 2001. $\sqrt{s_{\rm NN}}$ of 19.6 GeV is achieved directly from the injection energy from AGS into RHIC. Historically, this one-day run was initiated by a PHOBOS proposal to study charged particle multiplicity at a low energy.

The STAR detector is a large coverage and high multiplicity detector. It is one of the two large heavy ion experiments (the other is PHENIX) at RHIC. STAR searches for signatures of the quark-gluon plasma by investigating the global observables of nuclear collisions over a wide rapidity (y) and azimuthal (ϕ) range.

A perspective view of STAR is shown in Figure 2.4. Figure 2.5 shows a GEANT drawing of year 2001 geometry. The main detector of STAR is the Time Projection Chamber (TPC) [7], a large cylindrical detector with dimensions 4.2 m in length and

4.0 m in diameter. The TPC is a drift chamber that gives three-dimensional spatial information as well as the energy loss of the particles. The STAR TPC covers the full 2π in ϕ and pseudorapidity $|\eta| < 1.8$. STAR local coordinate system is defined by a right-handed Cartesian axes: x points parallel to the ground and away from the center of RHIC, y points directly up from the ground, and therefore z points west at STAR [126].

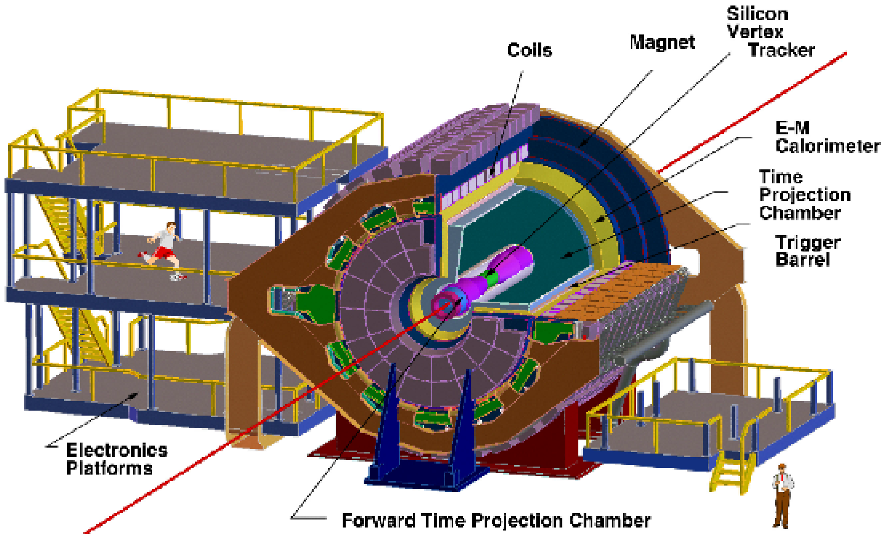

Figure 2.4. The STAR detector [6] next to the electronics platform. Inner subsystems are also displayed. The straight red line represents the beam axis.

The Time Projection Chamber tracks particle trajectories via the secondary electrons which are released from gas molecules due to ionization. The electric field and pressure settings are optimized to a condition such that the electrons drift at the peak velocity inside the P10 gas. This way, a small change in pressure would not significantly affect the drift velocity. The electrons drift inside a well-defined axial electric field toward the anodes and give information on the amount of energy loss. The positions where the electrons are liberated give information of the particle trajectories, which can then be used to calculate their momenta in three dimensions. This information can be used to do particle identification, as will be discussed in Chapter

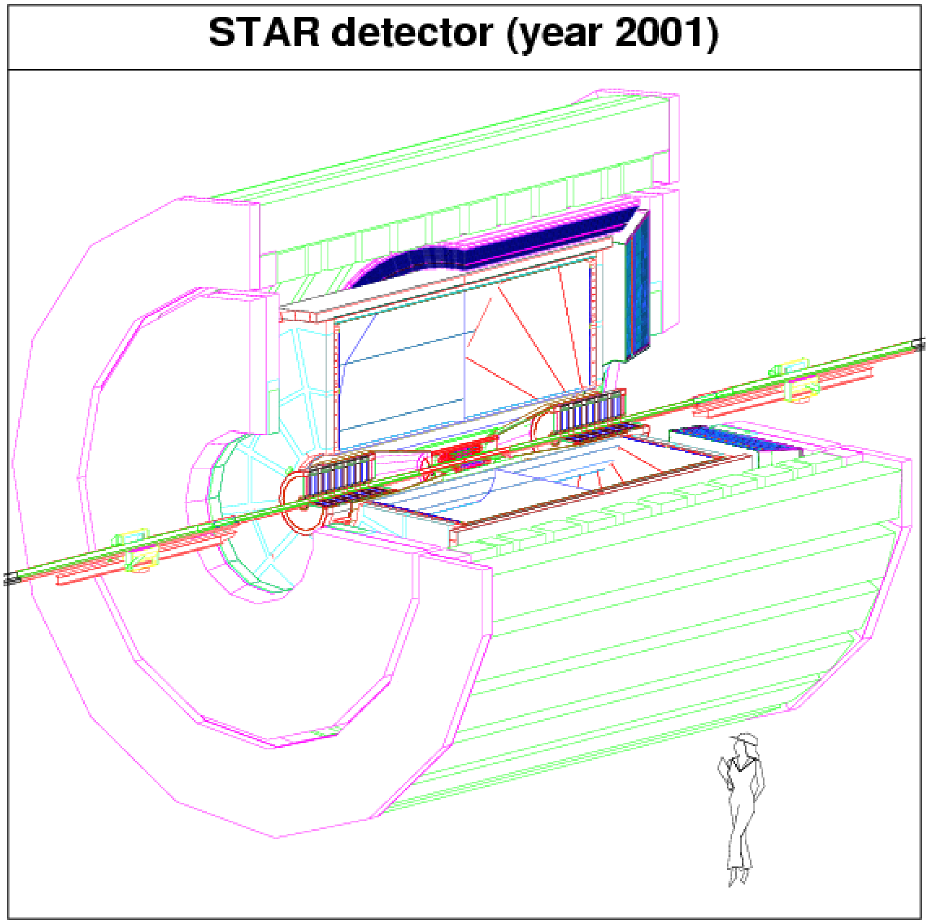

Figure 2.5. A GEANT drawing of the STAR detector with year 2001 (when 19.6 GeV run was taken) geometry.

4.

2.2.1 Magnet

The 1,100-ton solenoidal magnet [127] surrounding the TPC provides a magnetic field parallel to the axis of the detector. A current of $I = 2250$ A is applied to the magnet to provide a field ($B = \mu n I$, with μ being the relative permeability and n the coil density) of 0.25 Tesla (STAR "half field") for the 19.6 GeV Au+Au run. The magnetic field and track trajectories, when known, allow the precise reconstruction of the charged particles momenta.

A 6.85-m long return-field steel cylinderforms the outer wall of the cylinder. Located outside the solenoidal magnet from radius 5.27 to 6.28 m, the steel bars confine the magnetic field (remove edge effects) and also serve as support structure to other detector subsystems.

2.2.2 Gas System

The gas system [128] of the STAR TPC provides a pure gas mixture and cools down the outer field cage resistors. P10 gas consists of 10% CH_4 (methane) and 90% Ar. The gas fills the TPC drift volume (0.5 to 2.0 m radius). The pressure is kept at 2 mbar above the prevailing (experimental hall) atmospheric pressure (1 atm or 1.01325 bars). The amount of electron attachment needs to be minimized to prevent the electron clusters with longer drift distances from appearing to have lower ionization. The oxygen and water are kept below 100 and 10 parts per million, respectively, to minimize this electron absorption.

The argon ($\sim$ 16 eV first ionization energy) is the gas to be ionized by the produced particles. Argon is inert (that is, does not form molecular compounds) and exists in a very pure form (99.6% of argon in nature is ^{40}Ar). It is also odorless and colorless. The methane, due to its complex molecular structure, functions as the quenching ("shock absorbing") gas for the secondary electrons by means of its many low-energy rotational levels.

As a safety measure, a number of analyzers are used to monitor and control pressure, temperature, mixture, and purity of the TPC gases (argon, methane, oxygen, water, and nitrogen). For example, if the O_2 content becomes too high, a flow of flammable CH_4 will be shut off.

2.2.3 Electric Field

The electric field inside the TPC is defined by a cathode plane, two grounded end-cap planes, and two field cage cylinders. The high-voltage cathode is called the Central Membrane (CM). The CM, which is made of 70-μm-thick carbon loaded kapton film, is located in the middle of the detector, with a 50-cm radius hole in the center for the inner field cage (IFC) to pass through. The outer field cage (OFC) closes the drift volume at the outer radius of the CM. The Central Membrane is (typically) kept at -28 kV potential.

The electric fields in two sides of the CM point in opposite directions, along the beam line and away from the nearest end caps. The thin concentric field cage cylinders help providing a uniform electric field along the TPC length by defining boundary potentials in 182 equally-spaced steps from the CM to the anode planes. This is done by a series of resistors.

The arrangement of the electric field being parallel to the magnetic field inside the TPC helps minimize the transverse diffusion of the drifting electrons. The magnetic component of the Lorentz force $\vec{F} = q\vec{v} \times \vec{B}$ pushes the electrons to wind around the electric field vectors.

The combination of the gas pressure and the TPC electric field settings results in a fast and stable drift velocity of about 5.45 cm/μs for the electrons. The TPC is considered a "slow" detector [3]. The relatively long drift time from the center of the detector to the anode planes ($\sim 40\mu$s) is one of the limiting factors in TPC readout rate. The drift distance is measured in z direction from the point of ionization to the closest anode plane. In a 0.5 T magnetic field (STAR "full field"), the diffusion is low; after a 210-cm drift (full drift length), $\sigma_T = 3.3$ mm and $\sigma_L = 5.2$ mm for transverse and longitudinal directions, respectively. The diffusion is larger in smaller fields.

2.2.4 Readout

The Time Projection Chamber end caps consist of readout planes, which are essentially multiwire proportional chambers (MWPC). The components of the MWPC are a readout pad plane, arranged into 12 sectors with 45 pad rows per sector, and three sets of wires: anode grid, ground grid, and gating grid.

The anode sector, with components and dimensions shown in Figure 2.7, is further divided into inner and outer subsectors. The inner part consists of small pads (2.85 mm × 11.5 mm), arranged into 13 rows. The rows are separated by 4.8 cm radially. The innermost row (row 1) is 60 cm away from the TPC axis [4]. The outer subsector has larger pads (6.20 mm × 19.5 mm), packed into 32 rows. There are no spaces between the outer pad rows; this optimizes the ionization resolution. There are a total of 5,692 pads per sector, or 136,608 for the entire TPC readout system.

The gating grid wires are made of gold-plated Be-Cu with a 75-μm diameter. The separation between wires is 1 mm. The gating grid separates the drift volume and the MWPC volume and is "open" only when a trigger is issued. In the open state, the

---

[3] Other slow detectors in STAR include the Silicon Vertex Tracker (SVT), Forward TPCs (FTPC), Shower Max Detector (SMD), Photon Multiplicity Detector (PMD), Time-of-Flight-patch (TOFp), and Ring Imaging Cherenkov (RICH)

[4] From the relation between momentum, magnetic field, charge, and radius of curvature, we can calculate the minimum p_T that a particle needs to record a hit on this innermost row to be ≈ 22.5 MeV in a 0.25 T magnetic field.

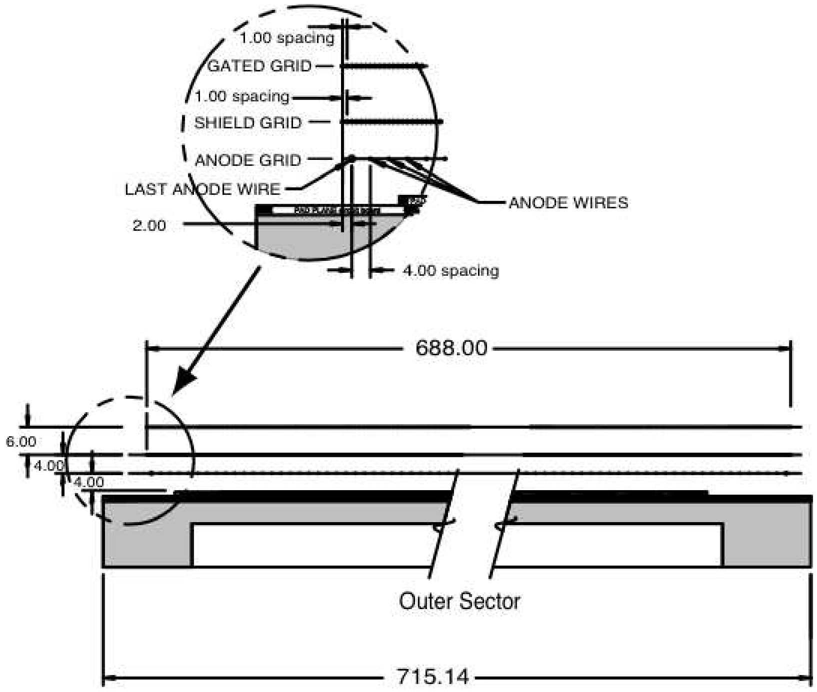

Figure 2.6. The wire planes of the Time Projection Chamber [7]. Dimensions are in millimeters.

gating grid wires are set to the same potential as the surroundings (typically −110 V). At this state, the grid is basically transparent to the electrons and ions. The grid can be closed by adjusting the voltages on the wires in such a way that the field lines terminate on the grid wires (±75 V, alternately). This prevents the positive ions formed in the proportional-multiplying region from going back into the drift volume and distorting the TPC electric field.

Once the electrons pass through the gating grid, they encounter the ground (shielding) grid, located 6 mm from the gating grid. The ground wire material and arrangement are exactly of same as that of the gating wires. The ground grid is used to terminate the drift field.

The high-voltage anode wires creates a strong field which causes the electrons to accelerate and in the very high-field region near the small-diameter wires [5] to further

---

[5] The electric field near a straight charged wire is proportional to $1/r$, where r is the distance away from the wire. The thinner the wire, the stronger the field around the wire, and thus the

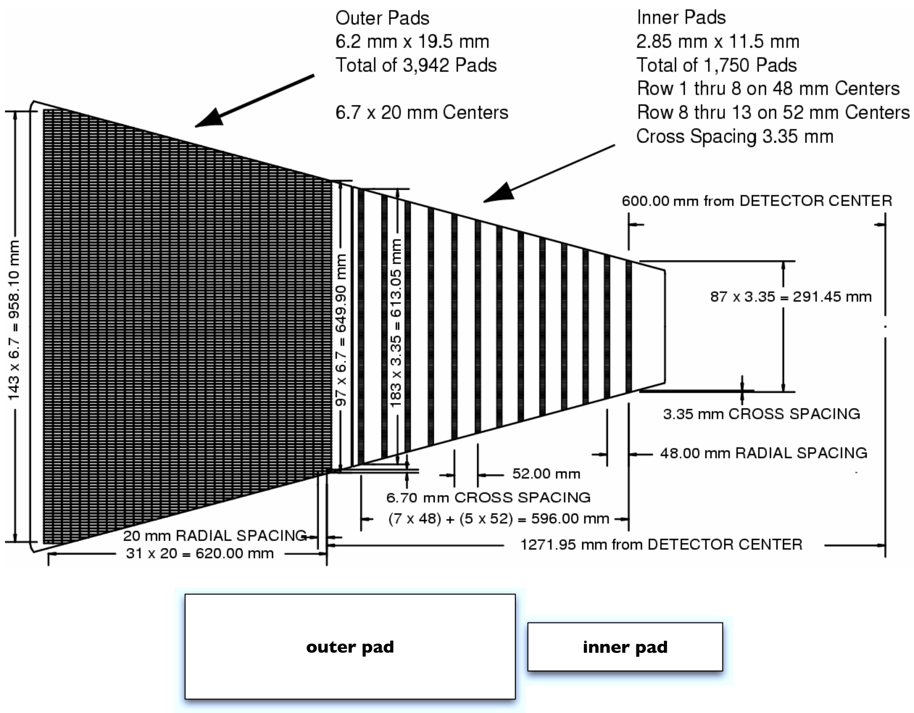

Figure 2.7. The STAR TPC pad plane of one sector. The lower panel shows the relative sizes of the pads.

ionize the gas (P10, as in the main volume). This process amplifies the signal by a constant gain factor in an order of 1,000 to 3,000. The gas gain has to be minimized to prolong the life of the anode wires, and at the same time, must be high enough to overcome the electronic noise. The gains in inner and outer sections are controlled independently by the respective wire voltages (1.17 kV for inner sector and 1.39 kV for outer sector). The image charges due to the avalanches on the anode wires induce currents on the anode pads, and go to the electronics.

Attached to the readout sectors are the Front End Electronics (FEE) cards [129]. Each 32-channel FEE card receives analog signals from the anode pads. On each card, there is a 16-channel STAR preamplifier/shaper (SAS) chip and a 16-channel switched capacitor array/ADC (SCA/ADC) chip. The SAS chip amplifies and shapes the signals. Then the SCA chip digitizes the signals into 512 time bins, and stores a voltage value for each bin. The readout boards then gather and pass the digital signals from the FEE cards to the STAR Data Acquisition (DAQ) system [130]. STAR DAQ reads millions of analog-to-digital conversion (ADC) values from the events and write them to tapes at event rates up to 100 Hz. The raw data from the anode pads are reconstructed into hit locations. These hits are then grouped into tracks. Finally, the tracks are extrapolated back to their collision origins (vertices).

2.2.5 Material

To minimize interaction between the traversing ions and gas molecules, a vacuum is kept inside the beampipe. The vacuum is maintained by the RHIC warm-bore vacuum system [131]. The design vacuum at the interaction point (IP) is $< 5 \times 10^{-10}$ Torr ($\sim 1.7\times10^{7}$ molecules/cm^{3}). The pipe must be designed to use a minimal amount of the tube and support structure. Outside the detector, 1.5-mm-thick stainless steel is used. At 402.59 cm from the IP, the beampipe becomes 1.24-mm-thick aluminium,

---

greater the amplification.

and at 76.20 cm from the IP, the beampipe transitions into 1-mm-thick beryllium [5].

Collisions between the beams happen inside this beryllium section. As we will see in a later discussion, the interaction of charged particle is proportional to the atomic number (Z) of the medium. Therefore, we want to keep Z of the beampipe as small as possible to keep beampipe interaction low. Therefore, ${}_4$Be is used [6]. Beryllium is also a very light non-magnetic metal with very high melting point (1014 K) and stiffness; its stability is desirable for accelerator uses.

Between the center of the TPC to the inner field cage, nitrogen gas is used to electrically isolate the field cage from the inner detectors and support structures. Nitrogen is also used to isolate the outer field cage from the outer aluminum shell of the TPC.

Table 2.4 summarizes the thickness of material and gas layers in terms of radiation lengths (X_0) [7] traversed by the track between the interaction region and the active volume of the main tracking detector TPC.

structure	radiation length ($\%X_0$)
beryllium beampipe	0.28
Silicon Vertex Tracker	6
N_2 (insulating gas)	0.13
inner field cage	0.52
P10 gas	1.17
outer field cage	1.26

Table 2.4. Thickness of the detector material [7, 35].

2.2.6 Safety

The STAR detector is implemented with interlocks [132] to protect the detector from possible accidents. The interlock system reads the inputs from different facilities such as gas detectors, smoke detectors, and water leak detectors. When a fault is

---

[6] ${}_1$H and ${}_2$He are non-metals. ${}_3$Li is flammable.

[7] X_0 is the mean distance over which a high-energy electron loses $1/e$ of its initial energy via bremsstrahlung.

detected, the interlock system puts the detector into a safe mode by automatically performing tasks such as shutting down the power or cutting off the water flow.

2.2.7 Event and Track Reconstruction

Clusters of electrons from ionization drift inside the TPC electric field towards the end caps. The reconstruction software for the TPC determines the electron clusters (called hits) recorded from the anode endcaps. In heavy ion collisions, the experiment faces several challenges: the high track density, the low average transverse momentum, multiple scattering, and energy loss of the produced particles.

The hits on the pad rows are converted into spatial coordinates (x, y, z) [8], with the local x-axis being defined along the pad row direction, the y-axis perpendicular to the pad row and pointing away from the beam line, and the z-axis parallels the beam direction. While the x and y coordinates are locations of the hits, the z coordinates are calculated from the arrival times of the electrons, measured in time buckets (each being approximately 100 ns long).

The locations of the pads determine the x and y positions of the charged clusters. The distributions of hits are fitted with two-dimensional Gaussian functions in x and y. A three-point Gaussian fit is defined by the amplitudes (h_1, h_2, and h_3, sequentially) on three adjacent pads (for x) or rows (for y) with similar drift times and the pad width (w). A local x coordinate of a cluster is determined by

$$x = \frac{\sigma^2}{2w} \ln\left(\frac{h_3}{h_1}\right) \tag{2.5}$$

where

$$\sigma = \frac{w}{\sqrt{\ln\left(\dfrac{{h_2}^2}{h_1 h_3}\right)}} \tag{2.6}$$

---

[8] The x and y here are not the same as the x and y used to describe the STAR local coordinate system.

For y, the equations will be similar, with h_1, h_2, and h_3 being the amplitudes on three adjacent rows.

Before the tracks can be reconstructed, several distortions have to be accounted for [7]. The distortions between the reconstructed hits and the actual cluster locations can be caused by non-uniformities of the magnetic field (± 0.0040 T), the geometrical effect between inner and outer anode subsectors, the small angular offset between E and B fields, the non-flatness and tilt of both the Central Membrane and the endcaps, the misalignment between the inner and outer field cages, and the space charge build-up from positive ions. These distortions affect the electron trajectories. The correction for each of these distortions is in a millimeter scale. Once the corrections are applied to the hit locations, particle trajectories can be fully reconstructed.

Since beam-beam events occur at the beam line, the track density is lowest at the outermost pad rows, which is where the track finding algorithm begins. Groups of three adjacent hits are used as "roots" (also called "links") of the tracks. The roots are combined to form track segments. The segments are later extended to include all the hits. Finally the segments are merged. The merging process first calculates the helix parameters (radius, centroid, dip angle) for each segment. If the parameters of a given two segments agree within the specified conditions, then the segments are assumed to be part of the same track and joined into a single segment.

The vertex finding algorithm [133] starts by looking for tracks which come within a certain radius $R_{\max}$ from $(x, y) = (0, 0)$ [9]. These tracks are fitted with helices and extrapolated towards the beam line. The weighted sum of the distance of closest approach (d) squared (tracks which experience more secondary scattering are given less weights) is calculated as a function of x, y, and z: $l^2 = \sum_i {d_i}^2$. A primary vertex is the point (x_0, y_0, z_0) which minimizes l^2. The accuracy of vertex reconstruction increases with the multiplicity.

---

[9] Back to the local x and y coordinates of STAR.

Once the primary vertex has been found, we look at the particle tracks. All the tracks associated with the vertex, which include the primary tracks and the secondary tracks from decays, are called global tracks. The subset which have distances of closest approach to the vertex less than 3 cm are called primary tracks. To determine the momentum of a track, a helix fit is performed [134]. The helix can be fully described by a pivot–or starting point–(x_0, y_0, z_0), and the following parameters: h, s, R, Φ_0, and θ_{dip}, where:

- h is the sense of helix rotation in the xy plane and is defined as $h = -\text{sign}(qB) = \pm 1$,
- s is the transverse path length,
- R is the helix radius,
- Φ_0 is the azimuthal angle of the pivot with respect to the helix center (x_c, y_c), and
- θ_{dip} is the angle between $\vec{p}$ and $\vec{p}_T$. So θ_{dip} is zero when the track has no z component of momentum.

Then, the helix equation is

$$x(s) = x_0 + R\left[\cos\left(\Phi_0 + \frac{hs\cos\theta_{\text{dip}}}{R}\right) - \cos\Phi_0\right] \tag{2.7}$$

$$y(s) = y_0 + R\left[\cos\left(\Phi_0 + \frac{hs\cos\theta_{\text{dip}}}{R}\right) - \sin\Phi_0\right] \tag{2.8}$$

$$z(s) = z_0 + s\sin\theta_{\text{dip}} \tag{2.9}$$

The circular projection on xy plane gives the transverse momentum, p_T. From dip angle, the longitudinal momentum can be obtained from $p_z = p_T \tan\theta_{\text{dip}}$.

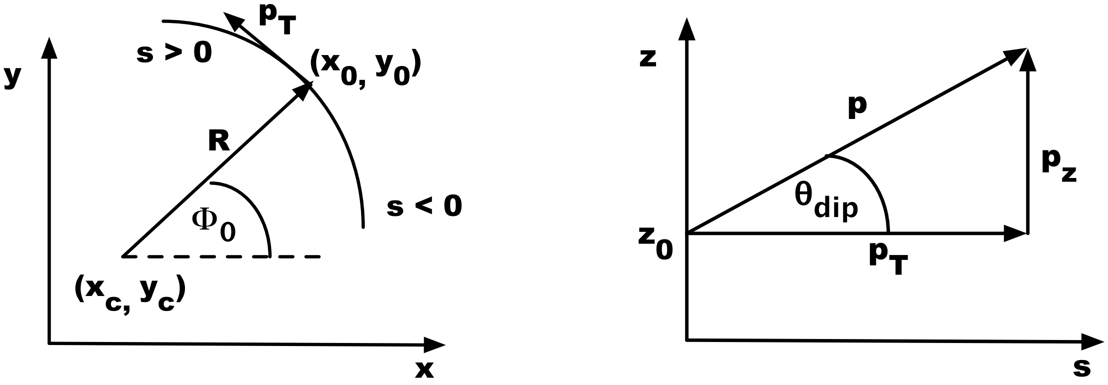

Figure 2.8. Helix parametrization. Left panel: projection of a helix on the $x-y$ plane (bend plane). Right panel: projection on the $s-z$ plane.

Chapter 3

Data Analysis

Several criteria were placed on the event data to optimize the data quality by increasing signal-to-background ratio and minimizing biases. In this chapter, the STAR trigger system is introduced and data selections are described.

3.1 Trigger

Triggering is a method of selecting specific events from the data. The STAR trigger system [8] is set up based on the kinds of physics we are interested in. For example, to select central collisions we look for events with high multiplicities; to find jet events, one look for "high tower" signals (those that have energies above some threshold) in the Barrel Electromagnetic Calorimeter (BEMC) [1]. A trigger is used in combination with a prescaler, which scales down the raw rate presented to the detector electronics to the rates that those detectors are capable of reading out. The prescaler also keeps the data recording rate below the maximum rate and allows a rare event to be recorded if it occurs.

Rare events can be selected by using more sophisticated trigger configurations.

---

[1] BEMC is a sampling calorimeter using lead and plastic scintillator. It sits just outside the central trigger barrel and longitudinally covers $|\eta| < 1$.

For example, an ultraperipheral collision (UPC) trigger looks for a 4-prong (e.g. $\Phi \rightarrow K_0 K_0 \rightarrow \pi^+\pi^-\pi^+\pi^-$) event. A dilepton trigger can help find $J/\Psi \rightarrow e^+e^-$ or $\Upsilon \rightarrow e^+e^-$ events. Light antinuclei [135] such as anti-^{4}He and anti-^{3}He can be found by selecting for particles with a -2 charge in dE/dx vs. p curve.

The STAR online triggering is subdivided into different levels called levels 0, 1, 2, and 3 (L0-L3). L0, L1, and L2 are hardware-level triggers which utilizes fast detectors. For every RHIC bunch crossing (every $\sim$ 107 ns), data go into L0 system and L0 decides within 1.5 μs whether it detects a signal and the detectors are LIVE (ready to accept a new event). Levels 1 and 2 are subsequent trigger systems with decision times of approximately 100 μs and 5 ms, respectively. Level-3 [136] utilizes a multiprocessor farm to do quick analyses of online event reconstruction at an event rate of $\approx$ 50 Hz.

The trigger detectors used in the 19.6 GeV run are the Central Trigger Barrel (CTB) [8] and the Zero Degree Calorimeters (ZDC East and ZDC West) [9]. Both detectors rely on the use of scintillation counters. A scintillator, which converts the energy loss of charged particle into visible light, is one of the oldest and most commonly used particle detectors. The electrical signal comes from a photomultiplier tube (PMT) viewing the scintillator. In 1911, for instance, Rutherford used a ZnS scintillator and his eyes (no phototubes) in the alpha scattering experiment.

The CTB detects charged particle multiplicity within $|\eta| < 1$. It consists of 240 scintillator slats arranged in 4 bands, each covering half a unit of pseudorapidity, surrounding the main tracking volume. A diagram of the CTB slats is shown in Figure 3.1. There is one PMT on each slat. Each scintillator slat (channel) covers $\pi/30$ in ϕ and 0.5 in η. The signals (light) from the scintillators go into photomultiplier tubes (PMT), which convert the signals into electrical pulses. The signals then go into a CTB Digitizer Board (CDB) which digitizes the output for the rest of the trigger system.

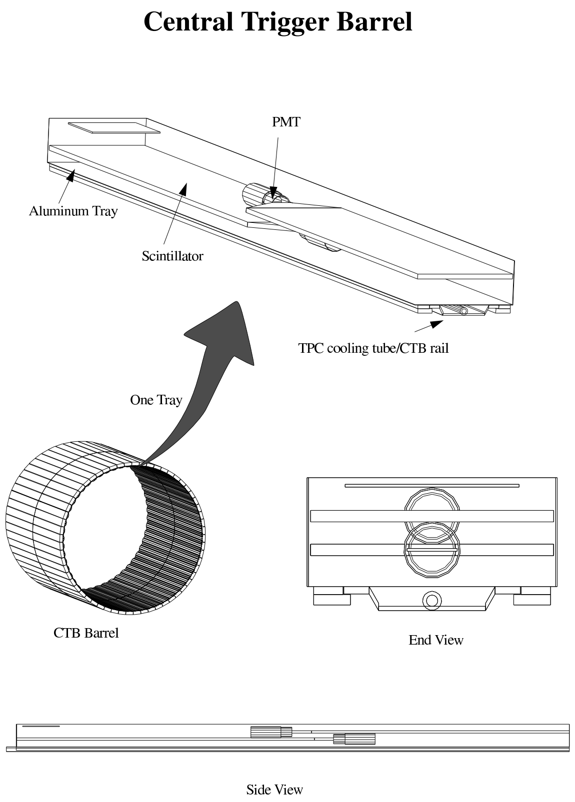

Figure 3.1. The layout of the Central Trigger Barrel (CTB) and one of the its trays [8]. One tray covers $\Delta\phi \times \Delta\eta = 0.1 \times 0.5$.

If we look at the distribution of the CTB signals, we can see a rather curious shape (Figure 3.2). This sharp cutoff/rise around CTB $\sim$ 1300 is due to the way the trigger was set up. The low CTB signals were detected by the ZDC trigger. The sharp rise in the acceptance indicates the point where the CTB trigger is turned on.

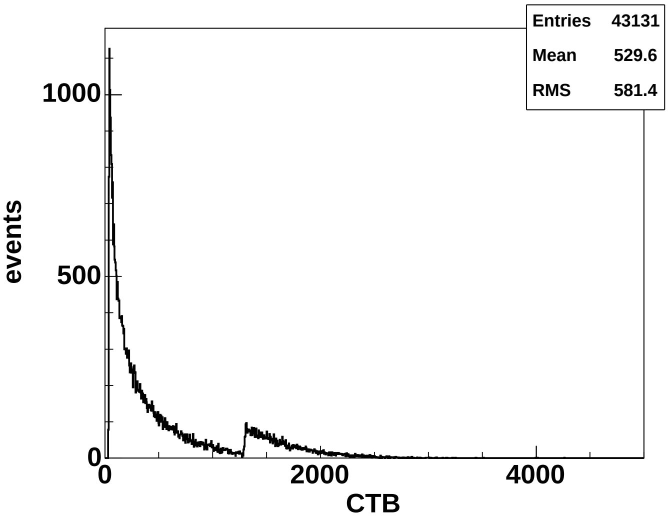

Figure 3.2. The distribution of CTB signals.

The two RHIC ZDCs are hadronic calorimeters, located in the zero-degree region along the beamlines on each side of the TPC. The locations of the ZDCs are shown in Figure 3.3. The ZDCs monitor the primarily-spectator neutrons which are released from the colliding nuclei. The neutrons can be detected in the ZDCs if they diverge by less than 2 milliradians from the beam axis.

There are three modules in each ZDC. Each module consists of layers of tungsten (W) plates, layers of plastic scintillators, wavelength shifting fibers, and a photomultiplier tube (PMT). The transverse dimensions of the plates are 10 cm × 13.6 cm. The downstream neutrons shower hadronically inside the ZDC and generate secondaries such as pions and nucleons. The fibers absorb scintillated photons and emit longer-wavelength photons to be detected by the PMT. The analog sums of the three PMT signals are called "ZDCe" and "ZDCw" for the east and west side, and are read

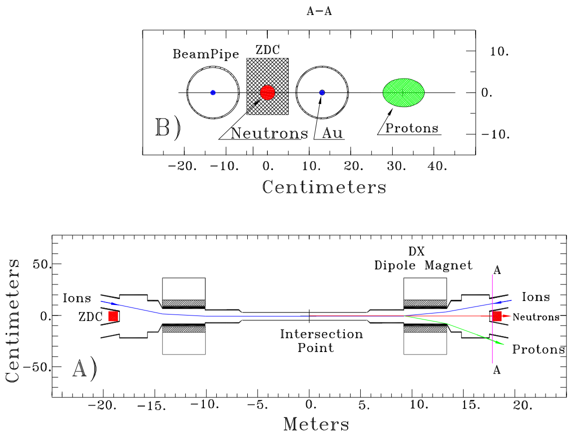

Figure 3.3. The Zero Degree Calorimeter location layouts [9]. Top: beam axis view. Bottom: side view.

out by the CTB Digitizer Board.

The average signals for the 19.6 GeV collisions is 2.9 on the west ZDC and 3.4 on the east ZDC (Figure 3.4). The source of the discrepancy is not known.

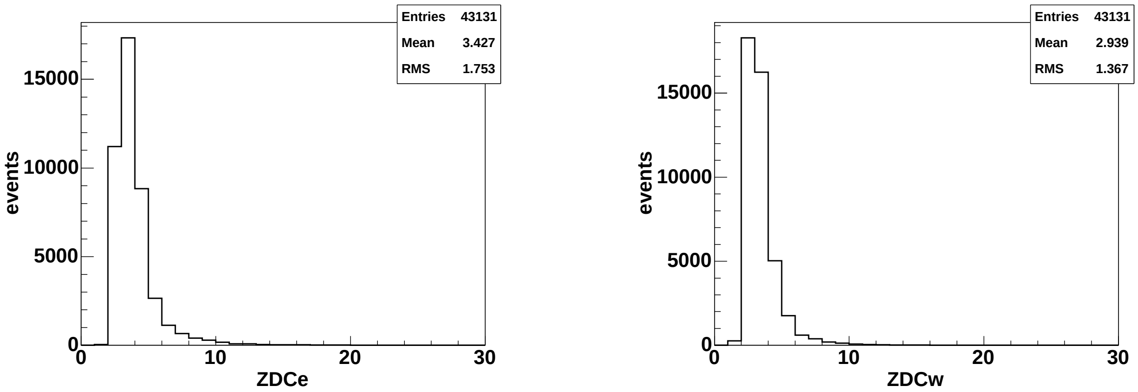

Figure 3.4. The distributions of ZDC signals.

The data for this study are taken using a minimum bias trigger which includes the whole range of collisions from peripheral to central [2]. The trigger required a coincidence of neutron signals in the two ZDCs. The trigger also required an event to have greater than 15 charged tracks in the CTB.

---

[2] The trigger name is “minBias22GeVZDC” and The data production version is “P02ge.”

3.2 Event Selection

The data came from RHIC Run II in year 2001. Not all the runs were analyzed. We referred to the run log to see which runs contain good data. For this analysis, the following run numbers were selected: 2329088, 2329089, 2329091, 2329092, 2329093, 2329094, 2329100, 2329101, 2330002, 2330003, 2330003, 2330004, and 2330005 [3].

Next, we looked at the locations where the events occurred. The x and y positions of the events come from the track and vertex reconstruction. The event's z coordinate comes from the (drift length) = (drift time) × (drift velocity). The drift velocity (v_{drift}) is obtained by doing a TPC laser [137] calibration before each run. A laser run between runs 2329089 and 2329091 indicated that $v_{\text{drift}} = 5.542$ cm/μs.

The distributions of vertex positions in transverse and longitudinal directions are shown in Figures 3.5 and 3.6 (z is the beam axis). The 1-mm thick beryllium beampipe at the radius 3.81 cm is visible in the xy vertex plot. The z vertex distribution peaks at the center of the TPC and can be fitted with a Gaussian function. The width of the vertex distribution has to do with the bunch geometry of the beam. For comparison, the 19.6 GeV distribution, with a root-mean-square (RMS) of about 86 cm, is much broader than the distribution of the 62.4 GeV Au+Au run, which has an RMS ≈ 30 cm. A diamond length of RMS < 20 cm is the optimum goal [4]. The shape can also be attributed in part to trigger conditions.

We chose to analyze the events at the center of the TPC. If we choose an event too far away from $z = 0$ cm, forward tracks would have few hit points and may not pass the track selection. This would compromise the characterization of the event. The cut of $|z| < 30$ cm was applied to the data. This ensures a uniform detector acceptance for the tracks within $|\eta| < 1.0$ ($\theta \approx 40^\circ$) for all the vertices.

To avoid recording events from beam-gas and beam-material interactions, we also

---

[3] By a STAR convention, the first number refers to the year the experiment was run (year 2 in our case), the next three represent the day the run was issued (329 and 330 correspond to November 25 and 26), the last three give us the order of the run in that day.

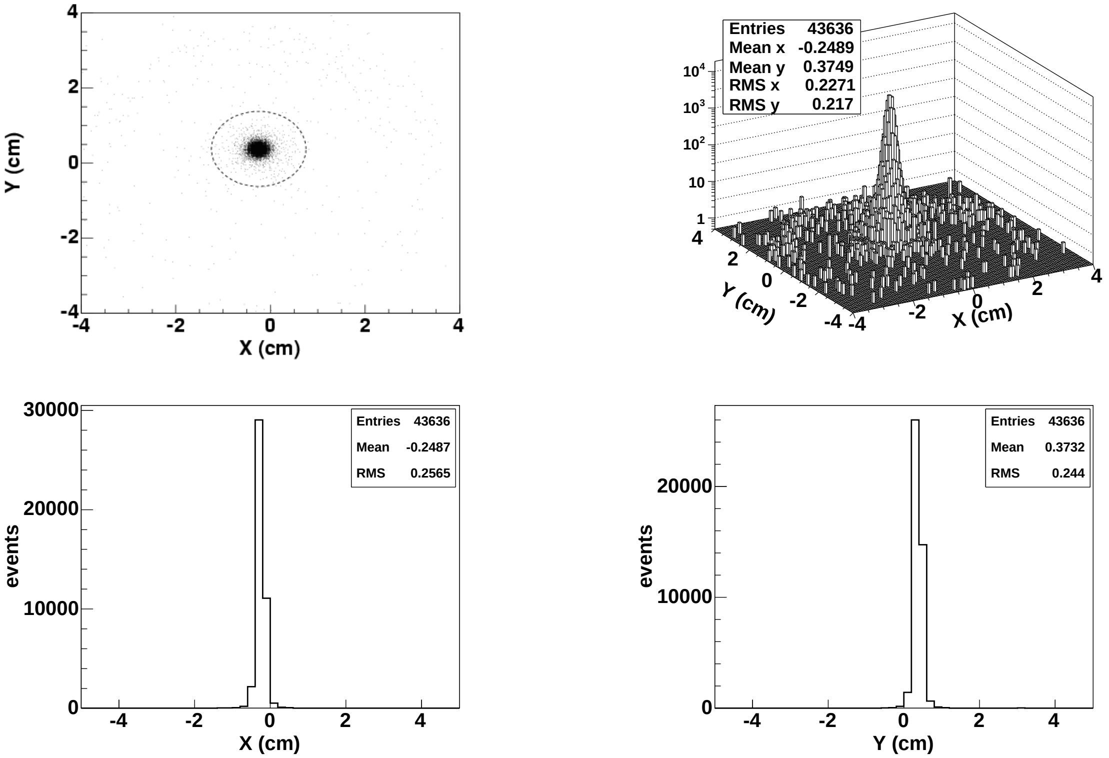

Figure 3.5. Vertex positions in xy (transverse) plane. We chose events inside the 1-cm radius circle, indicated by the dashed line in the top-left panel. The top-right panel provides a view of the distribution magnitude. Lower figures show distribution of x and y vertices separately. The data shown here have the z vertex cut applied.

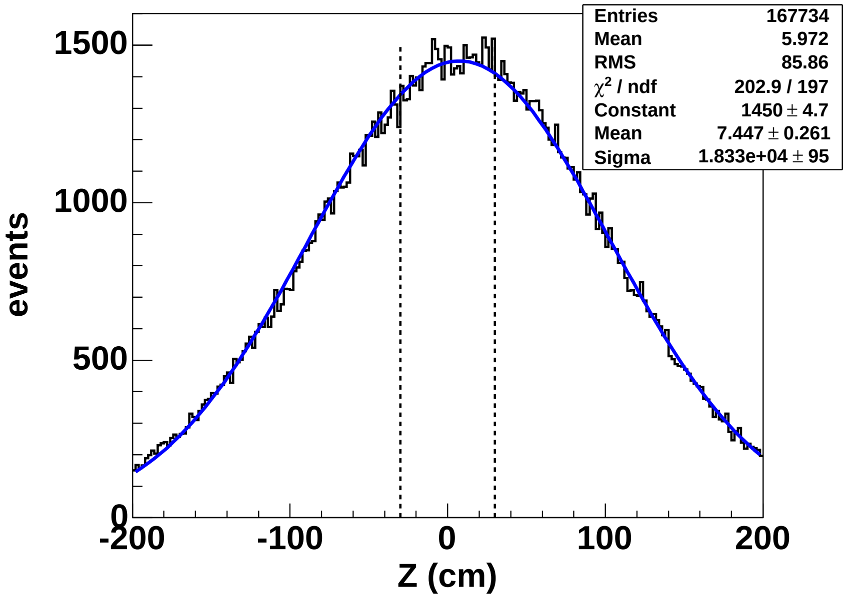

Figure 3.6. Vertex positions along the z (beam) axis. We select events that occur ±30 cm away from the center of the TPC. The solid line is a Gaussian fit to the data. The data shown here has the xy vertex cut applied.

required events to be within the radius of 1 cm from the vertex distribution mean; a circle cut, $(x+0.246)^2+(y-0.378)^2 < 1$, was applied. As a reminder, the beampipe's radius is 3.81 cm.

25.3% of events pass the vertex z cut and 97.4% pass the vertex xy cut. Together, the vertex cuts pass 25.0% of $\sim$172k recorded events, leaving 43,131 for the analysis. As will be seen later, there are roughly 5k events in top 10% centrality cut. As a comparison, the NA49 experiment has the events statistics of approximately 400k for top 5% central events [13].

3.3 Centrality Determination

Centrality is related to the nuclear impact parameter (b) which is the geometrical distance between the centers of two colliding nuclei. A more central collision will have a smaller impact parameter (larger overlap area). In a nucleus-nucleus collision, the impact parameter is in a scale of fermi (10^{-15} m) and cannot be measured experimentally. Therefore, we must use some other practical experimental observables that correlate with the impact parameter to define centrality.

The observable which we used to determine the collision centrality is the uncorrected reference multiplicity (N_{ch}). N_{ch} is defined as the number of produced charged particles with at least 10 fit points, within central pseudorapidity of $|\eta| < 0.5$ (corresponding to $\theta \approx \pm 62.5^\circ$), and having a distance of closest approach (DCA) between the track and primary vertex within 3 cm. The $|\eta|$ requirement is necessary to ensure that the centrality estimate does not vary with the z coordinate of the vertex. The DCA requirement eliminates most secondary interactions and decays. N_{ch} will be larger in central events than in peripheral events.

The way we divide N_{ch} is to use previous STAR measurements from higher energies. The scaled N_{ch} distributions for 19.6, 130 [30], and 200 GeV systems measured by STAR are shown in Figure 3.7. We scale the x (N_{ch}) axis and y (number of events) axis at 130 and 200 GeV to the 19.6 GeV maxima. The shapes of the two high energy data–also the 62.4 GeV data (not shown)–match each other very well. However, the 19.6 GeV data, while matching the higher energies well in most part, show dips in some regions.

The dips are thought to be due to trigger bias. The STAR trigger was not optimized for low energy runs. Low energy beams have small longitudinal momentum and are more spread out in the transverse plane [4]. The detection is not equally efficient for collisions of different centrality. The trigger is especially inefficient for very peripheral collisions, the spectator neutrons with small longitudinal momenta may get absorbed into small nuclei, such as deuterons, tritons, helions, and alphas and do not get to the ZDCs. As a result, detection efficiency goes down for this type of collisions. The shape of the CTB signal distribution in Figure 3.2, which shows significant dips in the mid-central and the lowest multiplicity regions, may be related to this N_{ch} shape.

We used the N_{ch} cuts of the scaled 130 GeV data to determine the centrality at 19.6 GeV. The centrality classes for 19.6 GeV Au+Au events were determined by multiplying the 130 GeV N_{ch} cut values [30] by the x axis scaling factor, ~ 0.652, and rounded to nearest integers. The events were divided into five centrality classes: 0-10%, 10-30%, 30-50%, 50-70%, and 70-100% most central. The percentage indicates the fraction of the multiplicity ($\propto$ cross section) in that bin versus total multiplicity. The final cuts are shown in Table 3.1. (The numbers for the 130 GeV analysis have since changed, as indicated in the Table; however, the changes are relatively small.) The numbers of events in each centrality bin are summarized in Table 3.2.

The uncorrected pseudorapidity distribution for different 19.6 GeV centrality classes are shown in Figure 3.8, with a comparison to the 62.4 GeV system. In

---

[4] This dispersion causes lower-energy beams to have lower lifetimes, because their luminosities drop faster.

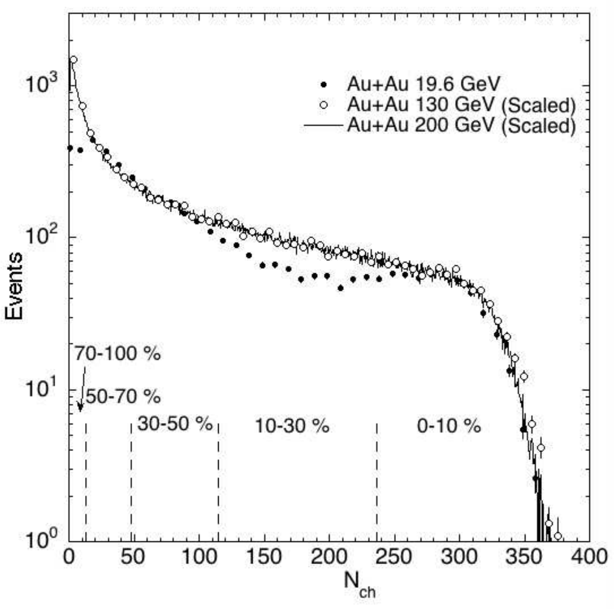

Figure 3.7. Multiplicity distributions of Au+Au collisions at three energies: 19.6 (dots), 130 (open circles), and 200 GeV (solid line). Dashed vertical lines indicate the centrality cuts used in this analysis.

centrality	STAR 130 GeV N_{ch}	STAR 19.6 GeV N_{ch}
5%	431 (424)	281
10%	364 (357)	237
20%	260 (255)	170
30%	179 (175)	117
40%	118 (115)	76
50%	74 (71)	48
60%	43 (41)	28
70%	22 (20)	14
80%	10 (9)	7

Table 3.1. Centrality determined by multiplicity N_{ch}. The numbers in parentheses are the 130 GeV latest numbers.

centrality	number of events
0-10%	5106
10-30%	8033
30-50%	11947
50-70%	13059
70-100%	4986
total	43131

Table 3.2. Number of events in different centrality bins.

the plots, similar event and track cuts were applied to both datasets. The shapes between the two energies are very close. The 19.6 GeV most central collisions seems to have a more visible dip in the midrapidity region ($y = 0$).

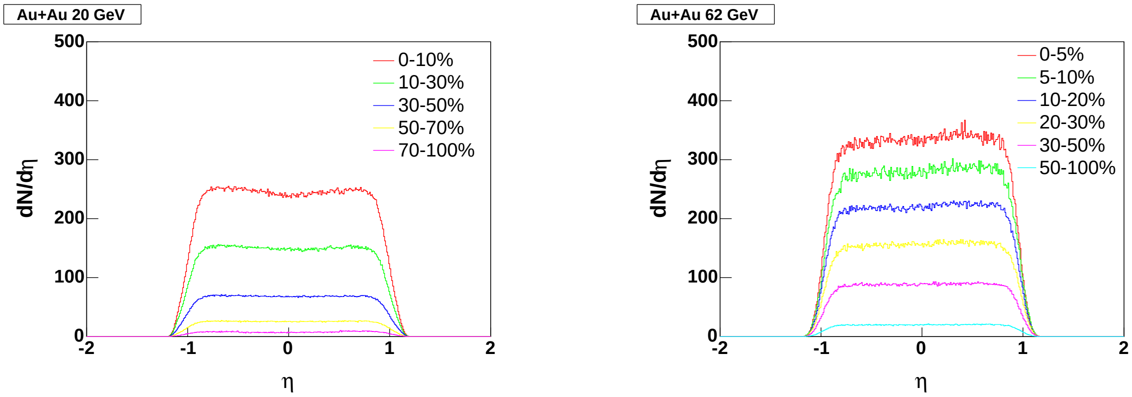

Figure 3.8. Raw $dN/d\eta$ distributions from Au+Au collisions at 19.6 (left) and 62.4 (right) GeV for various centralities.

3.4 Track Selection

To study inclusive particle spectra, we want to choose only the particles that were produced from the primary vertex. To minimize the number of particles from secondary vertices, a cut of 3 cm was applied to the distribution of the distance of closest approach between the tracks and the event vertex. For the quality of the fit, we selected tracks with χ^2 per degree of freedom of the helix fit (Figure 3.9) to the found points less than or equal to 2.5. About 91% of the tracks pass this χ^2 cut.

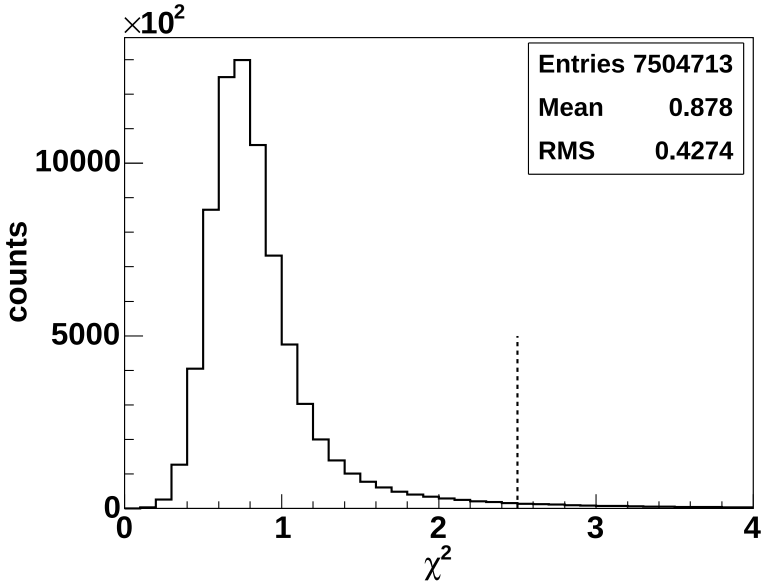

Figure 3.9. Distribution of the χ^2 per degree of freedom from the track fitting. The tracks in the plot pass all the other necessary cuts (except the χ^2 cut itself).

The total number of points used in the fit (Figure 3.10) was required to be greater than or equal to 25 to eliminate short tracks, which are probably split tracks. The maximum possible number of fit points is 45, one for each anode pad row. 31.8% of the tracks have less than 25 fit points and were removed by this cut.

Finally, the fractions of points used in the fit, or "tracking percentage," (Figure 3.11) was required to be greater than or equal to 0.51 the maximum fit points to prevent overcounting of split tracks (one track but counted as two). The maximum points are the number of points that could be used to fit the track if the TPC were infinitely long. A large number of long tracks do not have 45 hits on the pad rows due to their orientations with respect to the TPC. Comparison of the distributions of fit points and maximum points are shown in Figure 3.12. Almost all the tracks (98.8%) pass this tracking percentage cut.

To summarize, we applied the following cuts to our data:

- Event cuts:

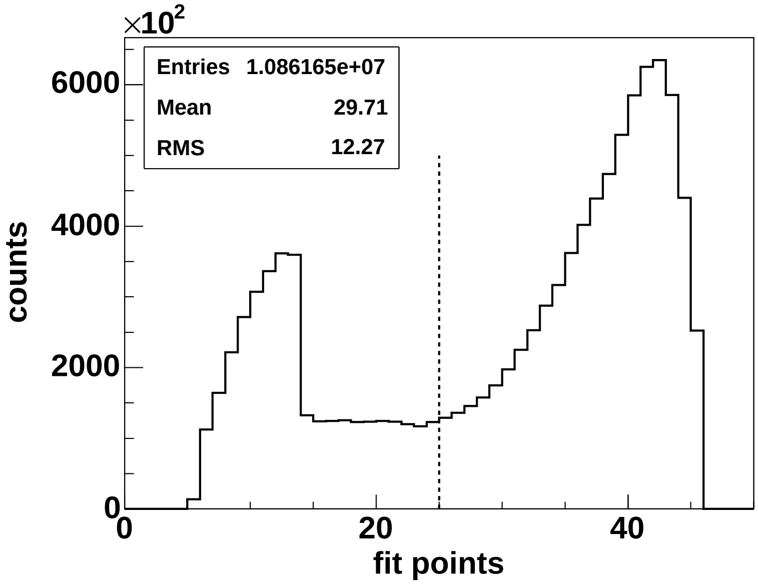

Figure 3.10. Distribution of the number of fit points per track after the event cuts and χ^2 cut. Dashed line is the cut. (The entire distribution is shown but in the analysis the tracks with less than 25 fit points are excluded.)

  - z-location of vertex: $|z| < 30$ cm
  - radius from beam center: $(x + 0.246)^2 + (y - 0.378)^2 < 1.0$ cm
  - N_{ch} classified into 5 bins

- Track cuts:
  - fit points ≥ 25
  - χ^2/d.o.f ≤ 2.5
  - $0.51 \leq \frac{\text{fit points}}{\text{max points}} \leq 1.05$
  - global DCA ≤ 3.0 cm

Other track characteristics are shown in Figure 3.13. The structure of ϕ distribution is due to the acceptance of anode sectors. (There are 12 sectors on each side of the TPC, with small spacing between them.) A greater number of positive tracks than

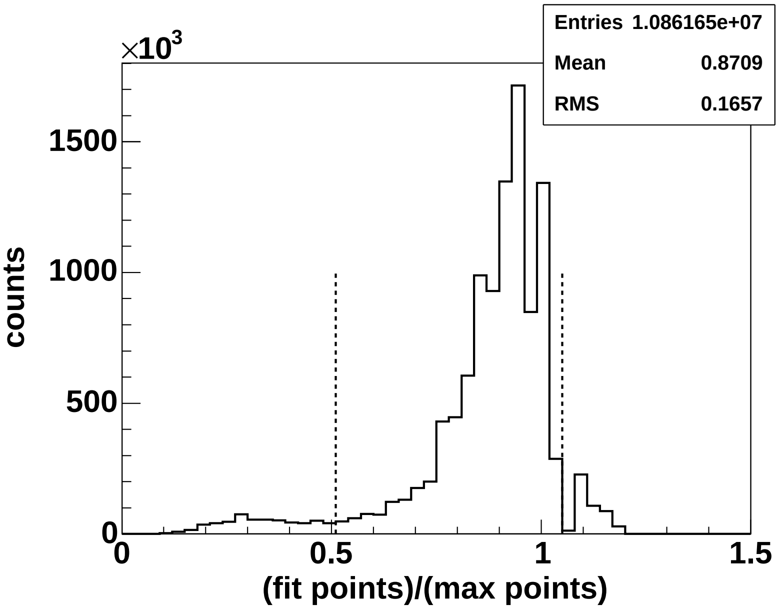

Figure 3.11. Distribution of the ratio between the number of fit points and maximum fit points after the event cuts and χ^2 cut. Dashed lines are the cuts. The entire distribution is shown but data used in the analysis have a cut of $0.51 \leq \frac{\text{fit points}}{\text{max points}} \leq 1.05$ applied.

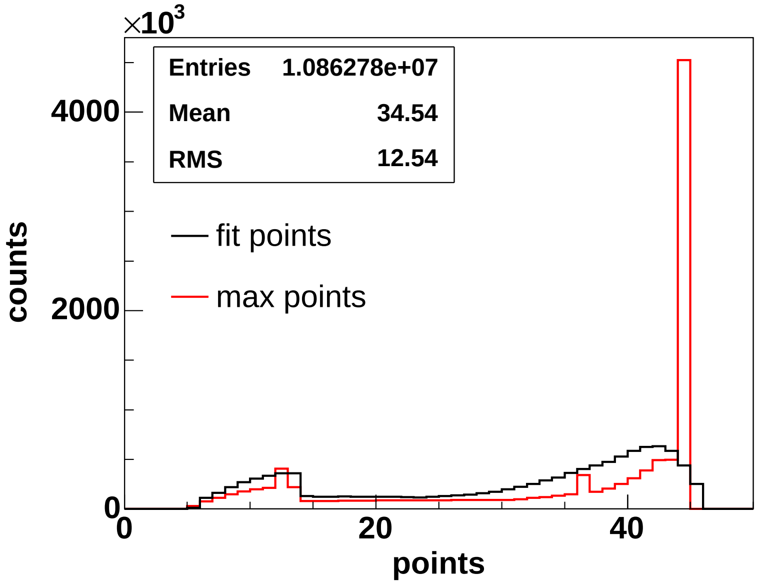

Figure 3.12. Distributions of the number of fit points (black) and maximum fit points (red) after the event cuts and χ^2 cut. The data used in the analysis have a cut of $0.51 \leq \frac{\text{fit points}}{\text{max points}} \leq 1.05$ applied.

negative tracks follows conservation of charge (initial charge for one nucleus-nucleus collision is $= +158$). We see that most tracks are about 2 m long.

3.5 Detector Acceptance

STAR has a wide symmetric range of coverage which makes it especially efficient in study physics near midrapidity. Figure 3.14 shows the detector acceptance in rapidity-transverse momentum space for the three particle species.

A particle is detected by the Time Projection Chamber if it can produce enough hits. The shapes in Figure 3.14 can be interpreted as follows. At low p_T, the three particle species have a similar p_T cutoff. The number of fit points required, which determines the minimum radius of curvature, directly influences this cutoff. The shape of the distribution at low p_T is a result of kinematic effects. While the η

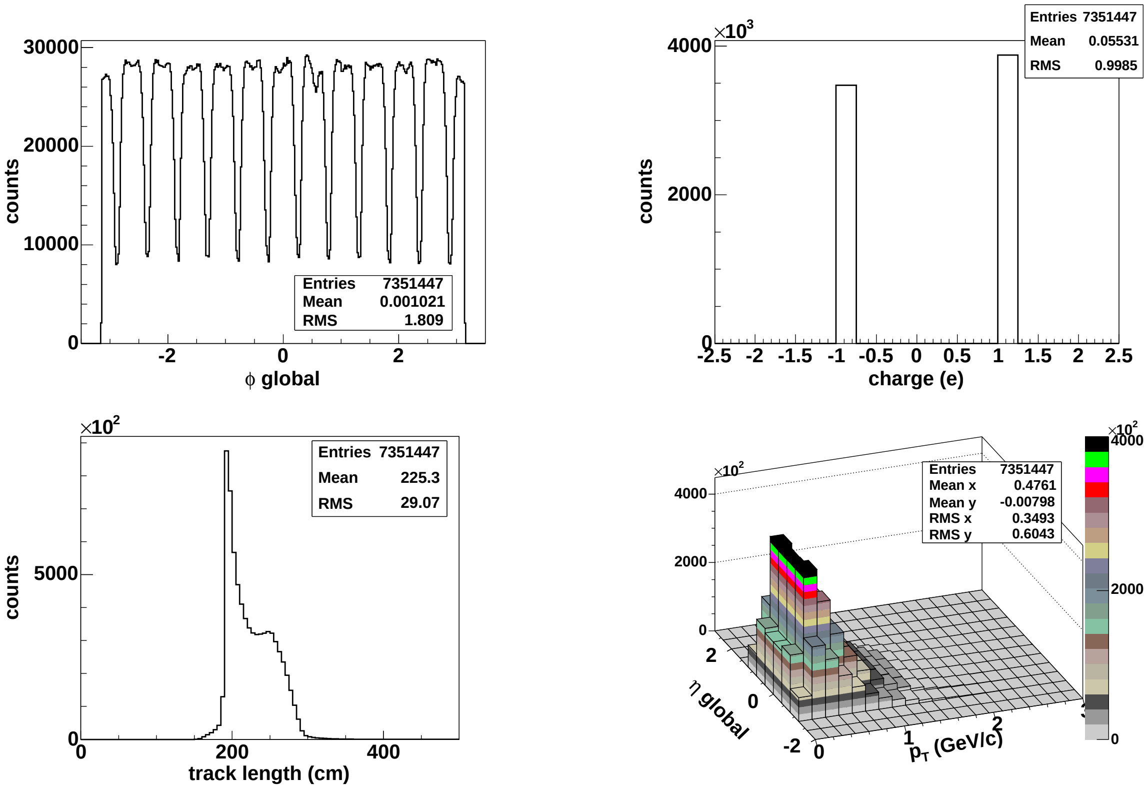

Figure 3.13. Distributions of ϕ (top left), charge (top right), track length (bottom left), and η vs. p_T (bottom right), after all the event and track cuts.

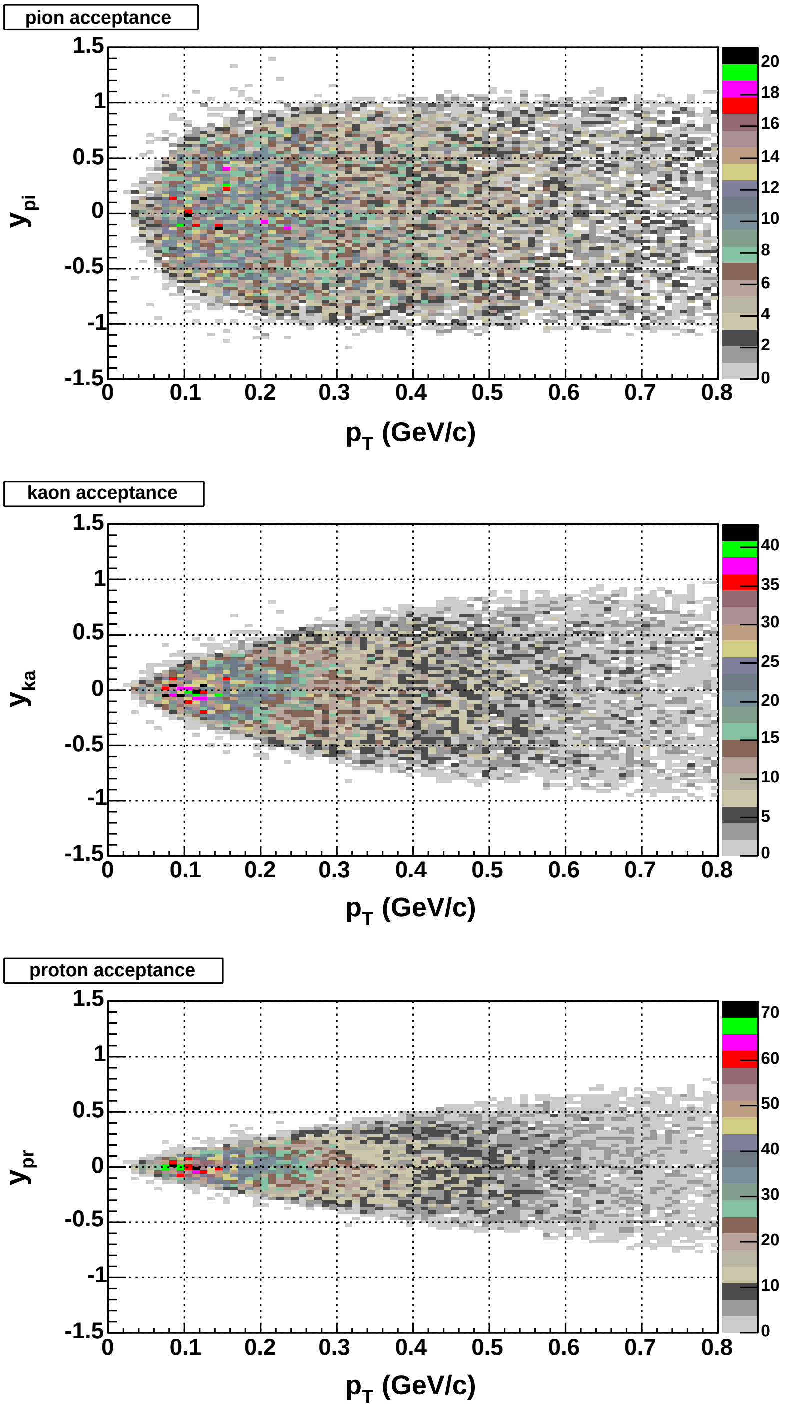

Figure 3.14. The STAR detector rapidity and transverse momentum acceptance for the 19.6 GeV Au+Au run. From top to bottom are: pions, kaons, and protons. The tracks are required to have at least 25 fit points.

acceptance is identical for any projectile, the y acceptance has a mass dependence in it. To see the effect, we can plot η vs. y from the relation between rapidity and pseudorapidity,

$$\eta = \sinh^{-1}\left(\frac{\sqrt{m^2 + p_T^2}}{p_T}\sinh(y)\right) \tag{3.1}$$

As illustrated in Figure 3.15, for the same η range, the particle with a smaller mass has a wider y range than that of a larger-mass particle.

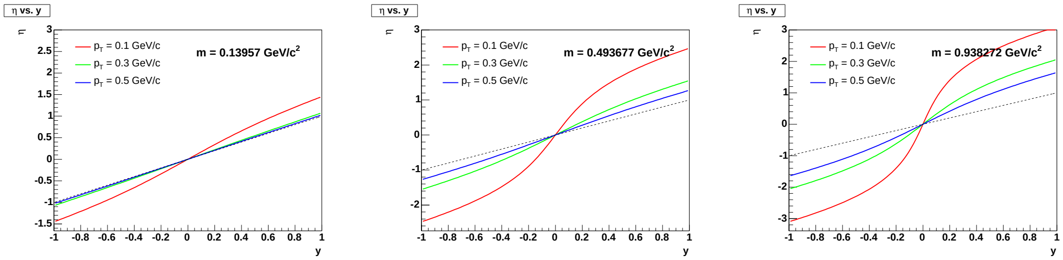

Figure 3.15. Pseudorapidity versus rapidity at various p_T and masses. From left to right are pion, kaon, and proton mass.

Chapter 4

Particle Identification

To study the properties of the particles, we first have to know what particles were produced. Therefore, particle identification (PID) is the very important first step. In this chapter, we describe how the PID process was done.

4.1 Energy Loss Through Medium

When a charged particle traverses through matter, in our case a P10 gas, it interacts with electrons, protons, neutrons inside the matter. If the projectile particle is relativistic enough ($\beta\gamma \approx 0.3 - 10$), the energy loss is mainly due to ionization of the gas. The released electrons (sometimes called δ-electrons) drift toward the readout planes. The total ionization can be measured from the summed charges of the electron clusters along the particle's trail. The ionization losses per unit length (dE/dx) are sampled from different clusters of the track. A single particle trajectory can yield up to 45 dE/dx samples onto the 45 pad rows.

More specifically, the amount of the energy loss can be measured using the signal heights on the anode pads. For a given cluster, the signals are summed over all pads. For each hit on the pad row, the summed signal is divided by the track length across the row to yield dE/dx.

The energy loss per unit length is stochastic in nature, due to the frequent collisions between the particle and gas atoms. dE/dx can go from a few tens of eV to hundreds of eV in rare processes. Therefore, due to this random nature of the interactions, the energy loss distribution has a Landau shape [43, 138] with a long tail towards the high ionization region. An integral to infinity of a Landau distribution is divergent. Therefore, the averaged energy loss of this Landau distribution cannot be defined. The largest ionization samples are therefore truncated, resulting in a nearly Gaussian dE/dx distribution.

The mean energy loss per unit length (also called "specific energy loss" or "stopping power") of a heavy ($m \gg m_{\text{electron}}$) particle can be explained by the Bethe-Bloch formula [43] (equation (4.1)). The formula is constructed based on the Coulomb interaction between the charged particle and the medium. The information of energy loss inside the TPC is used to identify the produced particles, i.e., to identify the species of particle (pion, kaon, proton, etc.) that produced the given track.

$$-\frac{dE}{dx} = \frac{N_{\text{A}} e^4 z^2 Z}{2\pi\epsilon_0^2 m_e c^2 A}\frac{1}{\beta^2}\left(\ln\frac{2m_e c^2\beta^2\gamma^2 T_{\text{max}}}{I^2} - 2\beta^2 - \delta\right) \tag{4.1}$$

where:

- N_{A} ($= 6.022 \times 10^{23}$) is the Avogadro's number,
- e ($= 1.6 \times 10^{-19}$ C) is the magnitude of electron charge,
- z is the charge number of the projectile,
- Z is the atomic number of the absorbing material,
- ϵ_0 ($= 8.854 \times 10^{-12}$ F/m) is the permittivity constant of vacuum,
- m_e ($= 0.511$ MeV/c^2) is the electron mass,
- A is the mass number of the absorbing material, and

- $T_{\max}$ the maximum kinetic energy per collision which can be transfered to a free electron; it is given by

  $$T_{\max} = \frac{2m_ec^2\beta^2\gamma^2}{1 + 2\gamma m_e/m + (m_e/m)^2} \tag{4.2}$$

  where I is the mean excitation energy, which is the average energy needed to remove an electron from an energy level to an unoccupied one or from the atom entirely,

- β and γ are the standard relativistic variables associated with the projectile's velocity.

- δ is the density effect correction which results from the medium becoming polarized by a fast particle. For argon, this correction only becomes significant when $\beta\gamma > 80$ [118].

Note that the γ and the magnitude of charge of a particle completely determine dE/dx in a given material.

Compared to heavy ions, the energy loss of electrons is more complicated due to their light mass and relativistic speeds. In addition to ionization, an electron traveling through material loses its energy via Bremsstrahlung radiation [43]. The amount of radiation loss is magnified at high energies. Due to its light mass, electron usually shows up at high $\beta\gamma$ region. We parametrized the $dE/dx(\beta\gamma)$ function to include the electrons. Having the information on the electron dE/dx centroids has a practical purpose of fitting the electron dE/dx distributions.

From equation (4.1), one can see that the rate of the energy loss depends on the incident particle's velocity. For a given momentum p, particles with different masses will lose different amounts of energy. Total p is calculated from p_T using the relation $p = p_T/\sin\theta = p_T/\sin[2\tan^{-1}(e^{-\eta})]$. Charge-wise, dE/dx depends on the square of the incident particle's charge z, but linearly on the atomic nuclear charge Z.

Using the Bethe-Bloch formula [1], Figure 4.1 shows the predicted dE/dx as a function of momentum for particles of different masses (pions, kaons, protons, deuterons, and muons). dE/dx is predicted by the formula to be identical for positively and negatively charged particles. Figure 4.2 shows the energy loss of the particles from the real 19.6 GeV data; rigidity (p/z or $m \times \beta \times \gamma$) is used as the horizontal axis. We can clearly see distinct bands of particles where rigidity is small. As expected, dE/dx is relatively symmetric for negative and positive particles.

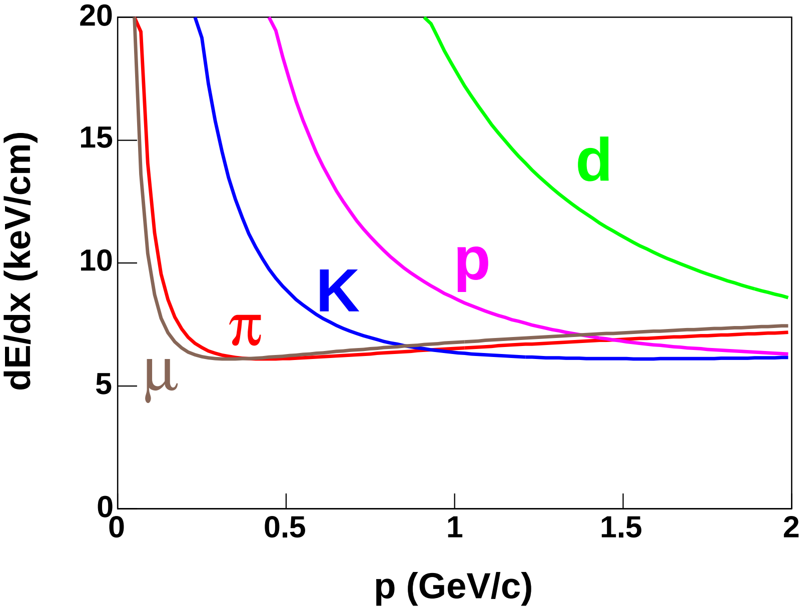

Figure 4.1. Bethe-Bloch dE/dx vs. p for π, K, p, d, and μ.

As seen in Figure 4.3, the particle energy loss for three different systems (200 GeV p+p, 200 GeV Au+Au, and 19.6 GeV Au+Au) are similar. Of course, it is this uniqueness of dE/dx-vs.-p shape that makes particle identification possible in the low momentum region. The lines in the figure are Bichsel dE/dx calculations for the P10 gas (explained in [43]).

---

[1] The matter is assumed to be argon, and the mean excitation (I) is approximated to be (10 eV)$\cdot Z_{\mathrm{Ar}}$. The density effect is assumed to be zero.

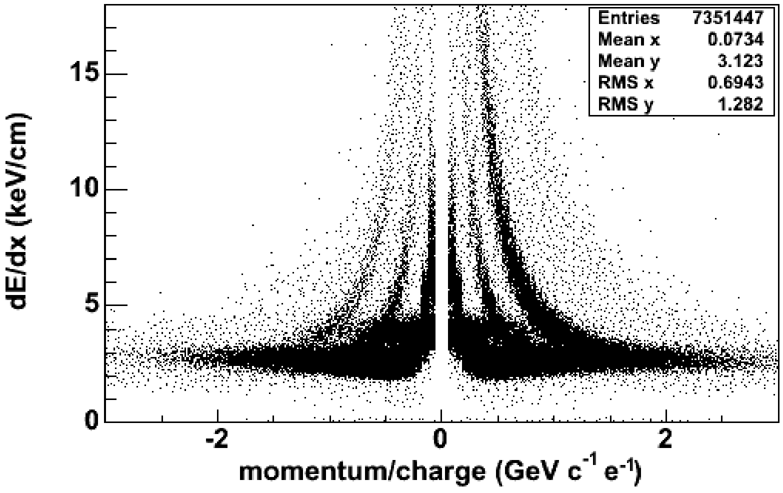

Figure 4.2. dE/dx vs. rigidity of charged particles from 19.6 GeV Au+Au events (minimum bias).

4.2 Extracting Yields

From a particle's track curvature inside the magnetic field (B), the detector gives us the particle's transverse momentum (from $\vec{p}_T \perp \vec{B}_z$ and assuming |charge| = 1). To extract a particle yield in a certain region of transverse mass ($m_T - m_0$) and rapidity (y), both of which have a mass dependence, we imposed a mass (m_0) value to p_T to obtain $m_T - m_0$ and y. We studied pions, kaons, and (anti)protons, therefore the mass m_0 is selected as one of these three possible values. The value used is the one that gives the measured dE/dx for the measured momentum. The values of y and m_T are calculated from this mass that best matches the measured dE/dx.

We analyzed the distribution of dE/dx in each transverse mass ($m_T - m_0 \equiv \sqrt{p_T^2 + m_0^2} - m_0$) slice, for each mass assumption. In addition to the transverse mass cuts, we also made cuts in rapidity space.

For a given m_0, only the yield of the particle with that mass is extracted. We first divided $m_T - m_0$ range between 0 and 1 GeV/c^2 evenly into 40 bins, resulting in bins of size $\Delta(m_T - m_0) = 0.025$ GeV/c^2. We studied the rapidity range between

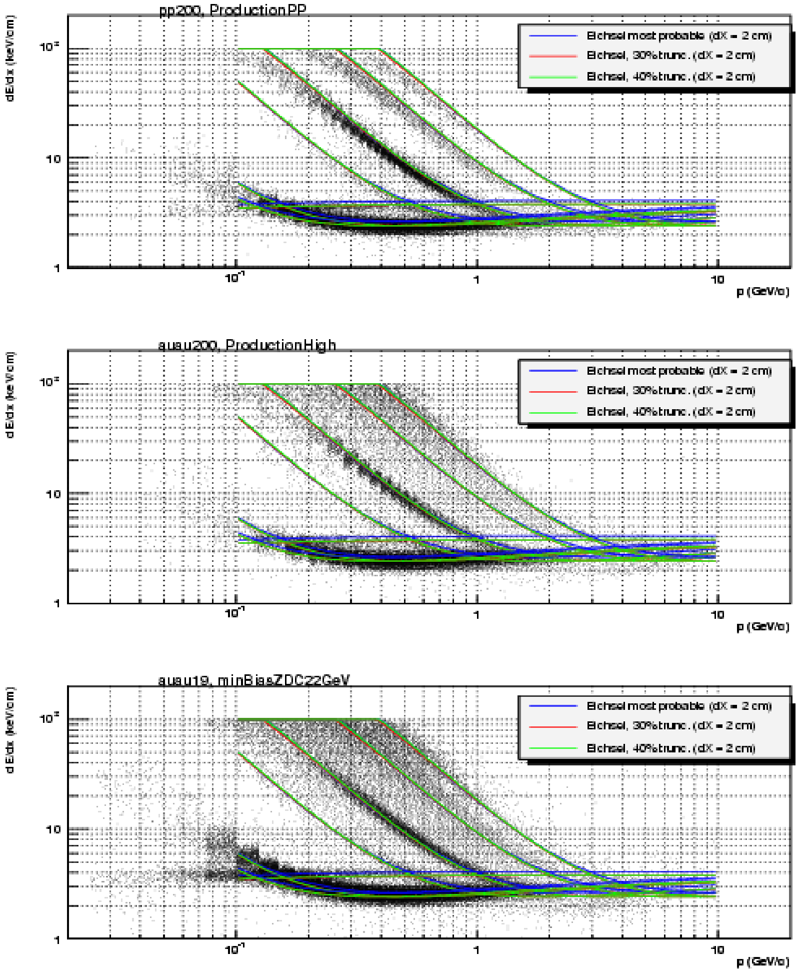

Figure 4.3. dE/dx vs. momentum for three different collision systems measured by STAR. Shown are, from top to bottom, 200 GeV p+p, 200 GeV Au+Au, and 19.6 GeV Au+Au. The lines are Bichsel calculations for different particle species.

-0.5 to 0.5. A bin width of $\Delta y = 0.2$ was used. In each $(m_T - m_0, y)$ bin, we plotted the distribution of the function of energy loss (dE/dx):

$$f(dE/dx) = 2.8 \times \ln\left(\frac{dE}{dx} \times 10^6\right) + 1.5 \tag{4.3}$$

where dE/dx has a unit of GeV/cm. The two constants, 2.8 and 1.5, in our function are arbitrary scale factors chosen for legibility of the plots.

In each transverse mass bin, we fitted the $f(dE/dx)$ histogram with four standard Gaussians. Each Gaussian function, which corresponds to each of the four charged particle species (π, K, p, and e), is defined as

$$y = A \exp\left[-\frac{1}{2}\left(\frac{f(dE/dx) - c}{\sigma}\right)^2\right] \tag{4.4}$$

with y being the count, A the amplitude, c the centroid, and σ the width.

The mean value (centroid) of dE/dx in each $m_T - m_0$ slice is what we want to parametrize as a function of $\beta\gamma$.

After preliminary fits, where dE/dx centroids still act as free parameters, we have four dE/dx centroid values in each $m_T - m_0$ bin. Knowing $m_T - m_0$ and rapidity, y, we can calculate the corresponding $\beta\gamma$.

We inspected the dE/dx Gaussian distributions and, for each particle species, selected $m_T - m_0$ slices in which the particle dE/dx peak is well separated from the other species.

After collecting ($\beta\gamma$, dE/dx) data points, a parametrization of the Bethe-Bloch formula was used to calibrate dE/dx. The parametrized form of the Bethe-Bloch equation, which was derived from the work done by Aihong Tang [139], is

$$y = m_1 \times \left(1 + \frac{1}{x^2}\right)^{m_2} \times \left(\left|ln(m_3 \times x^2)\right|^{m_4} + m_5 \times (1 + \frac{1}{x^2})^{m_6}\right) - m_7 \tag{4.5}$$

where $y \equiv dE/dx$ and $x \equiv \beta\gamma$. Initial parameter values, which are empirically obtained from one of the fits, are: $m_1 = 1.2403$ keV/cm; $m_2 = 0.31426$; $m_3 = 12.428$; $m_4 = 0.41779$; $m_5 = 1.6385$; $m_6 = 0.72059$; $m_7 = 2.3503$ keV/cm.

Ideally, we want to have a set of free parameters that is same for different systems and cuts. Before the parametrization was used in this 19.6 GeV study, we tested different parameter sets with the data from 19.6, 130, and 200 GeV Au+Au, and 200 GeV p+p.

Note that while the Bethe-Bloch equation only describes energy loss of heavy particles ($m \gg m_e$), we want our parametrization to include electrons. This approach has two benefits: first, it restricts the dE/dx vs. $\beta\gamma$ fit curve and second, it allows the dE/dx distributions to be fitted with four Gaussian functions, so that the electron contaminations can be calculated.

Figure 4.4 shows an example curve of equation (4.5).

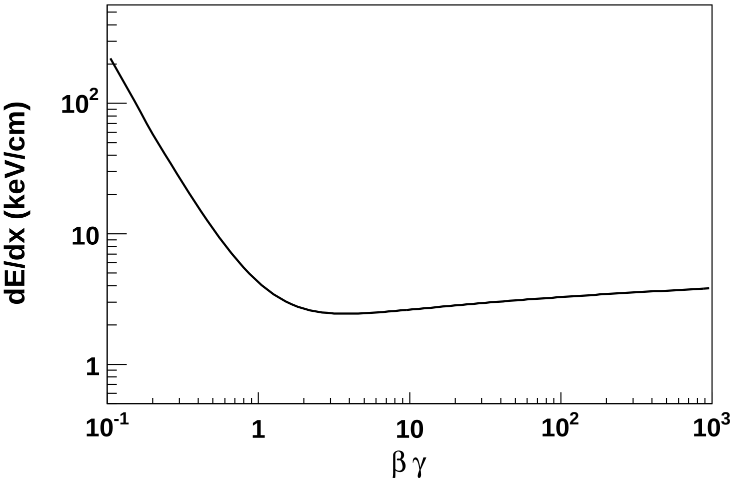

Figure 4.4. dE/dx as a function of $\beta\gamma$ from equation (4.5).

It was found that a set of three free parameters, m_3, m_4, and m_7, gives good fits for all systems. There is a different set of (m_3, m_4, m_7) for each bin of (y, m_T). The rest of the parameters (m_1, m_2, m_5, and m_6) are fixed at their initial values, independent of (y, m_T). The values are the same for all centrality, rapidity, and particle cases. This three-parameter fit was primarily used in this analysis, except when the statistics are low (such as the forward rapidity regions and the antiprotons from peripheral events), in which case five free parameters (m_1 and m_2 are the additional ones) were allowed.

Two examples of dE/dx vs. $\beta\gamma$ fits is shown in Figure 4.5. The data points are from $m_T - m_0$ slices where dE/dx centroids are well separated.

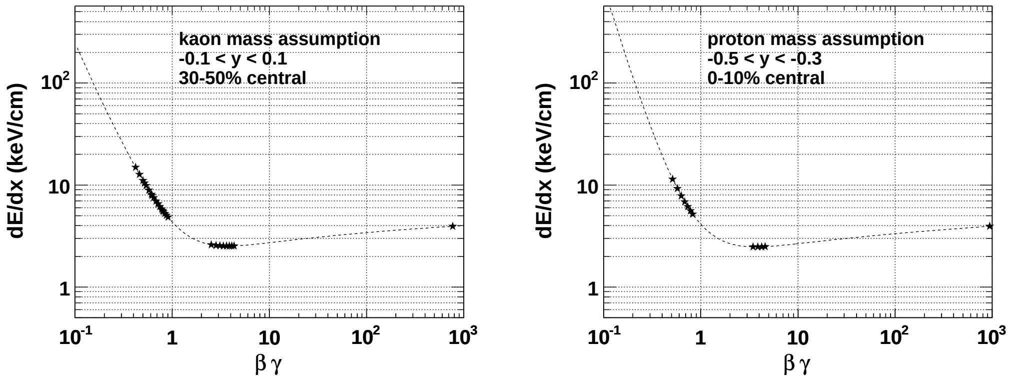

Figure 4.5. dE/dx as a function of $\beta\gamma$. The parametrized Bethe-Bloch function is used to fit the data. (Left plot: positive kaons. Right: antiprotons.) Note that the "mass assumption" only affects the rapidity selection and not the shape of the curve.

The particle identification process used in this study can be summarized by Figure 4.6.

The final fits were obtained by keeping fixed the centroid and width of each of the four Gaussians using the corresponding Bethe-Bloch parametrization. The amplitudes were left as the only free parameters. Figure 4.7 shows the final fits for one transverse mass region of midrapidity positively-charged particles, using pion mass assumption. The mass assumption affects how the dE/dx distribution looks. This is because in a given $(m_T - m_0, y)$ bin, a different m_0 assumption would yield different a $\beta\gamma$ value. From the Gaussian corresponding to the pions we extract pion yields in each transverse mass region (bin 12). A similar procedure using kaon and proton mass assumptions was used to extract yields for positive kaons and protons, other transverse mass and rapidity regions, and also for the corresponding negative species.

The fixing of the centroid and width parameters allowed us to extract the particle yields in some of the $m_T - m_0$ slices where there were significant overlaps of the dE/dx distributions. In such regions, if we were to leave all the Gaussian centroids as free

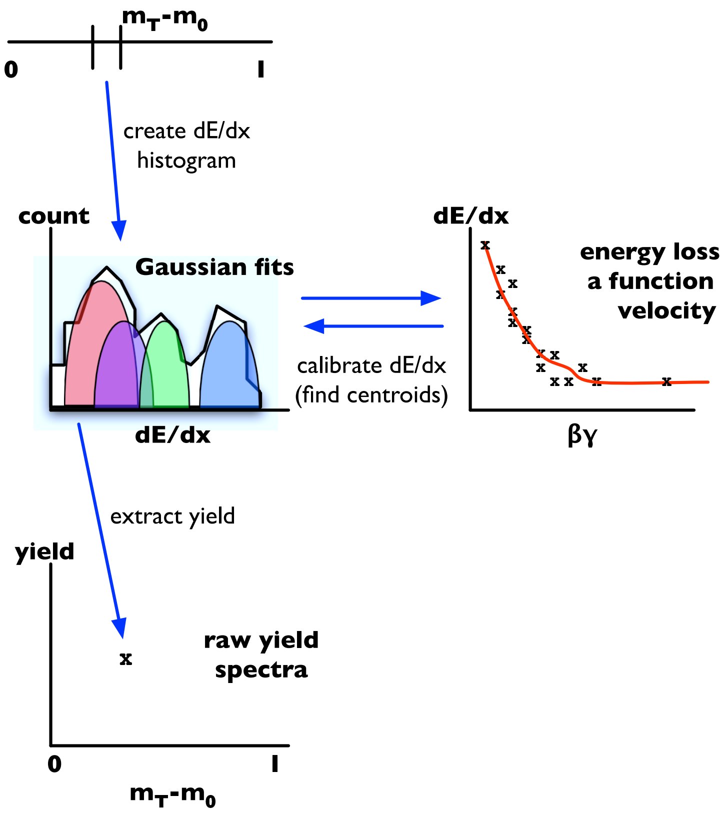

Figure 4.6. The PID flowchart.

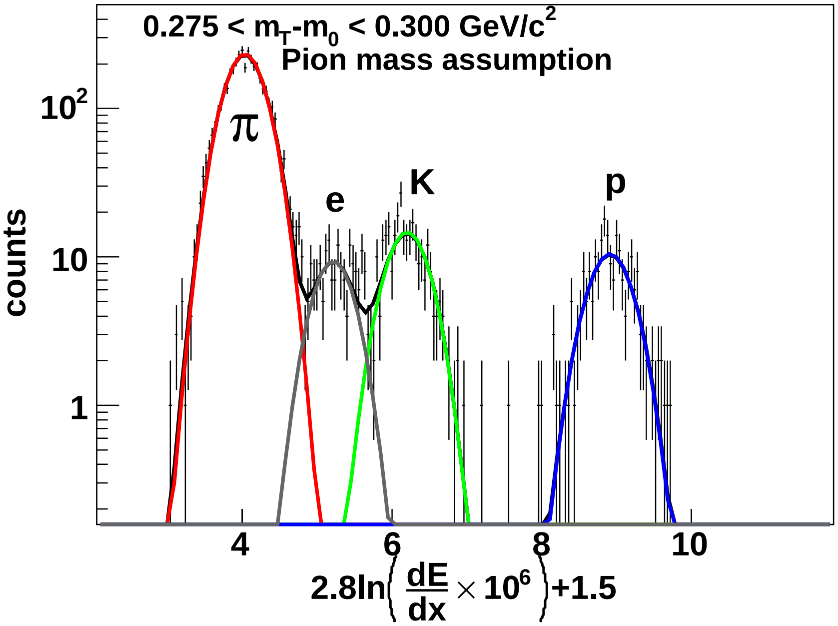

Figure 4.7. Energy loss distributions of positively charged particles at midrapidity ($|y| < 0.1$, using pion mass assumption) within $0.275 < m_T - m_0 < 0.300$ GeV/c^2.

parameters, the fits would be unreliable. Certainly, there are $m_T - m_0$ regions where the overlaps are too great for the fit to succeed. In such $m_T - m_0$ slices the particle yield extractions were omitted, which result in gaps in the final spectra, as will be seen later.

The Gaussian fits which were used to extract the π^+, K^+, and p yields in different $m_T - m_0$ regions are shown in Figures 4.8, 4.9, and 4.10, respectively. The regions shown in these figures are the highest $m_T - m_0$ ranges where we could do PID for respective particles.

The movement of each of the Gaussian curves from bin to bin are directly related to the shape of the dE/dx vs $\beta\gamma$ fit function (as seen in Figure 4.5).

These fits would later be integrated over to obtain the yields of the particles. Note that for any given mass hypothesis, only the yield of the particle with that mass is extracted, so that the yield is in a correct rapidity bin. The other three Gaussian fits were used to calculate contaminations (overlapped areas) only.

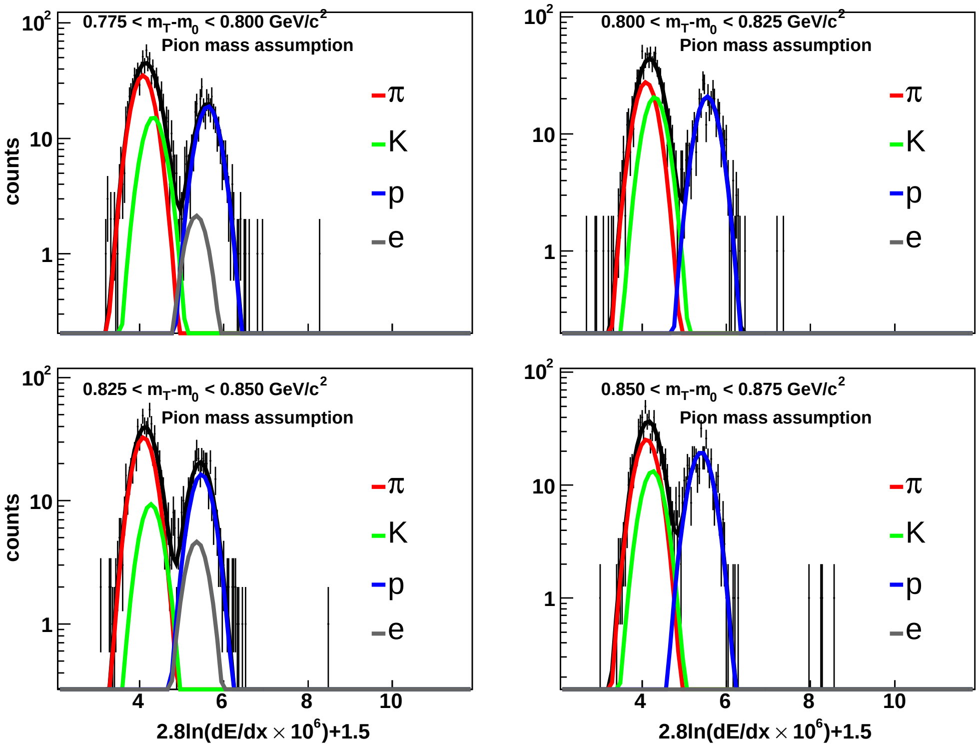

Figure 4.8. Midrapidity dE/dx distributions of positively charged particles. The four panels represent different transverse mass regions. Overall, they cover $0.775 < m_T - m_0 < 0.875$ in GeV/c^2. To extract the pion yield, pion rest mass is assumed.

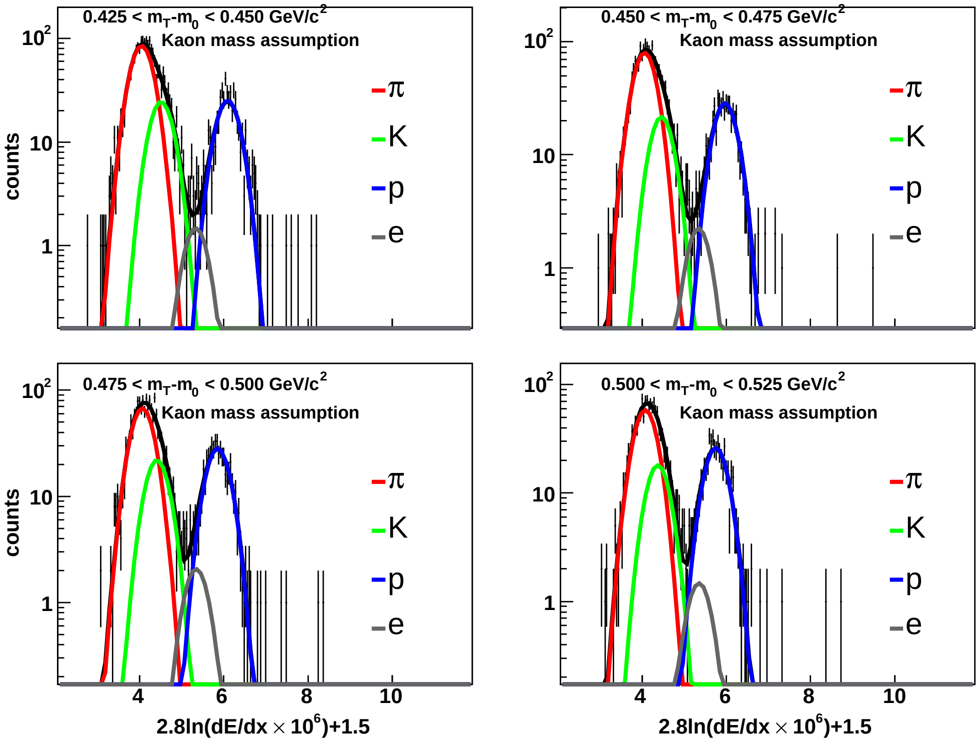

Figure 4.9. Midrapidity dE/dx distributions of positively charged particles. The four panels represent different transverse mass regions. Overall, they cover $0.425 < m_T - m_0 < 0.525$ in GeV/c^2. To extract the kaon yield, kaon rest mass is assumed.

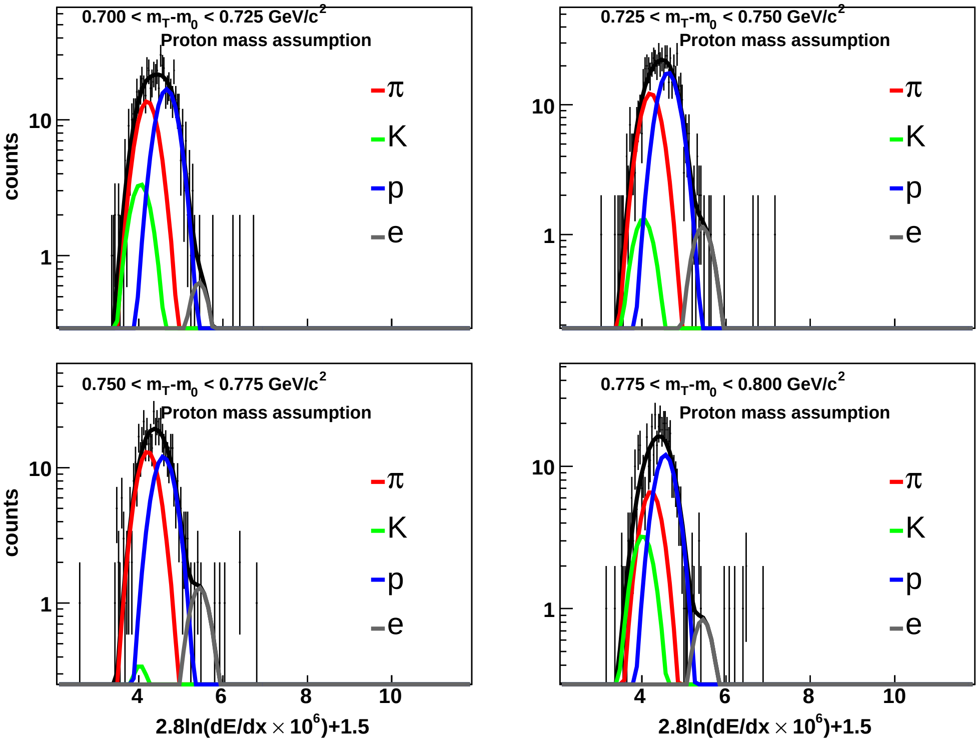

Figure 4.10. Midrapidity dE/dx distributions of positively charged particles. The four panels represent different transverse mass regions. Overall, they cover $0.700 < m_T - m_0 < 0.800$ in GeV/c^2. To extract a midrapidity proton yield, the proton rest mass is assumed.

Figure 4.11 shows an example of the dE/dx distributions and fits in all 40 transverse mass bins. The data shown are positive particles within $|y| < 0.1$, using the pion mass, from top 10% central events.

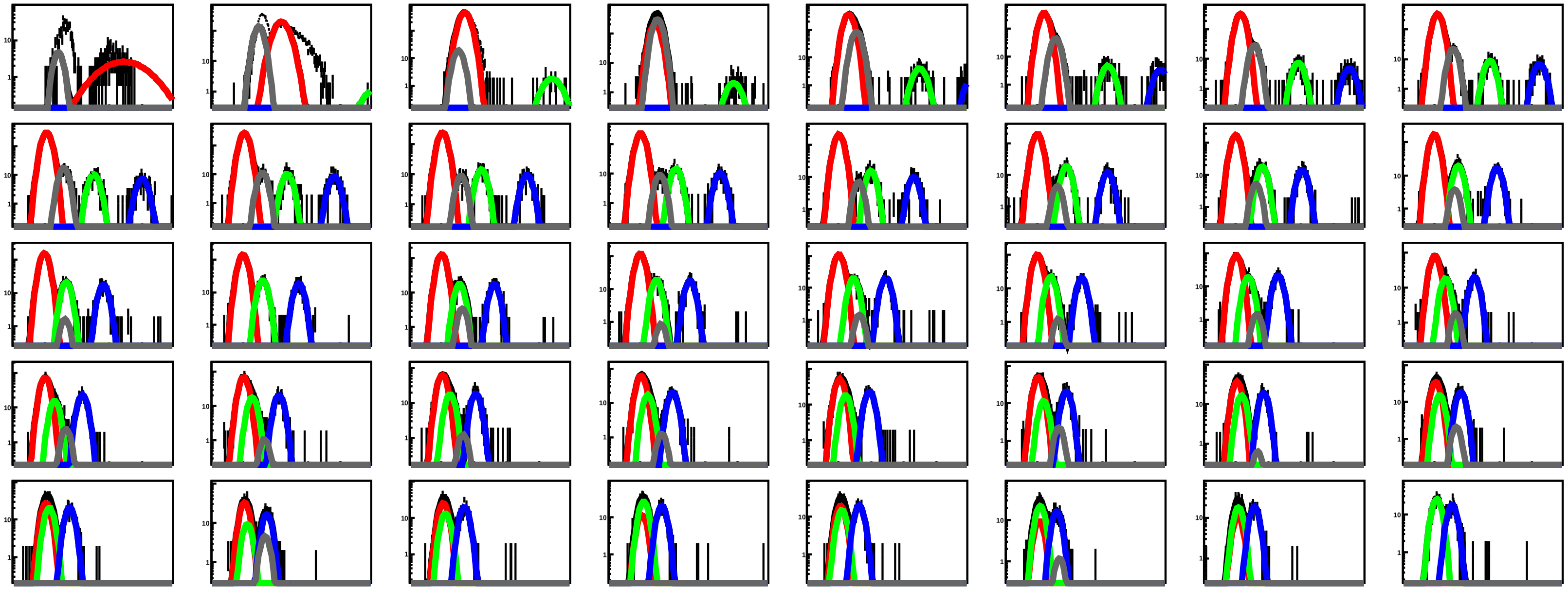

Figure 4.11. Energy loss distributions in different transverse mass bins. From left to right and top to bottom, $m_T - m_0$ goes from 0 to 1 GeV/c^2. In this present case, the positive particles from top 10% central collisions are shown. With a pion mass assumption, a rapidity cut of $-0.1 < y < 0.1$ was applied. The horizontal axis is $2.8 \ln(dE/dx) + 1.5$ going from 2.1 to 11.9 GeV/c^2. The vertical axis is dN/dm_T. Only $m_T - m_0$ slices 5-35 are used in the final spectra. (Figure legends: red is positive pions, green is positive kaons, blue is protons, and gray is positrons.)

Figure 4.11 represents one case of (particle[2], y, centrality). The total number of cases we analyzed is

$$(\text{6 particles}) \times (\text{5 rapidity bins}) \times (\left\{ \begin{array}{c} 5\ (\pi) \\ 4\ (K) \\ 3\ (p) \end{array} \right\} \text{ centrality bins}) = 360. \qquad (4.6)$$

---

[2] or mass assumption

Chapter 5

Yield Corrections

After the raw yields of the particles have been extracted, they were then passed through correction procedures. The main purpose is to construct the picture of what the collisions really produced, as opposed to what the detector saw. This chapter addresses the issues of tracking efficiencies and secondary proton generation. [1]

5.1 Efficiency

The tracking efficiency is affected by several factors, such as the finite acceptance of the detector, the electronics detection efficiency, the two-hit resolution, and particle decays. The efficiency correction was done by the GSTAR framework (the STAR detector simulation using GEANT).

Simulated particle tracks with predefined momenta and rapidities are software-generated and embedded inside a real event. This mixing of real and fake data creates an environment (called a Monte Carlo event) similar to the real events, where very high density of tracks are present inside the TPC. The number of embedded tracks is kept low relative to the number of real tracks to avoid distorting the track density of the event. Reconstruction software then reads the simulated event and outputs

---

[1] The energy loss effects were investigated in Appendix D and found to be negligible.

the information regarding this event. The p_T distribution of the simulated particle tracks that get reconstructed is then compared with the original embedded tracks. We then take the ratio of these two distributions as a function of p_T; a perfectly efficient detector would have the ratio equal to 1.

The distributions of embedded and reconstructed negative pions and the ratio between the two are shown in Figure 5.1. The ratio is fitted with equation (5.1) [140] to obtain the efficiency curve as a function of p_T:

$$\text{efficiency} = a e^{-(b/p_T)^c} \tag{5.1}$$

where a, b, and c are fit parameters.

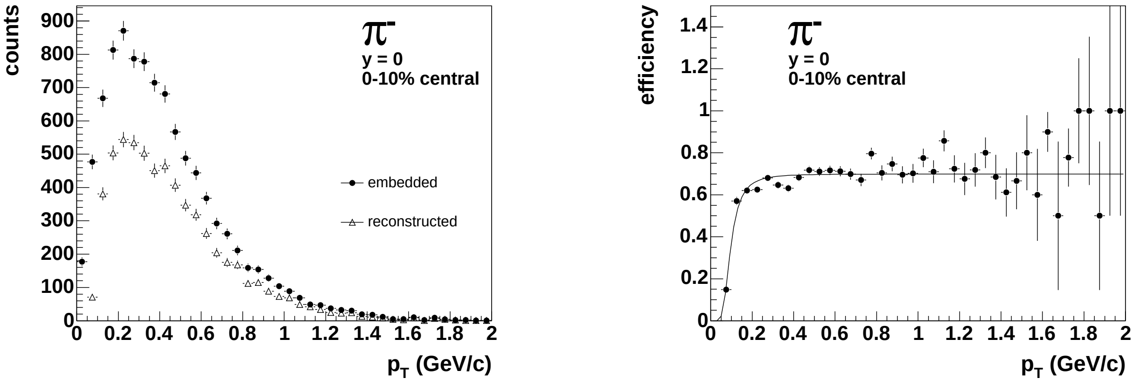

Figure 5.1. Left panel shows the p_T distributions of embedded and reconstructed negative pions. Right panel shows the corresponding ratio of the two distributions and the pion efficiency curve as a function of p_T. Simulation using cuts for top 10% events are shown.

The efficiency depends on particle's mass, centrality, and transverse momentum. Particles with shorter lifetimes will be harder to detect. Centrality-wise, more particles are produced as the collisions become more central, thus increasing the density of tracks inside the TPC. This lowers the tracking efficiency.

The efficiency drops sharply below $p_T \approx 0.3$ GeV/c due to the acceptance (low-momentum particles curl up inside the TPC magnetic field). The slower particles also have shorter lives than the faster ones due to the relativistic effects. At higher transverse momentum, the efficiency rises due to smaller track density.

The efficiency also depends on the cuts applied. For example, reducing the number of fit points required would increase the efficiency. The embedding study was done for three negative particle species: π^-, K^-, and $\bar{p}$. We applied the same efficiency correction for π^- and π^+; same scenario with K^- and K^+. The systematic error for the efficiency is estimated to be 8%.

Protons exist naturally everywhere. Due to this fact, the probability of the antiprotons being annihilated is relatively high compared to other produced particles. The $\bar{p}$ efficiencies were determined by taking the $\bar{p}$ absorption by the detector materials into account. The proton-antiproton annihilation cross sections are different for different materials. Figure 5.2 shows the absorption factor as a function of $m_T - m_0$. The absorption is most probable for slow antiprotons. Data used here are from a STAR simulation study [141]. Equation (5.2) is used to fit the absorption factor.

$$\text{absorption} = a(b - e^{-c(m_T - m_0)}) \tag{5.2}$$

where a, b, and c are the fit parameters.

The proton efficiency is obtained by correcting the $\bar{p}$ efficiency by this absorption factor, $\text{eff.}_p = \text{eff.}_{\bar{p}} \times 1/\text{absorp.}$.

The efficiencies for pions outside the low $m_T - m_0$ region (where the corrections are biggest) are 70% for the most central and 80% for the very peripheral (50-70% centrality) events. The corresponding efficiencies for kaons are 60% and 70%, respectively. For antiprotons and protons, the efficiencies are 75% and 82%, respectively. For pions, protons, and antiprotons, the efficiency flattens out above 0.2 GeV/c^2. For kaons, the efficiency reaches the plateau most slowly due to the fact that kaons are the fastest species to decay.

The efficiency curves for all the cases are shown in Figure 5.3. By inspection, the

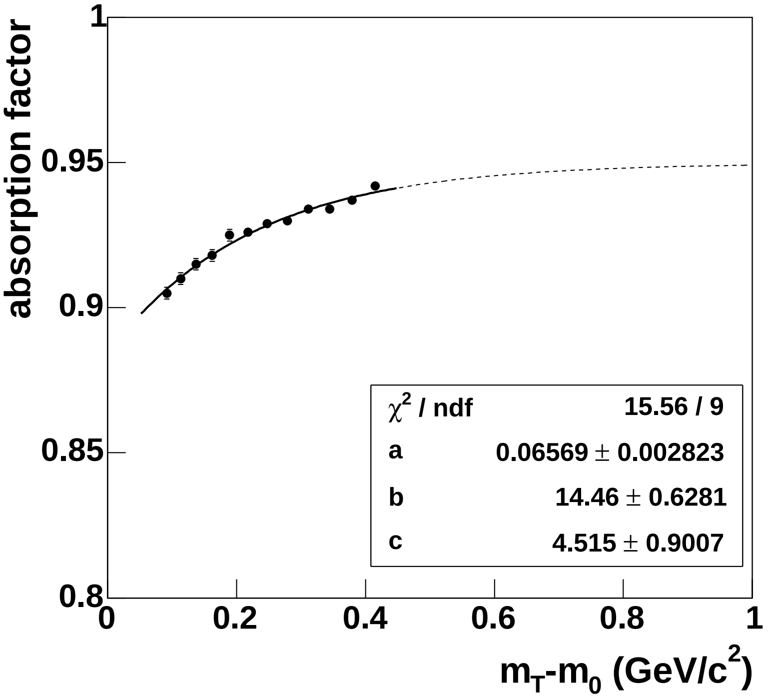

Figure 5.2. Antiproton absorption correction as a function of $m_T - m_0$.

relative systematic error for the efficiency correction is estimated to be 8%.

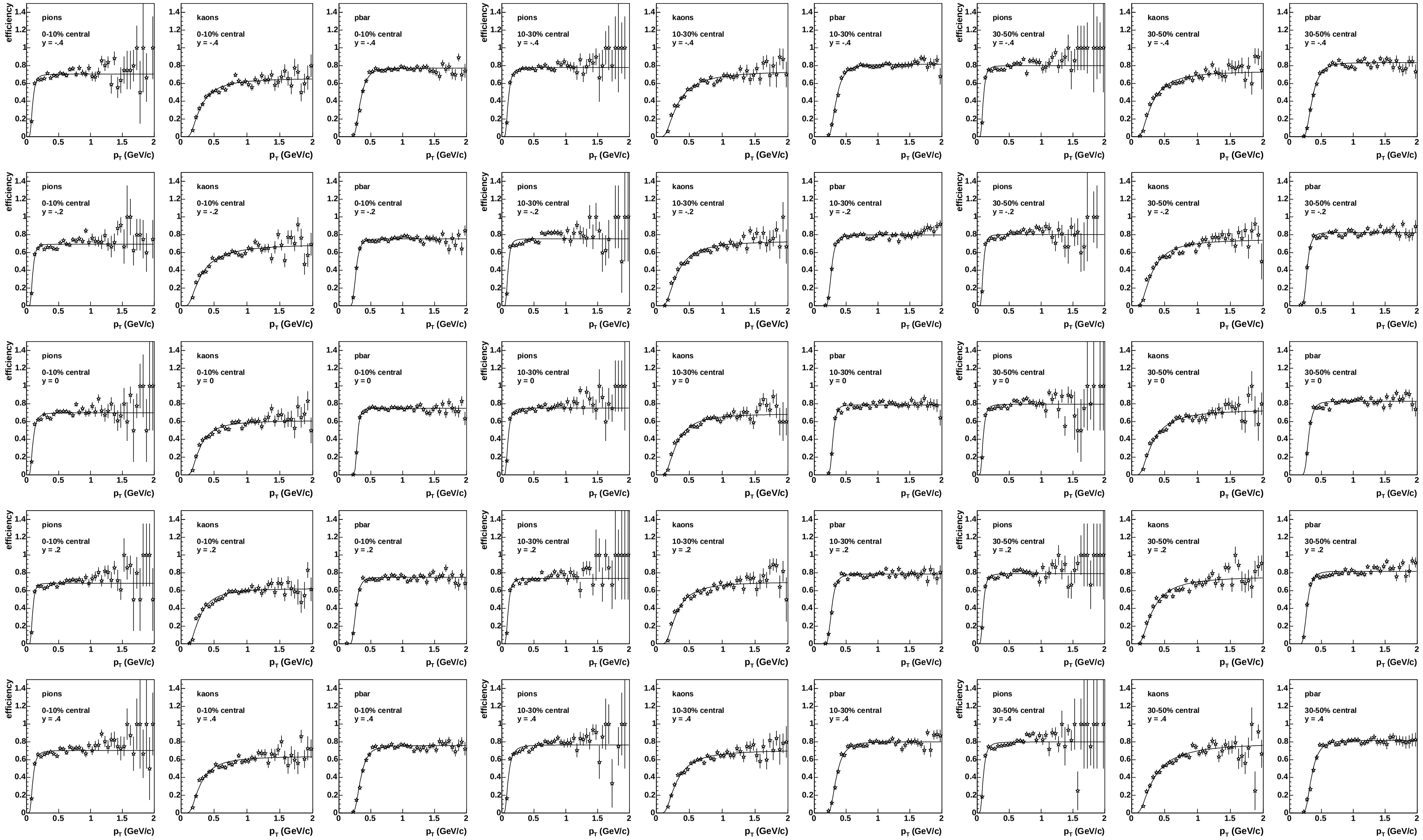

Figure 5.3. Efficiency for π^-, K^-, and $\bar{p}$ for different centrality and rapidity bins. Different rapidity bins are arranged in rows. The solid curves are fits to the data with equation (5.1).

5.2 Proton Background

Not all of the detected protons come from the collisions of the gold ions. There are secondary protons which come from the interactions of fast particles–mostly pions– with the detector material. Particles which are produced directly from the collisions will originate near the primary vertices. These primary particles will have small distance of closest approach (DCA), in contrast to those from subsequent interactions.

The secondary protons are produced far from the initial nucleus-nucleus collisions and therefore they can be subtracted from the total proton yields using the DCA distribution approach [141, 142]. We only have to worry about the protons here because these background protons are not created from the collisions, but knocked off from the surrounding nuclei. The nuclear binding energy is low compared to the threshold to create, for example, a pion. This is the reason for not expecting similar backgrounds of pions. The binding energy per nucleon, is defined [143] as

$$\frac{B}{A} = \frac{Z m_{^1H} + N m_n - m_{^AX}}{A} \tag{5.3}$$

where B is the binding energy, A is the nuclear mass number, Z and N are the number of protons and neutrons, respectively, m_H and m_n are masses of a hydrogen atom and a neutron, respectively, and $m_{^AX}$ is the atomic mass of ^AX. For the gold nucleus, the binding energy is ≈ 8 MeV/nucleon.

The number of the background protons depends strongly on how much material is inside the detector. Therefore, the effect varies for the experiment from year to year. The knocked-off protons usually have low momentum as compared to the those from the collisions. Thus, the background is expected to decrease with $m_T - m_0$. To correct for the background protons, we calculate the fraction of (background protons)/(total protons) within DCA < 3 cm.

To construct the DCA histograms, we first selected particles that pass all the initial cuts described in Chapter 3. After that, additional dE/dx cuts were imposed to select just protons and antiprotons. Values of Gaussian centroids and widths from the the dE/dx fitting (Chapter 4) were used to accomplish this task. From the data, dE/dx of protons and antiprotons are well separated from other species in the $m_T - m_0$ range of 50 to 250 MeV/c^2.

Each DCA histogram is fitted from 4 to 8 cm with equation (5.4)

$$\text{background} = a(1 - e^{-x/b}) \tag{5.4}$$

where x is the DCA; a and b are fit parameters.

The DCA distributions along with the fits with fixed $b = 1.0$ are shown in Figure 5.4. We can see that protons have a long tail of non-zero DCA background which antiprotons do not have. By varying the value of b parameter in the fit function, the systematic error of the background can be estimated. This error came out to be 50% relative to the background.

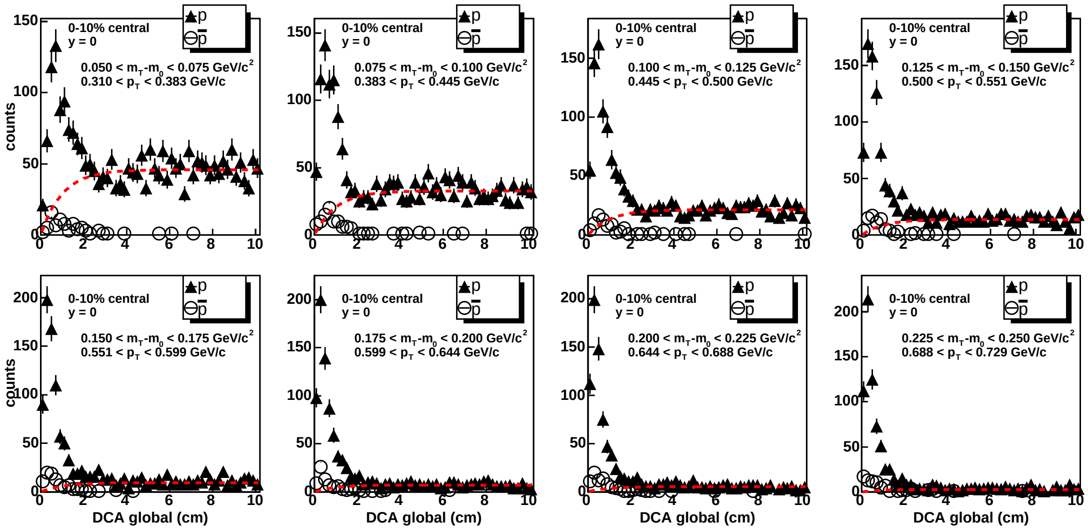

Figure 5.4. DCA distributions of protons and antiprotons in eight different $m_T - m_0$ slices. $-0.1 < y < 0.1$, top 10% central events. The dashed lines are fits using equation (5.4) with p_1 parameter fixed to 1.0.

The background proton yield is calculated by extrapolating the function to DCA = 0 cm and then integrating it from 0 to 3 cm. The correction is then applied to the data,

$$\text{corrected yield} = \text{uncorrected yield} \times \left(1 - \frac{\text{background}}{\text{total}}\right) \tag{5.5}$$

The resulting ratio of background/total protons as a function of $m_T - m_0$ is shown in Figure 5.5 for the midrapidity protons from top 10% central events. As we can see, the background decreases rapidly and becomes negligible for $m_T - m_0 > 0.4$ GeV/c^2. Quantitatively, for 0-10% central events, $-0.1 < y < 0.1$, the background relative to the total protons goes from about 35% at $m_T - m_0$ of 0.0625 GeV/c^2 to less than 5% at 0.2375 GeV/c^2.

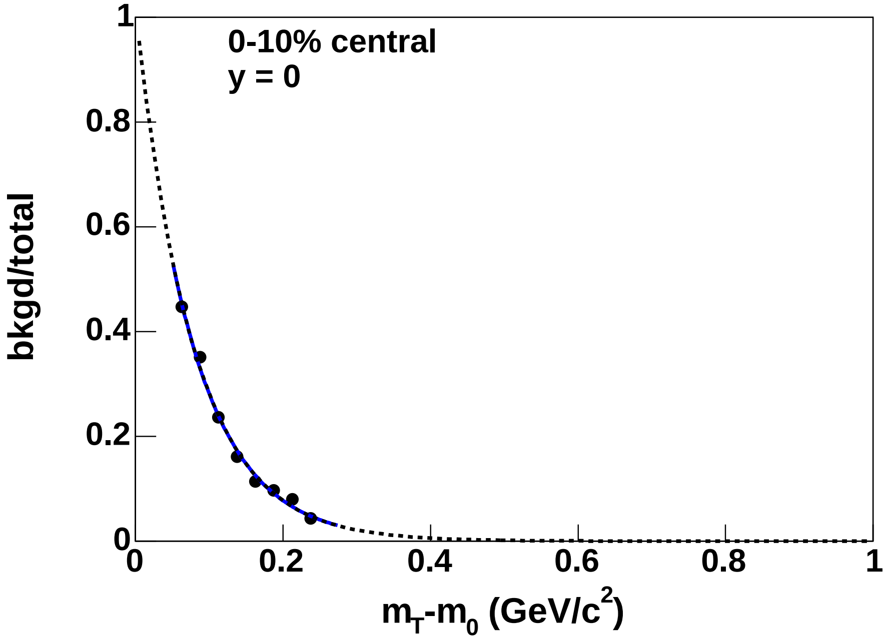

Figure 5.5. The ratio of background protons over total protons as a function of $m_T - m_0$. $-0.1 < y < 0.1$, top 10% central events.

Chapter 6

Results

In previous chapters, the instrumentation and the analysis methods have been presented. The results from the spectra analysis from Au+Au collisions at a center-of-mass energy of $\sqrt{s_{\mathrm{NN}}} = 19.6$ GeV will be discussed in this chapter.

6.1 Transverse Mass Spectra

Figure 6.1 shows the extracted transverse mass distributions of π^+, π^-, K^+, K^-, p, and $\bar{p}$ at midrapidity ($|y| < 0.1$). For each particle species, the yields from different centrality classes are shown. The quantity on the vertical axis is the invariant yield per event. Physically, it is the number of particles (averaged per event) in a phase space region defined by the four-momentum: $\frac{dp_x\,dp_y\,dp_z}{E}$. The term "invariant yield" comes from the fact that the phase space element is invariant under a Lorentz transformation ($E' = \gamma E - \gamma\beta p_z$, $p'_z = \gamma p_z - \gamma\beta E$).

An azimuthally symmetric distribution of the particles averaged over all events is assumed; therefore an integration over ϕ is applied.

$$\frac{1}{N_{\mathrm{events}}}\left(\frac{d^3N}{dp_x\,dp_y\,dpz/E}\right) = \frac{1}{N_{\mathrm{events}}}\left(\frac{d^3N}{m_T\,dm_T\,dy\,d\phi}\right) \tag{6.1}$$

$$= \frac{1}{N_{\mathrm{events}}}\left(\frac{d^2N}{2\pi m_T\,dm_T\,dy}\right) \tag{6.2}$$

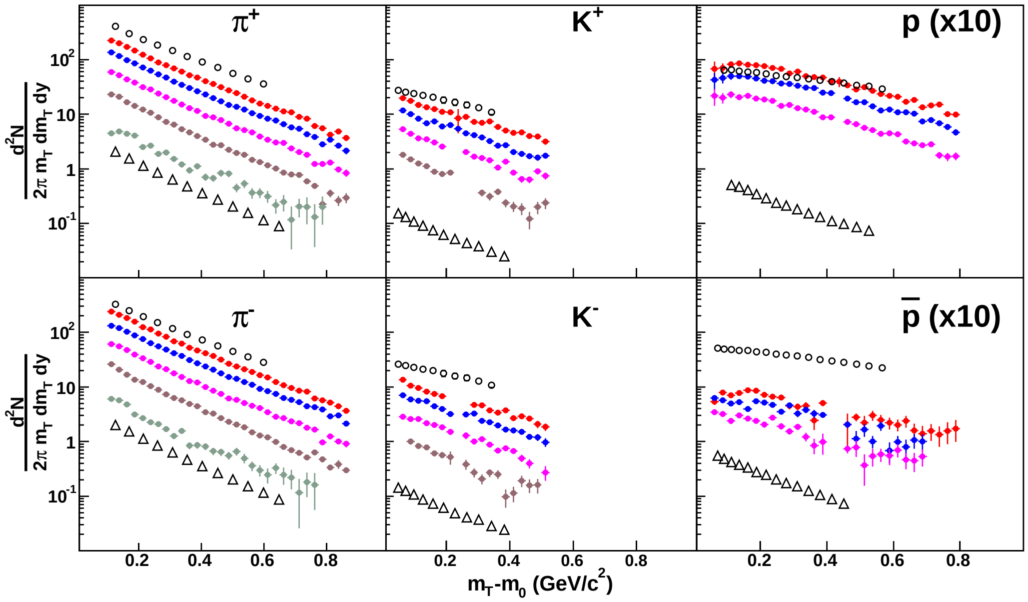

Figure 6.1. Transverse mass spectra of identified hadrons measured at midrapidity ($|y| < 0.1$). The results at $\sqrt{s_{\rm NN}} = 19.6$ GeV for different centrality bins are shown as solid symbols. From top to bottom, the filled circles correspond to 0-10%, 10-30%, 30-50%, 50-70%, 70-100% most central. Note that there are no spectra results from some of the most peripheral bins for kaons, protons, and antiprotons. The open symbols represent two sets of STAR 200 GeV results: Au+Au at 5% most central (circles) and minimum bias p+p (triangles). p and $\bar{p}$ are scaled up by a factor of 10. All the panels use the same scales on the axes.

On the horizontal axis, m_0 refers to the rest mass of each corresponding particle species; for charged pions, the rest mass is 139.570 MeV/c, for charged kaons, 493.677 MeV/c, and for protons and antiprotons, 938.272 MeV/c [43]. The spectra shown here in Figure 6.1 are for midrapidity ($-0.1 < y < 0.1$) particles.

The gaps in the spectra are mostly due to the overlapping of dE/dx distributions of the hadrons with the electrons. Additionally, in some $m_T - m_0$ slices, the Gaussian function failed to fit the dE/dx histograms due to low statistics and poor resolution (wide distribution). In such slices, we omitted the extracted yields from the final spectra.

Also in Figure 6.1, the 200 GeV results of top 5% central Au+Au and minimum bias p+p from STAR [18] are shown for scaling reference. From the figure, we observe that five of the six 19.6 GeV transverse mass spectra fall in between the two sets of 200 GeV spectra. The one exception is the protons, where most central events at $\sqrt{s_{\mathrm{NN}}} = 19.6$ GeV yield higher number of low $m_T - m_0$ protons than 200-GeV most central events. This could be explained by a higher degree of stopping (more incoming protons were transported to midrapidity) in low-energy central collisions [144, 145].

The kaon, proton, and antiproton spectra from 200 GeV Au+Au appear "harder" (higher transverse momentum) than those from the 19.6 GeV most central events, whereas the most peripheral events in 19.6 GeV Au+Au created more particles per event than the 200 GeV p+p.

The more central the collision, the larger the overlap region and the higher the number of participating nucleons. Therefore, more energy is available to be converted into new particles. As the centrality increases, the yield per event of the produced particles shows a systematic increase as expected. The shapes (slopes), which can be related to the temperature parameter T in the Boltzmann factor of the thermal energy distribution, are very similar between different centrality bins.

A general thermal distribution ($\sim e^{-E/T}$, where E is energy and T is temperature) works well, as we can see from the exponential shapes of different particle spectra. However, the thermal function does not work well in the very low $m_T - m_0$ due to the collective outward boost from the explosion. At the very high $m_T - m_0$, thermal distributions have also been found inapplicable because fast particles may leave the collision region so fast that they do not have enough time to thermalize with the rest of the system. In such high p_T (hard) regions, a power-law distribution [146] is normally used to fit the spectra.

In this study we examined the very low $m_T - m_0$ regions. When the system of particles is dense, the particles collide often and act as a collective fluid, as opposed to free particles. The collective flow pushes particles to higher p_T regions. Pions and kaons, being lighter and of higher velocity than proton and antiprotons, are not affected as much by the collective flow in the m_T spectra. This collective flow results in the inverse slope rising with the mass of the particle, the effect being largest at low $m_T - m_0$.

To quantitatively study the flow effects from the collisions, we need to take into account the collective flow in our fit functions. In this study we compare our results with two models which take into account the pressure wave from the explosion. The first one is a spherical expansion model, formulated by Siemens and Rasmussen for low energy nuclear collisions at BEVALAC. The second model by Schnedermann, Sollfrank, and Heinz assumes a longitudinal boost-invariant cylindrical expansion for higher energy systems at the SPS. The idea behind both models is that the collective transverse flow in heavy ion collisions boosts particles with different masses differently (in terms of energy) for the same radial flow velocity.

In elementary collisions such as proton on proton, rescattering is absent therefore the spectral slopes have zero collective boost. Thus the extracted temperatures for particles of different species are the same [147]. In a heavy ion collision, since there is a very high density of particles produced, the subsequent scattering and expansion introduce a blast velocity. This hydro-like velocity combined with the freeze-out (local) temperature parameter is used to describe the shape of the transverse mass spectra. In Section 6.7 we will go into the two models in more details and extract the flow velocities and the freeze-out temperatures.

The particle spectra from the most central events are compared with SPS results at 17.3 GeV from three experiments (NA44 [11, 148], NA49 [13, 149], and WA98 [10]) in Figure 6.2. As a note, the NA44 data are not exactly at midrapidity. $\pi^{\pm}$ were measured in $0.2 < y < 1.2$. This explains the dropping of their high $m_T - m_0$

pion yields, as compared to our data. $K^{\pm}$ are from $-0.5 < y < 0.6$. p and $\bar{p}$ are from $-0.6 < y < 0.0$. Results from the other experiments are from midrapidity. The shapes of π^- spectra are consistent for STAR, NA49, and WA98. The K^+ and K^- spectra agree exceptionally well across experiments. There is a slight shape difference between our and NA44 p and $\bar{p}$ spectra at low $m_T - m_0$.

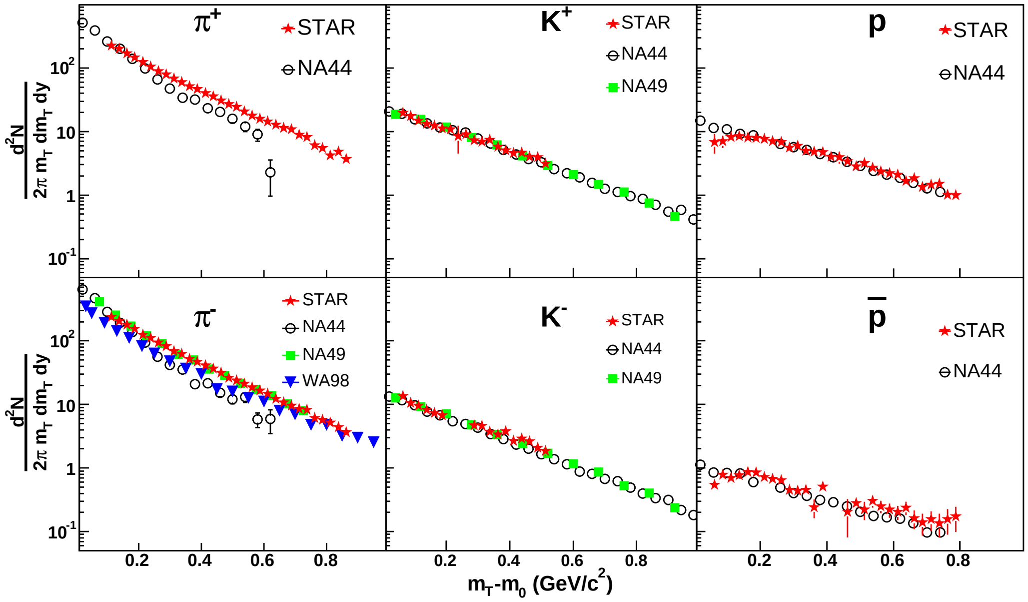

Figure 6.2. Transverse mass spectra comparisons between the most central collisions from STAR 19.6 GeV with SPS NA44, NA49, and WA98. Solid stars represent top 10% events of STAR 19.6 GeV, solid squares NA49 top 5% (except p and $\bar{p}$ are top 10%), open circles NA44 top 10%, and solid triangles WA98 top 10% (all SPS results are from $\sqrt{s_{\mathrm{NN}}} = 17.3$ GeV run). The high-p_T parts of the WA98 π^-, NA44 K^+, and NA44 K^- spectra can be found in [10, 11].

Different functions are used to fit the spectra. Among those are three statistical functions which describe the distribution of particles in thermal equilibrium. Maxwell-Boltzmann function describes identical but distinguishable particles (such as molecules). Bose-Einstein function describes indistinguishable integral spin (0, 1, 2, ...) particles (bosons), and Fermi-Dirac function describes indistinguishable half-integral spin (1/2, 3/2, 5/2, ...) particles (fermions). The quantum distributions approach the classical Maxwell-Boltzmann description when the energies of the particles are much greater than the temperature of the system, which is true in part of this study.

The particle spectra appear to be exponential. All six spectra are fitted to the Maxwell-Boltzmann function, and two "blast wave" models. In addition, pions and kaons are fitted to the Bose-Einstein function, whereas for protons and antiprotons, the Fermi-Dirac function is used. The thermal statistical distributions are defined below, whereas the two models with radial flow description will be discussed in Section 6.7.

$$\begin{aligned} f_{\mathrm{Maxwell-Boltzmann}} &= \frac{A}{\exp(E/T)} & (6.3) \\ f_{\mathrm{Bose-Einstein}} &= \frac{A}{\exp(E/T) - 1} & (6.4) \\ f_{\mathrm{Fermi-Dirac}} &= \frac{A}{\exp(E/T) + 1} & (6.5) \end{aligned}$$

where f is the probability of finding a particle with energy E, A is the normalization constant, and T is the temperature of the equilibrated non-flowing system.

The centrality dependence of particle production is plotted as a function of p_T in Figure 6.3. The ratio is scaled by the numbers of participants for the given centrality bins. There seems to be slight yield enhancement for higher p_T particles. This behavior is a sign that central collisions generate strong transverse expansions.

The midrapidity spectra with Maxwell-Boltzmann fits (equation (6.3)) are shown in Figure 6.4.

Table C.10 shows that the inverse slope goes up with particle mass.

The extracted transverse momentum spectra for four other rapidity bins are shown in Figures 6.5, 6.6, 6.7, and 6.8. The spectra are shown with the Maxwell-Boltzmann

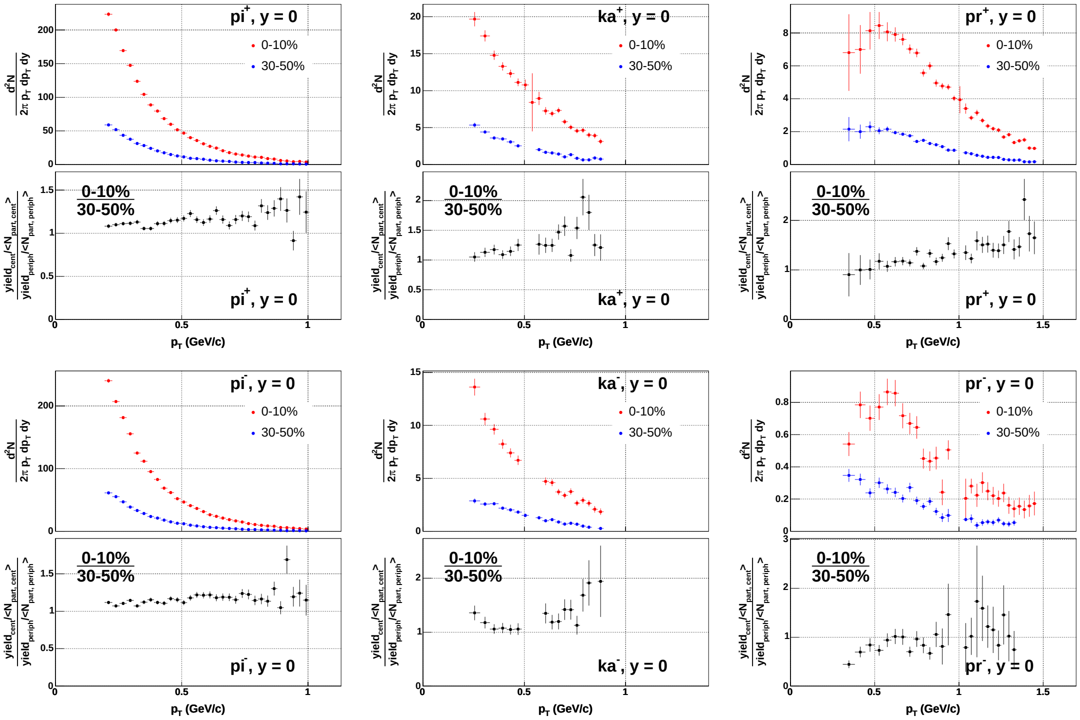

Figure 6.3. The ratio of midrapidity ($|y| < 0.1$) particle yields (scaled by $\langle N_{\text{part}}\rangle$) between 0-10% and 30-50% centrality classes. The figures are arranged in pairs. The upper panel of each pair shows two p_T spectra; the lower panel is the ratio between the two spectra. There are six pairs in total, one for each hadron.

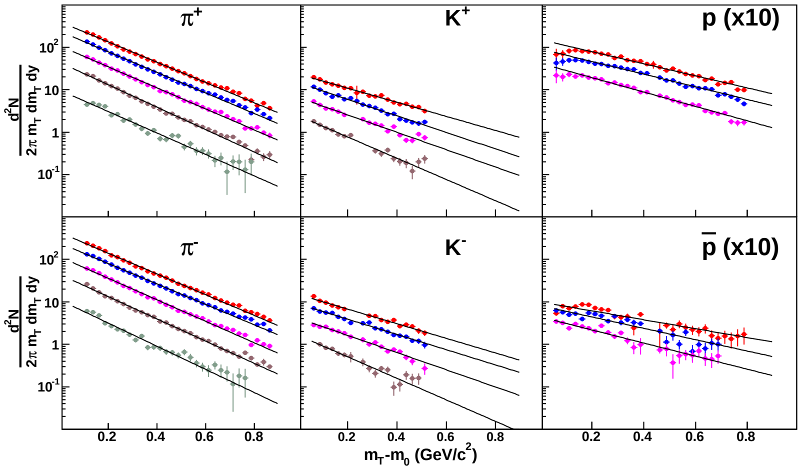

Figure 6.4. Transverse mass spectra of $\pi^{\pm}$, $K^{\pm}$, p, and $\bar{p}$, within rapidity $-0.1 < y < 0.1$, for different centrality bins. p and $\bar{p}$ are scaled up by a factor of 10. The solid lines are Maxwell-Boltzmann fits.

thermal fits.

6.2 Rapidity Density

The invariant yield integrated over the two components of the transverse plane (azimuthal angle ϕ and p_T) gives us the rapidity density (dN/dy). Under a Lorentz boost to a frame with a longitudinal velocity β_{f}, $y' = y - \tanh^{-1}\beta_{\text{f}}$ and $dy' = dy$. Therefore, dN/dy is a relativistically invariant quantity.

While the transverse mass spectra give us a picture of the transverse dynamics, dN/dy provides a longitudinal picture of the collisions. Figure 6.9 shows dN/dy of the identified particles as functions of rapidity, for different centralities. Note that with 9.8 GeV of energy per beam nucleon, the beam rapidity is $\approx \pm 3$ [1]. The dN/dy values for $-0.1 < y < 0.1$ are listed in Table C.11. Different dN/dy values from

---

[1] For $\sqrt{s_{\text{NN}}} = 200$ GeV, $y_{\text{beam}} = 5.4$.

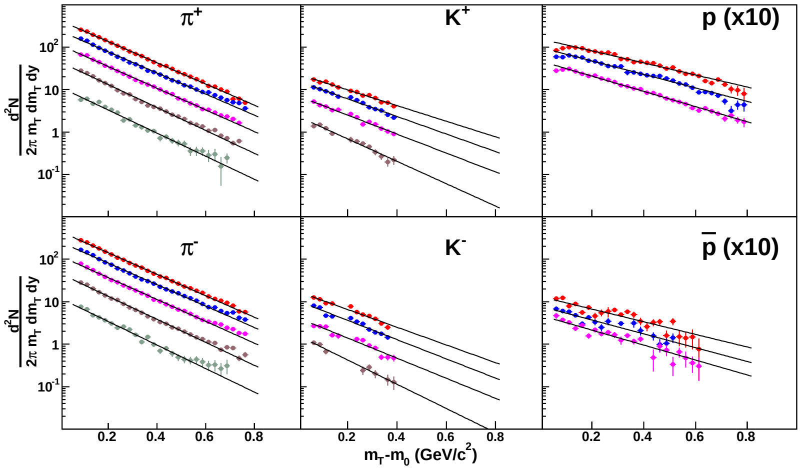

Figure 6.5. Transverse mass spectra of $\pi^{\pm}$, $K^{\pm}$, p, and $\bar{p}$, within rapidity $-0.5 < y < -0.3$, for different centrality bins. p and $\bar{p}$ are scaled up by a factor of 10. The solid lines are Maxwell-Boltzmann fits.

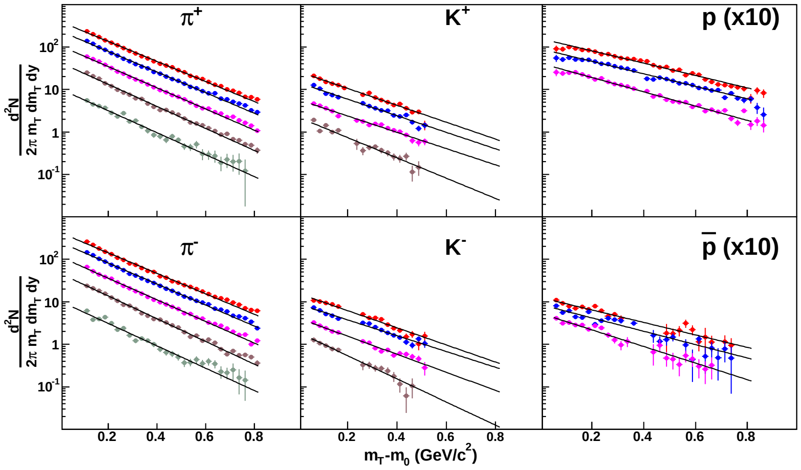

Figure 6.6. Transverse mass spectra of $\pi^{\pm}$, $K^{\pm}$, p, and $\bar{p}$, within rapidity $-0.3 < y < -0.1$, for different centrality bins. p and $\bar{p}$ are scaled up by a factor of 10. The solid lines are Maxwell-Boltzmann fits.

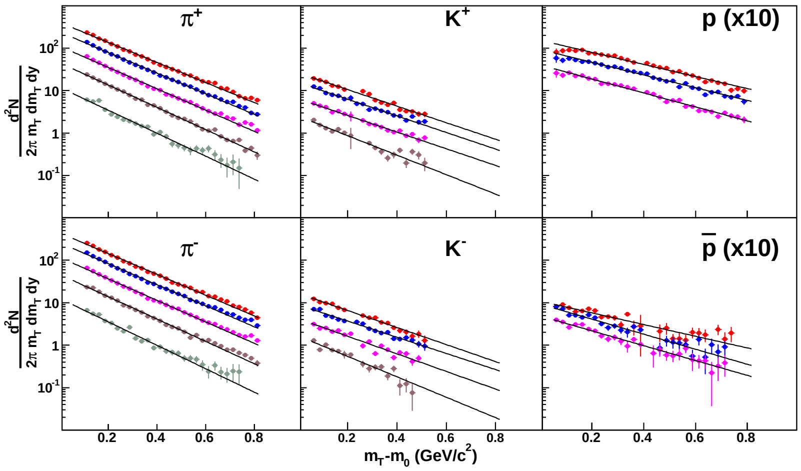

Figure 6.7. Transverse mass spectra of $\pi^{\pm}$, $K^{\pm}$, p, and $\bar{p}$, within rapidity $0.1 < y < 0.3$, for different centrality bins. p and $\bar{p}$ are scaled up by a factor of 10. The solid lines are Maxwell-Boltzmann fits.

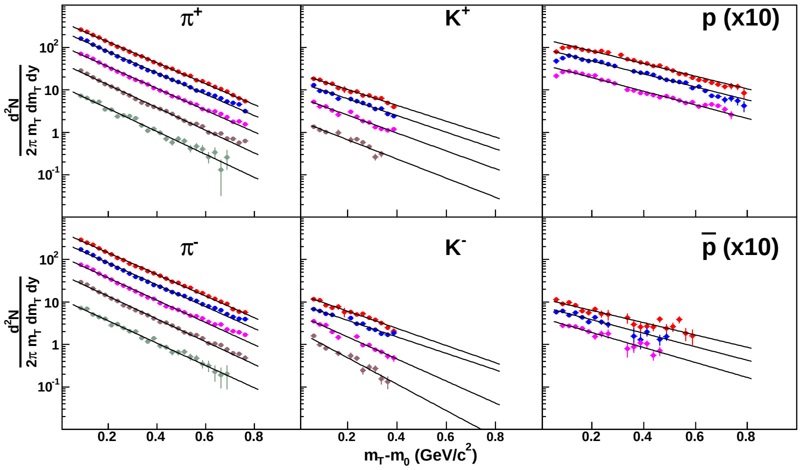

Figure 6.8. Transverse mass spectra of $\pi^{\pm}$, $K^{\pm}$, p, and $\bar{p}$, within rapidity $0.3 < y < 0.5$, for different centrality bins. p and $\bar{p}$ are scaled up by a factor of 10. The solid lines are Maxwell-Boltzmann fits.

different fit functions have been averaged to give the final values. For n functions,

$$\left(\frac{dN}{dy}\right)_{\rm avg} = \frac{\sum_{i=1}^{n}(dN/dy)_i}{n} \tag{6.6}$$

with an uncertainty,

$$\sigma_{dN/dy} = \sqrt{\frac{\sum_{i=1}^{n}\left[(dN/dy)_i - (dN/dy)_{\rm avg}\right]^2}{n}} \tag{6.7}$$

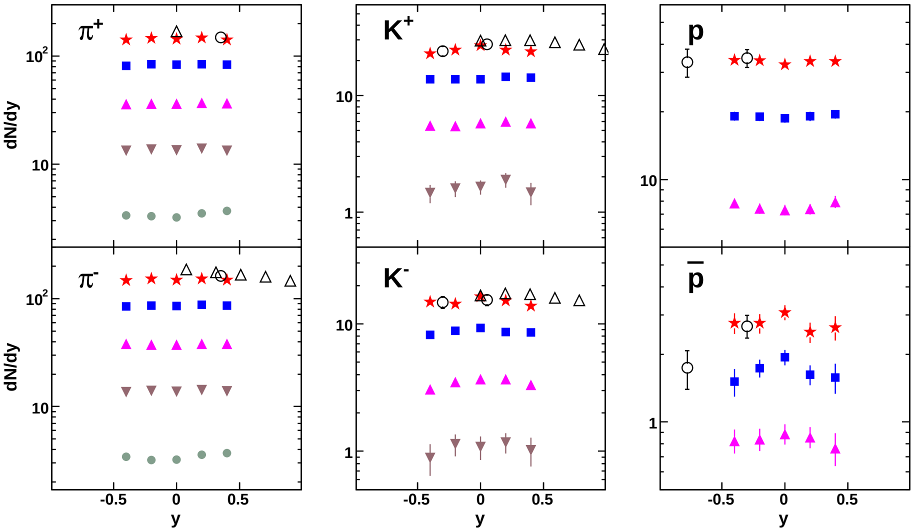

Figure 6.9. Rapidity density distributions of identified hadrons. Our 19.6 GeV results are shown as solid symbols. These distributions (from top to bottom) are for 0-10%, 10-30%, 30-50%, 50-70%, and 70-100% central events. Note that there are no results from some of the most peripheral bins for kaons, protons, and antiprotons. The open symbols represent NA44 top 10% central (circles) and NA49 top 5% central (triangles) results from $\sqrt{s_{\rm NN}} = 17.3$ GeV Pb+Pb.

The SPS results from NA44 and NA49 experiments are shown for comparisons in the plots. Note that the NA49 results [13, 149] are from the top 5% central events, while the NA44 results [11] are from top 10% central events. The more detailed NA49

dN/dy distributions are reported in [150, 151]. The NA44 proton and antiproton values plotted are those without resonance feed-down corrections. The NA49 pions are corrected for resonance decays. Our particle yields were taken inclusively (without the resonance decay corrections).

In the measured region, the pion dN/dy distributions are uniformly flat versus y in all centrality bins, as are the kaons for non-central events. In central collisions, antiprotons show somewhat of an enhancement at midrapidity. There is a slight enhancement at forward and backward rapidity regions for protons from most central collisions. One possible explanation is the incomplete stopping of the incoming protons. These effects are quite small, however.

Overall, we see plateau structures of dN/dy as functions of rapidity, suggesting a Lorentz boost invariance scenario [152], where the system of produced hadrons is distributed uniformly in rapidity, within approximately $|y| < 0.5$. In general, we see good agreement with the SPS results. Further analysis of dN/dy (for example, extend PID coverage into higher rapidity regions) could help us obtain the full 4π yields and longitudinal flow information. However, such a study is a challenge since the statistics are limited in such forward regions.

6.3 Particle Ratios

Particle ratios can be used to gain insight into bulk properties of the system. Things which can be learned include baryon content, strangeness production, and Coulomb potential of the charged source. A set of different particle ratios can be collectively used to extract the information on the chemical freeze-out conditions.

Since particle ratios give us an idea of the relative composition of different quark flavors, the ratios such as $\bar{p}/p$ and K^-/K^+ could act as inputs to calculations of other additional ratios. This can be done using quark coalescence models [153, 154]. For example, $\frac{\Lambda}{\bar{\Lambda}} = \frac{uds}{\bar{u}\bar{d}\bar{s}} = \frac{\bar{u}s}{u\bar{s}} \cdot \frac{uud}{\bar{u}\bar{u}\bar{d}} = \frac{K^-}{K^+} \cdot \frac{p}{\bar{p}}$.

6.3.1 K^-/K^+ and $\bar{p}/p$ Ratios

At midrapidity, the ratio between antiprotons and protons depend on the production of both species during hadronization and the transport of the incident protons to midrapidity. The ratio between the charged kaons can tell us about the strangeness production.

Figure 6.10 shows K^-/K^+ and $\bar{p}/p$ versus the transverse mass. Both ratios show no distinctive sign of $m_T - m_0$ dependence. In the observed region, both ratios are less than one. For $\bar{p}/p$, this signifies that net baryon density ($\propto$ number of baryons minus antibaryons) in the central rapidity region is not zero. For the charged kaons, since there are no valence s or $\bar{s}$ in the incoming nuclei, there must be an equal number of them produced from pair production. Because, as the $\bar{p}/p$ ratio implies, the resulted system contains more u and d quarks than $\bar{u}$ and $\bar{d}$, it is more likely for $\bar{s}$ to combine with u or d to form K^+ ($u\bar{s}$) or K^0 ($d\bar{s}$) than it is for s to pair with $\bar{u}$ or $\bar{d}$ to form K^- ($\bar{u}s$) or $\bar{K}^0$ ($\bar{u}s$). If there were an equal number of u quarks and antiquarks in the fireball, an equal number of produced K^+ and K^- should be observed.

K^-/K^+ and $\bar{p}/p$ ratios as functions of rapidity are shown in Figure 6.11. The K^-/K^+ ratio is relatively uniform over rapidity range $-0.5 < y < 0.5$ and transverse mass range $0 < m_T - m_0 < 1$ GeV/c^2, and shows no significant dependence on centrality–this is consistent with the measurements at other energies [15, 155, 156, 157].

The $\bar{p}/p$ ratio is lower in central collisions than in peripheral collisions. Although this centrality dependence is small, it is more obvious than that of the kaon ratio. Since a central collision creates a large volume of hot and dense nuclear matter, the centrality dependence of $\bar{p}/p$ might be interpreted as the antiprotons being absorbed inside that large collision region. A higher degree of baryon stopping might also be the

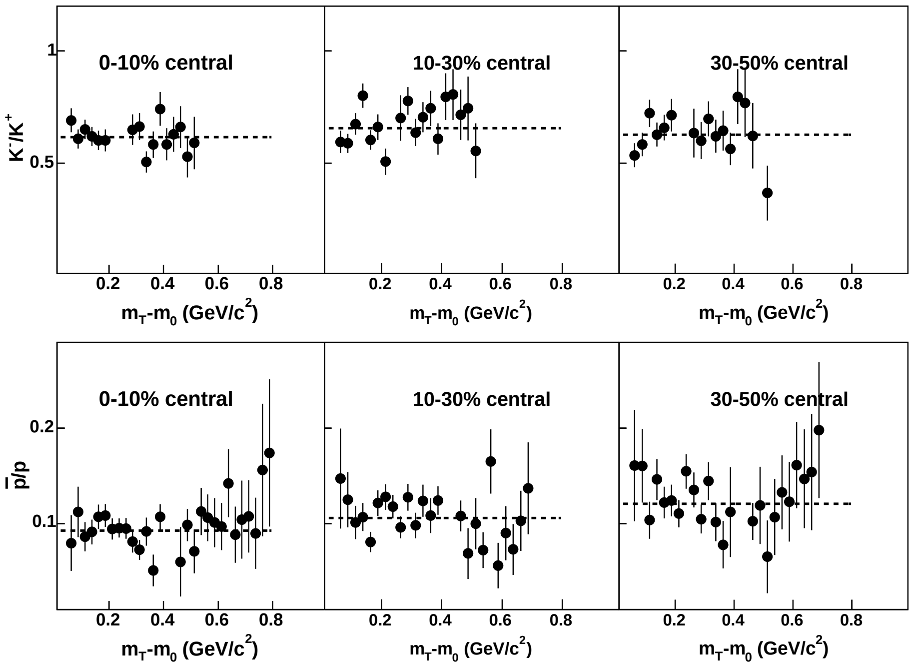

Figure 6.10. K^-/K^+ (top row) and $\bar{p}/p$ ratios (bottom row) vs. $m_T - m_0$, $-0.1 < y < 0.1$, three centrality bins.

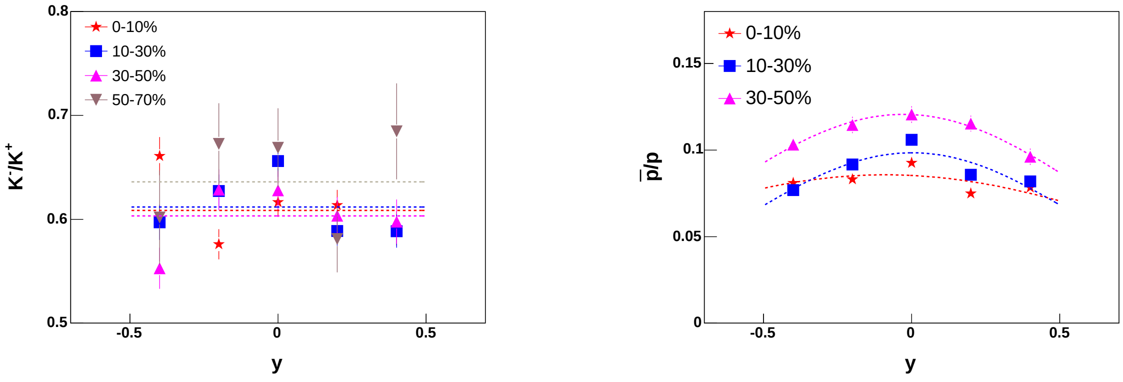

Figure 6.11. K^-/K^+ and $\bar{p}/p$ ratios versus rapidity, for different centrality bins. Kaon ratios are fitted to flat functions, $\bar{p}/p$ to Gaussian functions.

reason of this centrality dependence of $\bar{p}/p$. An enhancement of the ratio is observed at midrapidity. This might be interpreted as the antiprotons being created mostly at midrapidity while the incomplete baryon stopping may contribute to the proton yield at forward rapidity.

We compare the midrapidity K^-/K^+ and $\bar{p}/p$ ratios with other experiments at different beam energies in Figure 6.12. In addition to the SPS results, two low-energy Au+Au experiments at the AGS (E866/E917) are also compared. Ratios measured in p+p collisions at CERN Intersecting Storage Rings (ISR) [158] are also shown as reference. The ratios are from the most central events of each experiment. For the p+p values, K^-/K^+ ratios are integrated over rapidity, while $\bar{p}/p$ results are from midrapidity (Feynman momentum fraction $(x_F) = 0$) and averaged from p_T of 0.35 to 0.60 GeV/c. For the 19.6 GeV values, the ratios are the averages over different rapidity bins within $|y| < 0.5$. The systematic errors were estimated by looking at the deviations from the averaged values.

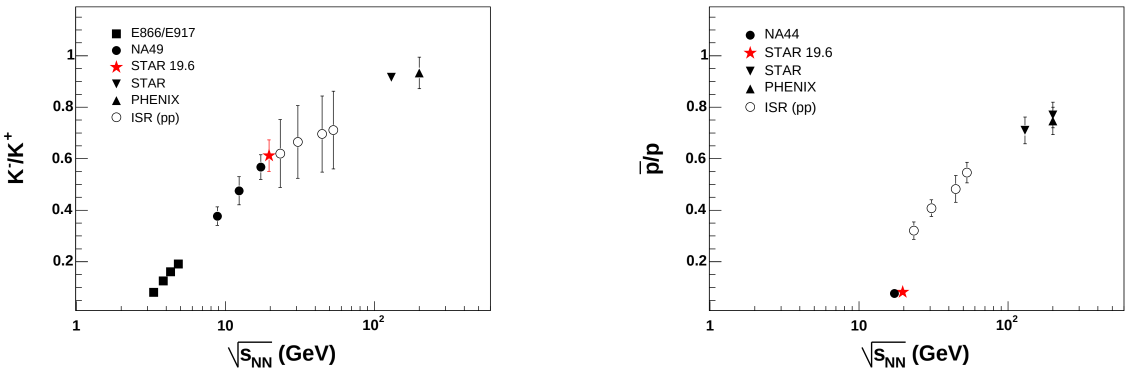

Figure 6.12. K^-/K^+ and $\bar{p}/p$ ratios as a function of $\sqrt{s_{\mathrm{NN}}}$. Results from p+p collisions at the ISR are shown as open symbols. (Data sources: E866/E917 [12], NA49 [13], PHENIX [14], STAR [15, 16, 17, 18].)

As the collision energy increases, both ratios rise systematically. Both ratios are still below unity at RHIC top energy of $\sqrt{s_{\mathrm{NN}}} = 200$ GeV. While the kaon ratios from p+p are consistent with the heavy ion results, the $\bar{p}/p$ ratios seem higher than the heavy ion trend. At higher $\sqrt{s_{\mathrm{NN}}}$ values, protons do not stop significantly.

The rise of K^-/K^+ ratio as a function of energy can be attributed to the nature of kaon production channels. At lower energy the associated production ($N + N \rightarrow N + X + K^+$, where $X = \Lambda$ or Σ) dominates, due to a lower energy threshold. As the energy increases, the pair production which produces the same number of K^+ and K^- becomes more significant.

The formation of a quark-gluon plasma is expected to coincide with an enhancement in production of strange particles [159, 160]. An important difference between the QGP and the hadron gas is the gluon density. There are no available gluons in a hadron gas. In a QGP, a gluon-gluon fusion can create $s\bar{s}$ pairs [160, 161]. The energy threshold for producing an $s\bar{s}$ pair in a QGP is twice the strange quark mass. This threshold is lower than in a hadron gas, where two strange hadrons need to be formed. The time scale of the $gg \rightarrow s\bar{s}$ channel is also predicted to be much shorter than the $q\bar{q} \rightarrow s\bar{s}$ channel [161], resulting in faster production rates. Therefore, an increase in strangeness production should point to a QGP formation.

6.3.2 K/π and $\bar{p}/\pi^-$ Ratios

To further study the strangeness production, we look at the ratios of charged kaons, which carry the bulk of produced strangeness, to pions, the most abundantly produced hadron from the collisions [15, 162]. We first look at the centrality dependence of the kaon to pion ratios (Figure 6.13), in which we see a slight centrality dependence of both ratios. K^+/π^+ ratio reaches the value of 0.17 in central collisions, while K^-/π^- levels out around 0.10. The slow increases of the ratios with respect to centrality are similar to that found in the more elementary collisions of $\bar{p}p$ at $\sqrt{s_{\mathrm{NN}}} = 1.8$ TeV at the Fermilab Tevatron, measured by E735 [163] and in the higher energy system of 200 GeV Au+Au, measured by STAR [18].

The K^+/π^+ and K^-/π^- ratios as functions of collision energy ($\sqrt{s_{\mathrm{NN}}}$) are shown

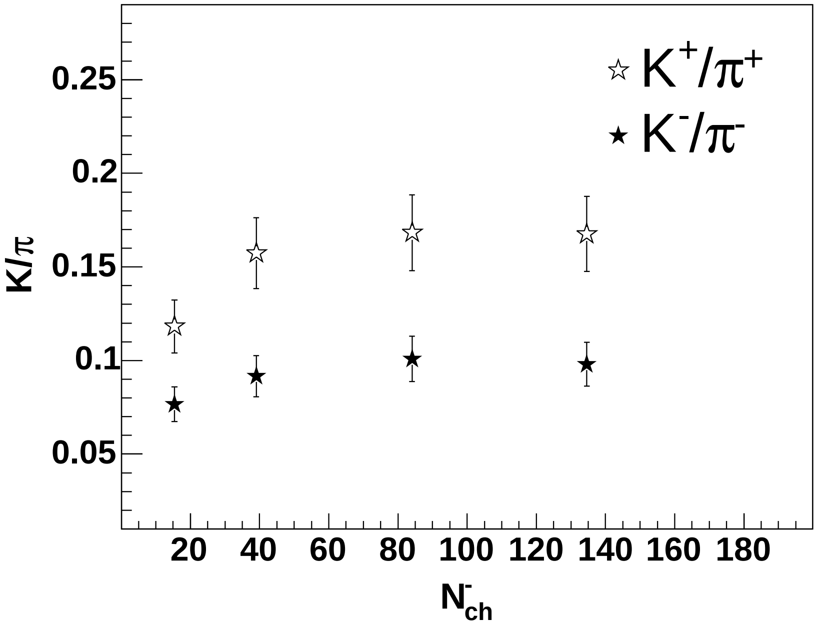

Figure 6.13. Kaon to pion ratios as a function of reference negative multiplicity ($N^-_{\rm ch}$). The K^+/π^+ ratios are shown as open stars, K^-/π^- as filled stars.

in Figure 6.14. The 19.6 GeV values are the averages over a rapidity range of $-0.5 < y < 0.5$ of top 10% central events. The excitation functions of the two ratios are found to differ vastly. The positive ratio rises in the low energy region and exhibits a distinct peak around $\sqrt{s_{\rm NN}}$ of 7-8 GeV before dropping down at higher energy. In contrast, the negative ratio steadily increases with the energy, seemingly asymptotically approaching unity.

Previous studies [155, 15, 164] have found that K^+ and K^- abundances depend on the net baryon density. As we can tell from $\bar{p}/p$ ratio vs. $\sqrt{s_{\rm NN}}$, the baryon density changes as a function of energy. A statistical model which calculates the particle yields at chemical freeze-out predicts that the strange yields relative to non-strange yields reach a maximum near $E_{\rm beam} = 30$ AGeV ($\sqrt{s_{\rm NN}} \approx 7.7$ GeV) [165]. Therefore, a broad maximum in K^+/π^+ ratio can be expected around that energy region. K^- mesons are produced via pair production $N + N \rightarrow N + N + K^+ + K^-$.

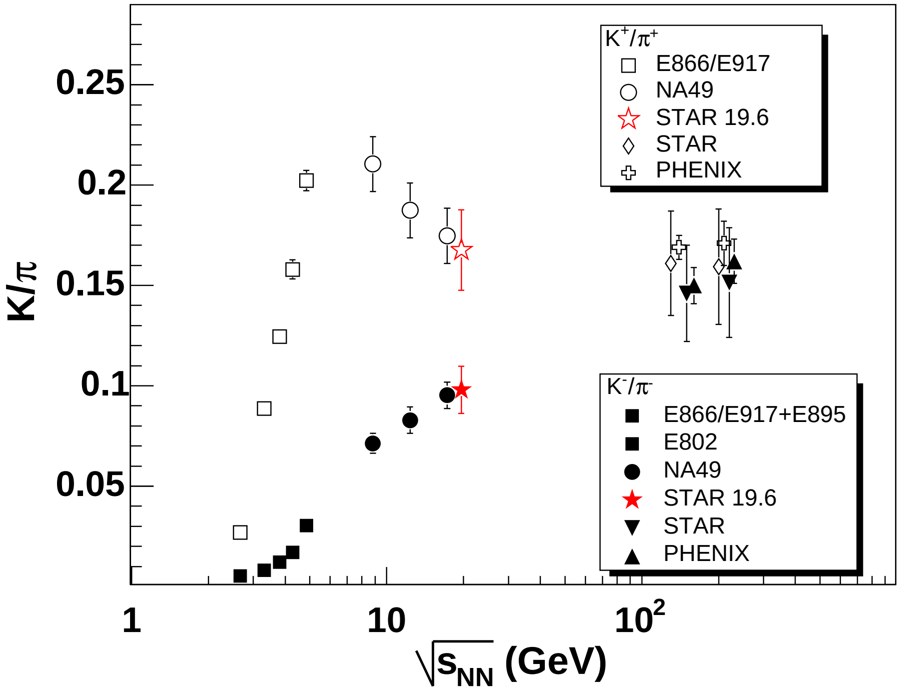

Figure 6.14. K^+/π^+ ratio (open symbols) and K^-/π^- ratio (solid symbols) excitation functions. The 19.6 GeV values are shown as stars. (data sources: E866/E917 [19], E895 [20], E802 [21], NA44 [11], NA49 [13], PHENIX [14, 22], STAR [18, 15]. For clarity, some of the 130 and 200 GeV data points are shifted to the right by 10-GeV increments.)

Therefore, as energy increases, a smooth increase in K^- production is expected. A microscopic transport model such as UrQMD [166, 167] and a study using RQMD [168] also predicted this broad maximum of K^+/π^+ ratio. However, the observed peak of the excitation function ("strangeness horn" [169, 170, 171, 172]) is sharper than expected.

Interestingly, this non-monotonic behavior of the strangeness excitation function was predicted by the Statistical Model of the Early Stage [173]. The model assumes that the production of particles in the early stage is statistical and the probability of finding a macroscopic (thermodynamic) state is $\sim e^S$, where S is the entropy. The sharp feature is reproduced in the numerical calculation when a phase transition to the QGP is assumed. Essentially, the "jump" in the positive strangeness to pion ratio has to do with the mass of the strange quarks being significantly reduced when the nuclear matter becomes deconfined ($T > T_{\text{crit}}$). The different shapes of the K^+ and K^- over pions are due to different hadronic production channels.

Overall, the 19.6 GeV K^-/K^+, $\bar{p}/p$, K^+/π^+, and K^-/π^- ratios are found to be consistent with the excitation trends established by other experiments.

At $\sqrt{s_{\text{NN}}} = 19.6$ GeV, a very small number of antiprotons is produced. At midrapidity ($|y| < 0.5$), the $\bar{p}$ yield relative to the π^- yield from 0-10%, 10-30%, and 30-50% central events are 1.73%, 1.94%, and 2.2% respectively, each with a systematic error of about 10%. The $\bar{p}/\pi^-$ ratio versus the negative reference multiplicity is shown in Figure 6.15. The small decrease of the ratio with multiplicity is in contrast to the K/π ratios.

6.3.3 π^+/π^- Ratio

The next particle ratio to consider involves the positive and negative pions–the two most-produced charged particles. The π^+/π^- ratio shows no strong dependence on either centrality or rapidity. However, there is a $m_T - m_0$ dependence in the small

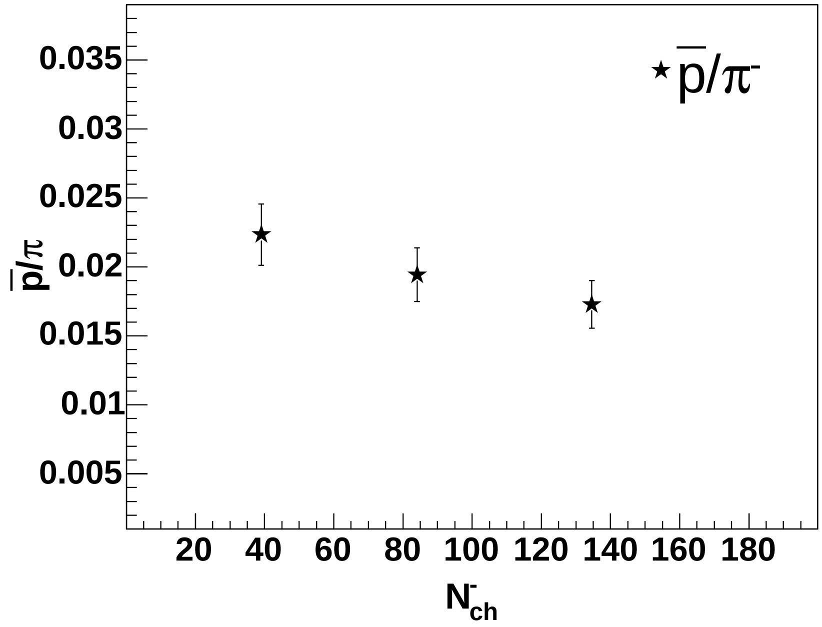

Figure 6.15. Antiproton to pion ratio as a function of reference negative multiplicity (N^{-}_{ch}).

$m_T - m_0$ region. To better investigate this effect for the 19.6 GeV data, we included additional points in the very small p_T region. They were obtained by doing PID with a very small $m_T - m_0$ bin size, so that the pion dE/dx distribution has a narrow enough width to be reliably fitted with a Gaussian.

In Figure 6.16, the π^+/π^- ratio as a function of transverse mass from the most central collisions is compared to results from other energies. Results from STAR (Au+Au at $\sqrt{s_{\mathrm{NN}}} = 200$ GeV) [18], AGS Experiment 866 (E866) (Au+Au at $\sqrt{s_{\mathrm{NN}}} =$ 4.9 GeV) [23], and SIS Kaon Spectrometer (KaoS) (Au+Au at $\sqrt{s_{\mathrm{NN}}} = 2.3$ GeV) [24] are shown.

The ratio of π^+/π^- increases with the collision energy in Figure 6.16. At low energies, pions are produced primarily via resonance decays. Excited nucleons can turn into Δ resonances, that in turn decay. The strong decay channel of the lightest delta resonance, $\Delta(1232) \to N\pi$, has a branching ratio of over 99%, this results in a

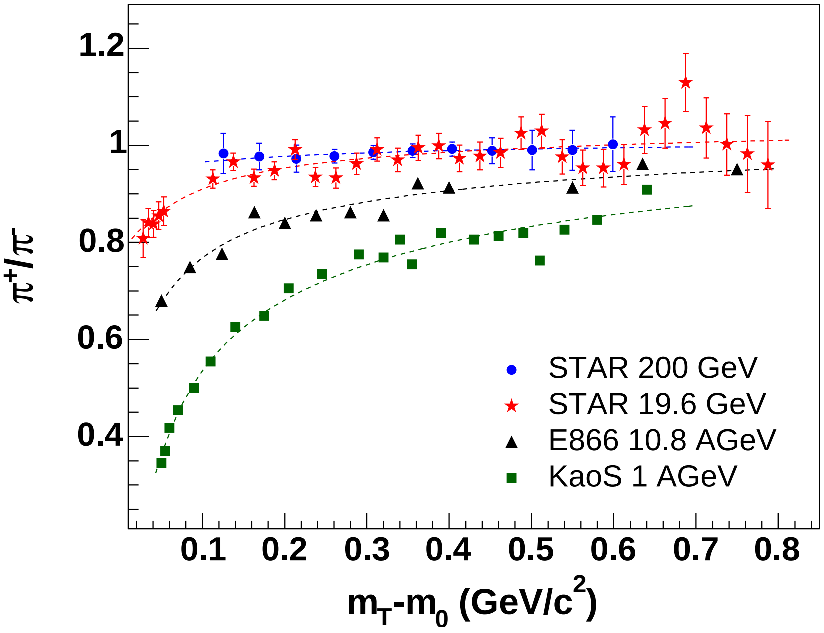

Figure 6.16. π^+/π^- ratio, $-0.1 < y < 0.1$, top 10% central. Also shown are measurements at other energies by STAR [18], E866 (AGS) [23], and KaoS (SIS) [24].

large number of pions. Since p is 1.3 MeV lighter than n whereas masses of π^+ and π^-, which are antiparticles of each other, are equal, it is more energetically favored to generate p and π^- than n and π^+.

In addition, if we neglect rescattering, the only three possible primary reactions in Au+Au collisions are p+p, p+n, and n+n. These three reactions create different numbers of π^+ and π^-. Some possible reactions which involve charged pions are

$$\begin{aligned}
p+p &\rightarrow p+n+\pi^+ \\
&\rightarrow p+p+\pi^+ + \pi^- \\
&\rightarrow n+n+\pi^+ + \pi^+ \\
&\rightarrow \ldots \text{ (net charge} = +2) \\
p+n &\rightarrow p+p+\pi^- \\
&\rightarrow n+n+\pi^+ \\
&\rightarrow p+n+\pi^+ + \pi^- \\
&\rightarrow \ldots \text{ (net charge} = +1) \\
n+n &\rightarrow n+p+\pi^- \\
&\rightarrow n+n+\pi^+ + \pi^- \\
&\rightarrow p+p+\pi^- + \pi^- \\
&\rightarrow \ldots \text{ (net charge} = 0)
\end{aligned}$$

In symmetric collisions between ${}^{A}_{Z}X_N$ nuclei, there are N^2 possible n+n collisions, Z^2 of p+p, and $2ZN$ of p+n collisions. In low-energy collisions, according to [174], $\dfrac{\pi^+}{\pi^-} \approx \left(\dfrac{Z}{N}\right)^2$. For heavy nuclei, $Z < N$ which leads to $\pi^+ < \pi^-$.

At higher energy, pair productions dominate resonance decays. A pair production results in the same number of positive and negative pions. Following this logic, the π^+/π^- ratio is supposed to reach unity as the energy goes up. At large $m_T - m_0$, Figure 6.16 shows that the pion ratio has nearly saturated to 1.0 at center-of-mass energy $\leq$ 19.6 GeV.

We also observe noticeable suppression of the ratio at low $m_T - m_0$, in the three lower beam energies. For $m_T - m_0 >$ 150 MeV, the 200 GeV ratio is very similar to the 19.6 GeV ratio. The shape of the pion ratio can be interpreted as a result of Coulomb interactions between the emitting source and the outgoing charged particles

[175, 176, 177, 178, 179, 23]. The positively charged source attracts π^- toward itself, decreasing their energies, but increases π^+ energies by repelling them. This energy modification leads to the shift in the pion thermal spectra. As the lightest hadrons produced, pions experience this effect the most.

If we let E_0 be the pion energy at the kinetic freeze-out, the final energy ($E_f = m_T \cosh y$) of $\pi^\pm$ arriving at the detector will be modified by the Coulomb potential energy

$$(E_f)_{\pi^\pm} = E_0 \pm V_C \tag{6.8}$$

The final spectrum phase space is modified by the Jacobian [24]:

$$\begin{aligned}
\frac{\partial^3 p_0}{\partial^3 p} &= \frac{p_0^2 \partial p_0}{p^2 \partial p} && (6.9)\\
&= \frac{p_0 E_0 \partial E_0}{p E \partial E} && (6.10)\\
&= \frac{p_0 E_0}{p E} && (6.11)\\
E\frac{d^3N}{d^3p} &= E\frac{d^3N_0}{d^3p_0}\frac{p_0 E_0}{pE} && (6.12)\\
&= E_0\frac{d^3N_0}{d^3p_0}\frac{p_0}{p} && (6.13)\\
\left(E\frac{d^3N}{d^3p}\right)_{\pi^\pm} &= E_0\frac{d^3N_0}{d^3p_0}\frac{\sqrt{E_0^2 - m_0^2}}{\sqrt{(E_0 \pm V_C)^2 - m_0^2}} && (6.14)
\end{aligned}$$

If the primordial energy (E_0) is expressed in terms of the final energy (E_f),

$$\left(E\frac{d^3N}{d^3p}\right)_{\pi^\pm} = (E_f \mp V_C)\frac{d^3N_0}{d^3p_0}\frac{\sqrt{(E_f \mp V_C)^2 - m_0^2}}{\sqrt{E_f^2 - m_0^2}} \tag{6.15}$$

If we use a Maxwell-Boltzmann function to describe the primordial pion thermal distribution (d^3N_0/d^3p_0), then the ratio can be written as

$$\begin{aligned}
\frac{\pi^+}{\pi^-} &= \left(E\frac{d^3N}{d^3p}\right)_{\pi^+} \Big/ \left(E\frac{d^3N}{d^3p}\right)_{\pi^-}\\
&= \left(\frac{E_f - V_C}{E_f + V_C}\right)\frac{\sqrt{(E_f - V_C)^2 - m_\pi^2}}{\sqrt{(E_f + V_C)^2 - m_\pi^2}} R e^{2V_C/T} && (6.16)
\end{aligned}$$

with R being the primordial pion ratio.

Based on the model in [179], which introduces an effective potential due to proton emission dynamics, V_C for top 10% central collisions is found to be 8.54 ± 0.94 MeV, which is consistent with the result at SPS energy of 17.3 GeV of 8.2 ± 0.5 MeV, analyzed in [179]. Reference [179] also found that the Coulomb potential decreases with the beam energy. This suggests the net baryon reduction in the central region and/or larger radial expansion of the source.

The Coulomb force acts on all charged particles at any distance, therefore the produced charged kaons, protons, and antiprotons feel the effects as well. The effects on those heavy particles, however, are small compared to the effects on the pions. For example, let's consider $y = 0$ particles where $E_f = m_T$. At a fixed value of V_C, the ratio of positive and negative particles of the same mass, m, is

$$\frac{\text{positive}}{\text{negative}} = \left(\frac{m_T - V_C}{m_T + V_C}\right) \frac{\sqrt{(m_T - V_C)^2 - m^2}}{\sqrt{(m_T + V_C)^2 - m^2}} Re^{2V_C/T} \tag{6.17}$$

Heavy particles have higher m and T values. Using the 0-10% centrality T results from Table C.10, the different Coulomb effects can be seen for three different particle masses in Figure 6.17.

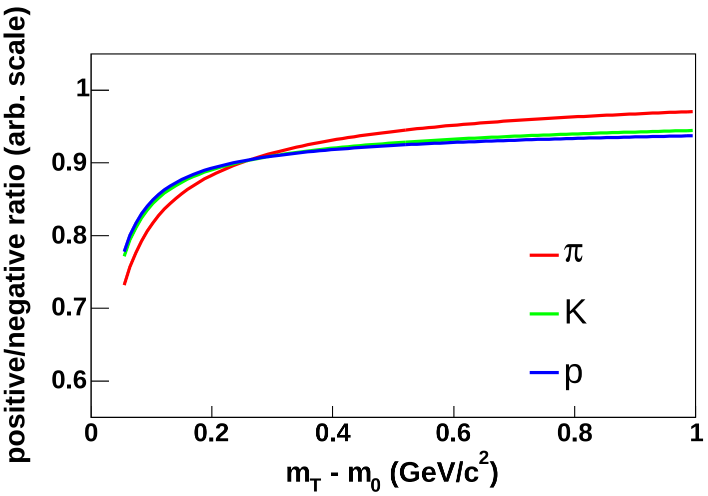

Figure 6.17. Coulomb effects on different positive/negative particle ratios. The normalization is arbitrary.

6.4 Mean Transverse Momentum

A natural observable we can obtain from a transverse mass or transverse momentum spectrum is the mean value of p_T. The behaviors of mean transverse momentum for different particles and in different collision systems have been extensively studied. What can we learn from mean p_T? In general, $\langle p_T \rangle$ can give us the information on the transverse dynamics of different types of particles. Obtained by integrating the spectra, $\langle p_T \rangle$ gives us information on the flow directly from the data and is relatively model independent. (It obviously still depends on the extrapolation of the fit functions.) Furthermore, the fluctuations of $\langle p_T \rangle$ between events can be used to investigate the signals of the QCD phase transition [180].

We obtained the p_T spectra by converting each $m_T - m_0$ coordinate of the transverse mass histogram into p_T. The invariant yield on the y axis needs no conversion since

$$\begin{aligned} m_T &= \sqrt{p_T^2 + m_0^2} && (6.18) \\ \frac{dm_T}{dp_T} &= 2p_T \frac{1}{2\sqrt{p_T^2 + m_0^2}} = \frac{p_T}{m_T} && (6.19) \\ m_T\, dm_T &= p_T\, dp_T && (6.20) \\ \frac{d^2N}{m_T\, dm_T\, dy} &= \frac{d^2N}{p_T\, dp_T\, dy} && (6.21) \end{aligned}$$

The fit functions were then integrated over p_T range of 0 to 10 GeV/c, which covers essentially the entire phase space occupied by the particles:

$$\langle p_T \rangle = \frac{\int_0^{10} (f \cdot p_T \cdot p_T)\, dp_T}{\int_0^{10} (f \cdot p_T)\, dp_T} \qquad (6.22)$$

where f is the fit function to the spectra.

The mean transverse momenta for midrapidity particles in different centrality bins are tabulated in Table C.12.

$\langle p_T \rangle$ for different hadrons is shown in Figure 6.18.

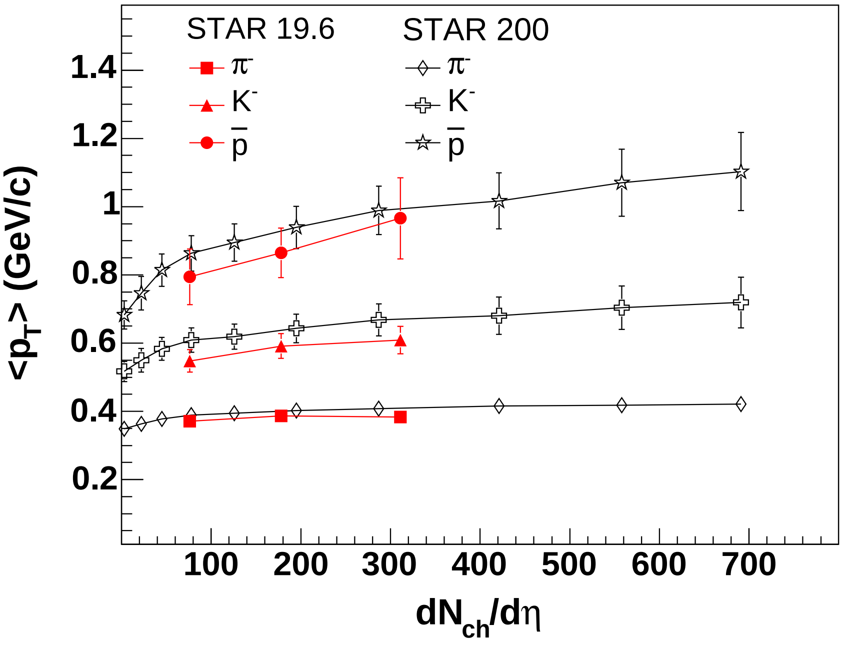

Figure 6.18. Mean transverse momentum of midrapidity particles, $|y| < 0.1$, versus $dN_{\rm ch}/d\eta$. Results are compared with STAR 200 GeV results. The 19.6 GeV results for the positive particles are extremely close to the corresponding negative species. The leftmost points of the 200 GeV are p+p results.

The values have been averaged from different fit functions [2]. To calculate the averages, for pions and kaons the results from Maxwell-Boltzmann, Bose-Einstein, Siemens-Rasmussen, and blast wave fits are used. For protons and antiprotons, only Siemens-Rasmussen and blast-wave results are used. For 0-10% most central events, the pion values from different fit functions are within 2% of the average values. For kaons, they are about 5%. The variations are 2% and 10% for protons and antiprotons, respectively. The values of $\langle p_T \rangle$ is plotted against $dN/d\eta$ in order to draw comparison to the STAR 200 GeV results [18]. Thus, some of the most peripheral bins of pions and kaons are omitted from the figure, but can be referred to from Table C.12.

Results at both energies show similar trends. The mean p_T of pions and kaons are relatively flat, whereas the protons and antiprotons $\langle p_T \rangle$ noticeably increase with centrality. At a higher collision energy, the produced particles are expected to fly out at higher p_T. The 19.6 GeV Au+Au results for each particle species are approximately equal or slightly higher than the p+p results taken at 200 GeV, indicating that significant rescattering is present inside the nuclear matter created in Au+Au.

6.5 Pseudorapidity Density

To obtain the corrected pseudorapidity density of charged particles ($dN_{\mathrm{ch}}/d\eta$), first the invariant yield (equation (6.23)) was numerically integrated from $m_T - m_0$ = 0 to 10 GeV/c^2. This gives dN/dy, which we then used $\partial y/\partial\eta \sim \Delta y/\Delta\eta$ to estimate $dN_{\mathrm{ch}}/d\eta$.

---

[2] See Section 6.1 for functions associated with different particle spectra.

$$
\begin{aligned}
A &\equiv \frac{d^2N}{2\pi m_T\, dm_T\, dy} && (6.23)\\
\frac{dN}{dy}(m_T - m_0) &= A \times 2\pi m_T\, dm_T && (6.24)\\
\frac{dN}{d\eta}(m_T - m_0) &= \frac{dN}{dy}(m_T - m_0) \times \frac{\Delta y}{\Delta \eta}(y, m_T - m_0, m_0) && (6.25)\\
\frac{dN}{d\eta} &= \int \frac{dN}{d\eta}(m_T - m_0)\, dm_T && (6.26)
\end{aligned}
$$

where $\Delta y/\Delta\eta = (y_{\text{hi}} - y_{\text{lo}})/(\eta_{\text{hi}} - \eta_{\text{lo}})$. η can be calculated from $m_T - m_0$, m_0, and y.

Table C.13 lists $dN_{\text{ch}}/d\eta$ values for each (rapidity, centrality) bin. The values are relatively higher than the reference multiplicity, N_{ch} (defined in 3.3), which are used to determine centrality.

For the top 10% central collisions, $|y| < 0.1$, we extracted

$$
\frac{dN_{\text{ch}}}{d\eta}\frac{1}{0.5\langle N_{\text{part}}\rangle} = 1.96 \pm 0.03(\text{stat.}) \pm 0.16(\text{syst.}) \tag{6.27}
$$

where N_{part} is the number of participants from the optical Glauber model calculation (Appendix E and [181]).

	0-10%	10-30%	30-50%	50-70%
$< N_{\text{part}} >$	317.9	192.3	90.8	35.5

Table 6.1. The Glauber model's average number of participants for each centrality class.

In Figure 6.19 the energy dependence of the pseudorapidity density per participant pair is shown. There is a smooth logarithmic increase of $dN_{\text{ch}}/d\eta/\langle 0.5N_{\text{part}}\rangle$ with $\sqrt{s}$. The 19.6 GeV $dN/d\eta$ value falls along the trend established by other experiments, and agrees very well with PHOBOS measurement at the same energy. The value of $dN/d\eta$ per number of participant pairs is close to a prediction from a "parton saturation" model [182, 183], of 1.95 ± 0.1 at $\sqrt{s_{\text{NN}}} = 22$ GeV, or 1.87 at 19.6 GeV [31].

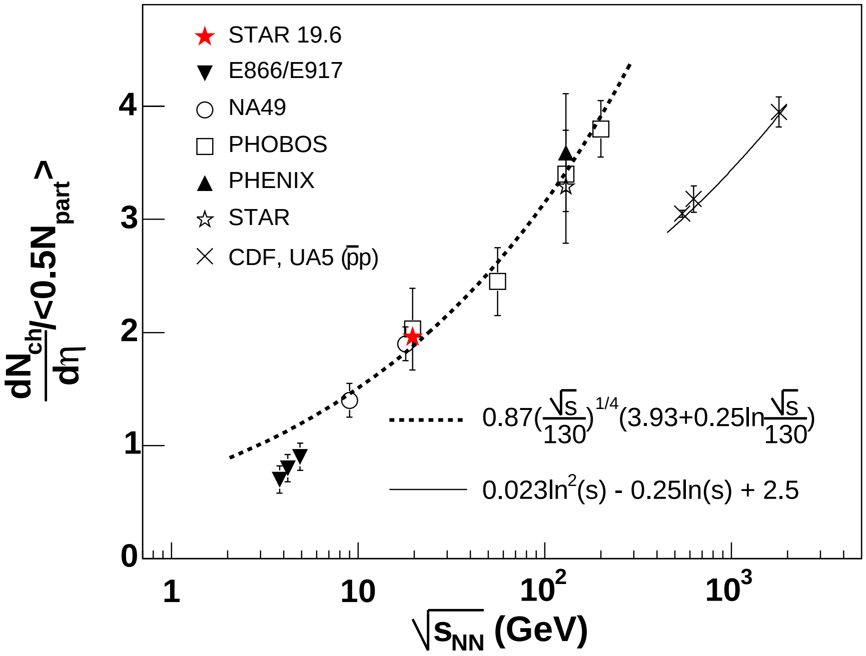

Figure 6.19. $\frac{dN/d\eta}{\langle 0.5N_{\rm part}\rangle}$ as a function of $\sqrt{s_{\rm NN}}$. (data sources: (PHOBOS [25, 26, 27], PHENIX [28], and STAR [29, 30]. NA49 and E866/E917 points are taken from [27]. Dashed line is the prediction (not a fit) from parton saturation model [31].) Results from $\bar{\rm p}$+p collsions (CDF [32], UA5 [33]) are shown for comparison. The functional fit (solid line) is done in [32].

An implication of the parton saturation model's success in describing larger-s_{NN} energy dependence of the multiplicity at central η per participant pair is that parton saturation may have set in around $\sqrt{s_{\mathrm{NN}}} = 19.6$ GeV or lower (SPS energies). In other words, such energy is high enough that small-x regime of parton distribution functions [184] (where densities of gluons and sea quarks dominate) becomes significant.

6.6 Chemical Freeze-Out

When inelastic collisions cease, the chemical equilibrium is reached, meaning that particle abundances are fixed (except some resonances, which will decay). Since the integrated hadron yields only change prior to chemical freeze-out, we can learn about the state of the system at the chemical freeze-out from the extracted particle yields and ratios.

Statistical (thermal) approaches [185, 186] can be used to obtain the freeze-out temperature and the chemical potentials of the system. The data used are from midrapidity, not full 4π yields. Previous study [187] indicates that taking the particle ratios cancels out unwanted effects such as volume corrections, transverse and longitudinal flow.

The statistical model assumes that particles are produced from a thermally equilibrated source. The system of particles is treated as a grand canonical (GC) ensemble. In a GC system, energy (E) and number of particles (N) can be exchanged between the fireball system and the heat reservoir. In a GC system, the partition function can be expressed as

$$Z = \sum_i \exp\left(-\frac{E_i - \mu N_i}{T}\right) \tag{6.28}$$

where E_i is the energy of particle species i, and the chemical potential is the same for all species.

The average number of particles can then be derived from Z

$$\begin{aligned} \langle N \rangle &= \frac{\sum\limits_i N_i \exp(-(E_i - \mu N_i)/T)}{\sum\limits_i \exp(-(E_i - \mu N_i)/T)} \\ &= \frac{1}{Z} T \frac{\partial Z}{\partial \mu} \\ &= T \frac{\partial \ln Z}{\partial \mu} \end{aligned} \tag{6.29}$$

From [185], the number density (not actual yield) for particle i integrated over momentum can be written as

$$\rho_i = \frac{g_i}{2\pi^2} \int_0^\infty \frac{p^2\, dp}{\exp((E_i - \mu_i)/T) \pm 1} \tag{6.30}$$

where g_i is the spin-isospin degeneracy, defined as $(2J+1)(2I+1)$ with J and I being the spin and isospin numbers. From [43], $J_{\pi^\pm} = 0$, $I_{\pi^\pm} = 1$, $J_{K^\pm} = 0$, $I_{K^\pm} = 1/2$, $J_{p,\bar{p}} = 1/2$, and $I_{p,\bar{p}} = 1/2$. In the denominator of the integrand, $+$ is for bosons, $-$ is for fermions. Unlike in th partition function (equation (6.28)), the chemical potential in equation (6.30) has a subscript i. This is because $\mu_i = \mu_B B_i - \mu_S S_i - \mu_{I_3} I_{3,i}$ is dependent on baryon number, strangeness numbers, and isospin of each species.

Since we do not have 4π particle yields, it is essential to use the ratios. To extract the freeze-out temperature and chemical potentials from our particle ratios, we took the functional form used in [188],

$$\rho_i = \gamma_s^{\langle s+\bar{s} \rangle_i} \frac{g_i}{2\pi^2} T_{\mathrm{ch}} m_i^2 K_2\left(\frac{m_i}{T_{\mathrm{ch}}}\right) \lambda_q^{Q_i} \lambda_s^{s_i} \tag{6.31}$$

K_2, which comes from the integral term, is the modified Bessel function of the second kind (Appendix F). The fugacity parameters (λ's) are defined as:

$$\lambda_q \equiv e^{\mu_q / T_{\mathrm{ch}}} \tag{6.32}$$

$$\lambda_s \equiv e^{\mu_s / T_{\mathrm{ch}}} \tag{6.33}$$

- μ_q and μ_s are the chemical potentials of light (u, $\bar{u}$, d, $\bar{d}$) and strange (s, $\bar{s}$) quark flavors, respectively. The baryon chemical potential, μ_B, can be calculated from $\mu_B = 3\mu_q$.

- m_i is the particle's mass.
- strangeness number $s_i = \langle s - \bar{s} \rangle$ and quark number $Q_i = \langle u + d - \bar{u} - \bar{d} \rangle_i$ are fixed for each species of particle.

The essential parameters that describe the particle density are the chemical freeze-out temperature (T_{ch}), the baryon chemical potential (μ_B), the strangeness chemical potential $\mu_S = \mu_q - \mu_s$, and the strangeness saturation factor γ_s, which can be expressed in term of net strangeness fugacity, $\gamma_s = \exp(\mu_{\langle s+\bar{s} \rangle}/T)$ [186]. The definition of γ_s is given in [189, 190] as

$$\gamma_s \equiv \frac{\text{strangeness density}}{\text{equilibrium density}} \tag{6.34}$$

The input ratios used in this study are the π^+/π^-, K^-/K^+, $\bar{p}/p$, K^-/π^-, and $\bar{p}/\pi^-$ ratios. They are averaged over the midrapidity range $-0.5 < y < 0.5$. In this analyssis, there are five data points and four free parameters (T_{ch}, μ_q, μ_s, and γ_s). Although we have a limited number of particle species to work with, it is still interesting to see what freeze out conditions are at this energy. Results are shown in Figure 6.20 and tabulated in Table C.14 (Appendix C).

The chemical freeze-out temperature of 164.7 ± 0.5 MeV is obtained for the 10% most central data. $\mu_q = 68.5 \pm 0.2$ MeV ($\mu_B = 205.5 \pm 0.6$ MeV) and $\mu_s = 27.2 \pm 0.9$ MeV ($\mu_S = 41.3 \pm 0.9$ MeV). Our T_{ch} is similar to both that of the STAR 200 GeV (157 ± 6 MeV) [18] and 17.3 GeV SPS data (168 ± 2.4 MeV) [185]. The baryon chemical potential at $\sqrt{s_{\text{NN}}} = 19.6$ GeV falls in between the 200 GeV results that STAR measured (22 ± 4 MeV) and the result of 266 ± 5 MeV from the SPS data. The result seems to support the notion that the measured hadrons are generated from a well-equilibrated thermal source, at a temperature near the predicted phase transition, T_{crit} (~ 175 MeV).

The results for all centrality bins are listed in Table C.15. The parameters are plotted against $dN_{\text{ch}}/d\eta$ in Figure 6.21. Contour plots of T_{ch} and μ_q are shown in

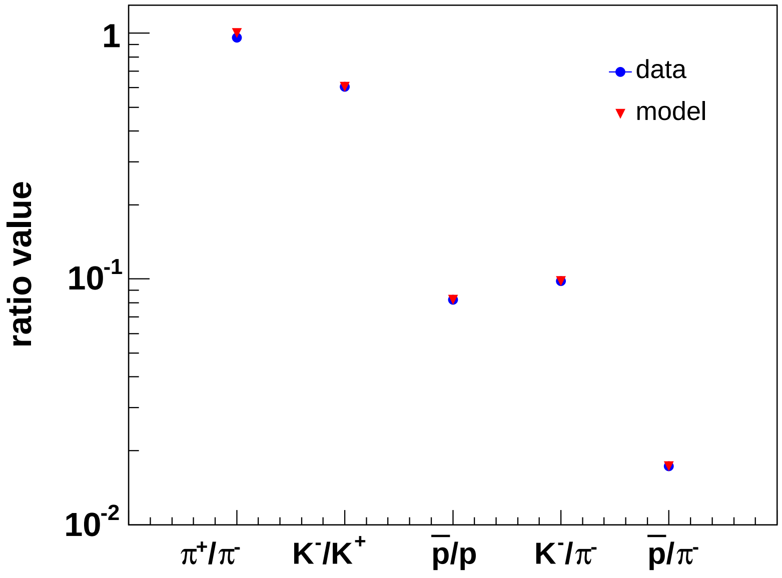

Figure 6.20. Comparison of the statistical model fit results and the data from the top 10% central events of Au+Au at $\sqrt{s_{\mathrm{NN}}} = 19.6$ GeV.

Figure 6.22.

Figure 6.23 shows T_{ch} versus μ_B from different experiments. The variation in T_{ch} suggests that the chemical freeze-out temperature is dependent on the existence of a nuclear medium.

Using the hadronic gas model with chemical equilibrium [191], this "chemical freeze-out curve" can be reproduced when the system is assumed to freeze out at either of these following scenarios:

- energy per produced hadron is 1 GeV [192, 193].
- net baryon density is 0.12 fm^{-3} [194]

We can see from Figure 6.23 that the baryon chemical potential is vanishing with the increasing beam energy, whereas the temperature is reaching the critical temperature predicted by lattice QCD.

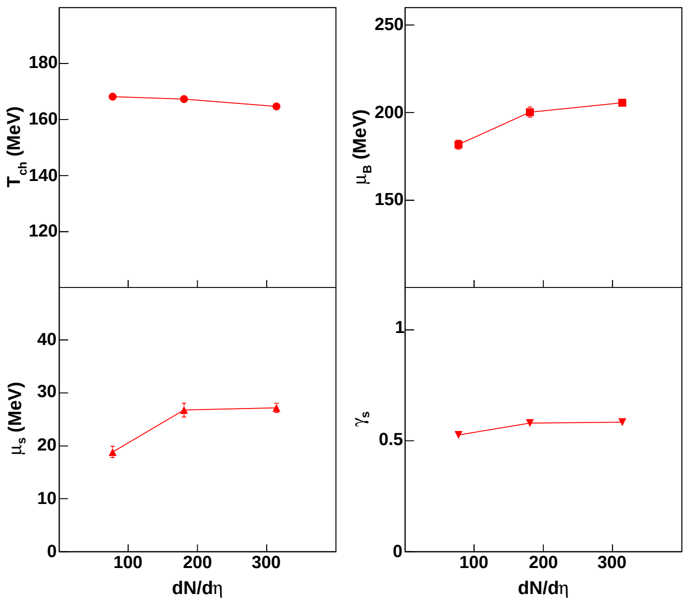

Figure 6.21. Chemical freeze-out parameters from the fits as functions of centrality classes.

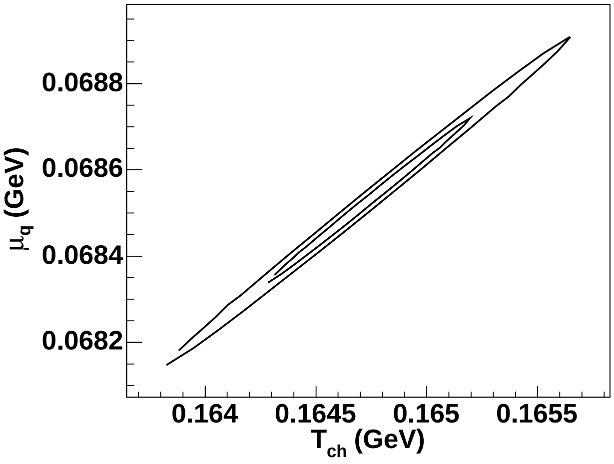

Figure 6.22. Contour plots (1 and 2 σ) of T_{ch} and μ_q parameters from the statistical model fit, for top 10% central events.

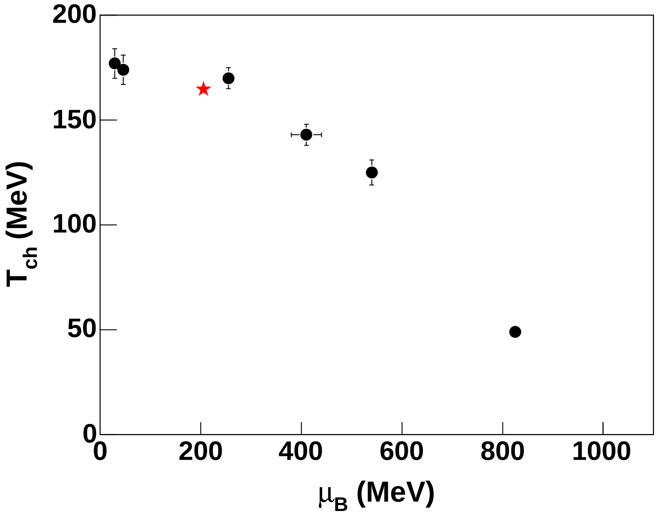

Figure 6.23. The phase diagram of nuclear matter from different collision systems. (data sources: see Table C.16.)

In elementary collisions, although each event contains a small multiplicity, a collection of those events contains large enough number of particles and thus appears statistical (for example, see [195, 196]). This scenario is called "phase-space dominance" [197, 198]. In elementary collisions, the fit parameters in the statistical models serve as "Lagrange multipliers," with the constraint equations being the conservation laws (e.g., of baryon number, electrical charge, and strangeness), and the function to be maximized is the entropy. In a simple-minded picture, a nucleus-nucleus collision can be thought of as a superposition of nucleon-nucleon collisions. T_{ch} parameter would be the temperature of the thermal system at QGP-to-hadrons transition and the chemical potentials would have something to do with the number densities. In essence, the statistical model provides a check for a statistically distributed source, not a proof of an equilibrated source.

6.7 Kinetic Freeze-Out

After inelastic mean free path exceeds the system size at chemical freeze-out, the particles continue to collide elastically, changing their energy and momentum distributions. As the expanding hadronic system becomes further dilute and colder (the elastic mean free path approximately equal to the system size), it reaches a kinetic freeze-out [199]. At this stage, the particles can be approximated as streaming freely toward the detectors. From the particle spectra, we can find out about the conditions of this final freeze-out.

The distributions of the particles do not follow purely statistical models in which the particles thermalize via random motion. The intense pressure of the collision region leads to a collective expansion ("flow") of the produced particles. We will focus on flow in the transverse plane (β_T) since the transverse motion is produced entirely from the collision. In longitudinal direction ($\eta \neq 0$) the situation is more complicated since the collectivity of the particles is coupled with the longitudinal dynamics of the pre-collision nuclei. In heavy ion collisions, collective flow is interesting because it is a nuclear effect, which we do not see in the elementary nucleon-nucleon collisions. The evolution of flow depends on thermalization and therefore is an important link to quark-hadron phase transition.

The two following phenomenological models have been used in analyzing the collective flow in heavy ion collisions. Much lower energy data, such as those from SPS, seem to favor one, while the higher energy experiments at RHIC tend to use the other. At $\sqrt{s_{\mathrm{NN}}} = 19.6$ GeV, our energy lies between SPS and RHIC energy regimes. Our spectral results will be compared with both models.

6.7.1 Siemens and Rasmussen Model

One of the earliest blast wave formulations of the particle production in heavy ion collisions was the work by Siemens and Rasmussen in 1979 [200]. Pion and proton data from collisions of Ne on NaF at lab $E_{\text{kin}} = 0.8$ GeV were studied and signs of an exploding source were investigated. In this model, a particle distribution is affected by the pressure wave produced from the collision. The invariant yield is described by

$$\frac{d^2N}{m_T dm_T dy} = Ae^{-\gamma E/T}\left(\frac{\sinh(\alpha)}{\alpha}(\gamma E + T) - T\cosh(\alpha)\right) \tag{6.35}$$

where A is the normalization constant, $\gamma = (1-\beta^2)^{-1/2}$, and $\alpha = \gamma\beta p/T$. β is the radial flow velocity and T is the temperature of the expanding source. In the limit $\beta \to 0$, equation (6.35) becomes a Maxwell-Boltzmann thermal distribution, $\sim \exp(-E/T)$.

The fits for top 10% central spectra at midrapidity are shown in Figure 6.24. (Tabulated results are in Table C.17.)

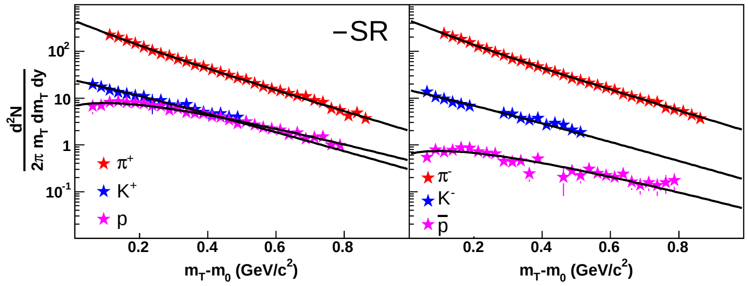

Figure 6.24. Siemens-Rasmussen fits on the midrapidity spectra of top 10% centrality class.

The contour plot of the extracted flow velocity and temperature for the midrapidity spectra is shown in Figure 6.25. The most central collisions produce largest β.

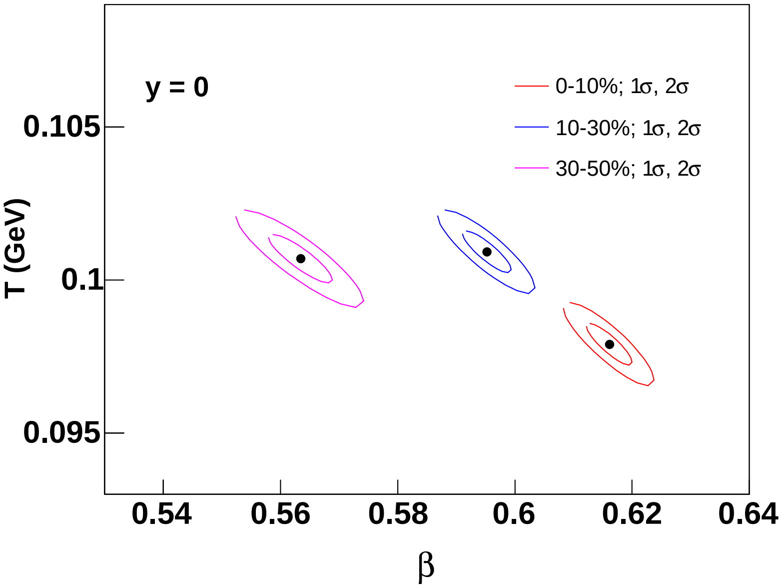

Figure 6.25. 1σ and 2σ contours of β and T from Siemens-Rasmussen fits for midrapidity spectra in three different centrality classes at midrapidity.

6.7.2 Blast Wave Model

In this commonly-called blast wave model [201], instead of a spherically symmetric expansion, Schnedermann, Sollfrank, and Heinz formulate the collision as a transverse cylindrical expansion and invoke the Bjorken longitudinal boost-invariant plateau at midrapidity [152].

The parametrization is based on the fixed-target ^{32}S + ^{32}S measurements (transverse mass spectra and dN/dy) at 200 AGeV by NA35 [202], the transverse mass spectra of different particles are described by the flow velocity in the transverse direction, β_T, the flow profile parameter, n, and the kinetic freeze-out temperature, T_{kin}.

The model is similar to a hydrodynamical picture [203, 204, 60]. Instead of a hot gas, a collision between two heavy nuclei are supposed to generate a dense system of particles such that those particles thermalize and move collectively with zero mean free path. This hydro-like nature is analogous to molecules of water inside a single container. In hydrodynamics, a fluid cell at $x \equiv (t, \vec{x})$ can be described by energy density, pressure, four-velocity $u^\mu(x)$, and conserved charge densities (baryon number, strangeness, electrical charges, ...etc). The evolution of the fluid is governed by the conservations of energy, momentum, and charge currents. With a specification of the equation of state (EoS), i.e., the pressure as a function of energy density and conserved charge densities, the dynamics of the fluid can be obtained.

In this hydro-inspired model, a flow profile is used to describe the transverse flow velocity of a fluid element at distance r from the center of the emission source. Unlike the spherical expansion model by Siemens and Rasmussen in which the flow velocity has a single value, as for emission only from the surface of the sphere, the blast wave flow profile is parametrized as a function of the surface velocity β_s of the expanding cylinder and a parameter n:

$$\beta_T(r) = \beta_s \left(\frac{r}{R}\right)^n \tag{6.36}$$

Similar to the Hubble expansion of the universe ($v = Hr$), in the blast-wave model the particles closer to the center of the fireball move slower than the ones on the edges. Dynamical freeze-out occurs when the time between collisions is in the same order as the Hubble time [205].

The transverse mass spectrum is then described by a superposition of thermal distributions boosted with a transverse rapidity $\rho(r) = \tanh^{-1} \beta_T(r)$:

$$\frac{dN}{m_T\, dm_T} \propto \int_0^R r\, dr\, m_T I_0 \left(\frac{p_T \sinh \rho(r)}{T_{\text{kin}}}\right) K_1 \left(\frac{m_T \cosh \rho(r)}{T_{\text{kin}}}\right) \tag{6.37}$$

where I_0 and K_1 are the modified Bessel functions.

The behavior of the function with differing mass, β_s, and T_{kin} is illustrated in Figure 6.26.

The global blast-wave fits for midrapidity spectra are shown in Figure 6.27. A simultaneous fit for each case of (centrality, rapidity) was done by concatenating six spectra successively into one histogram, each occupying a 1-GeV range of $m_T - m_0$,

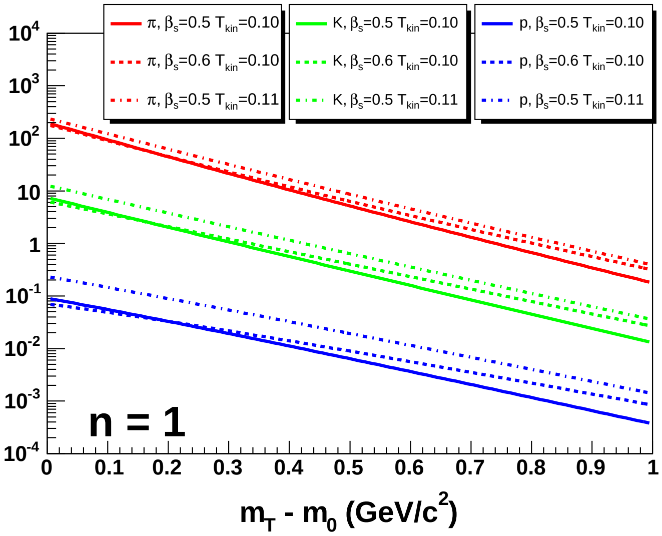

Figure 6.26. Blast wave function with varying m, β_s, and T_{kin}. The flow profile of $n = 1$ is used in this figure. The normalization is arbitrary.

then fitting each range with a common set of $(T_{\text{kin}}, \beta_s, n)$. (Tabulated fit results are in Table C.18.)

Comparisons with other fit functions are shown in Figure 6.28. We applied the function to the spectra in the top three centralities for which we have the spectra of all six species. The fit is done with n being a free parameter. Although β_s is the real parameter, the average value of β_T is often quoted in literature. The radially

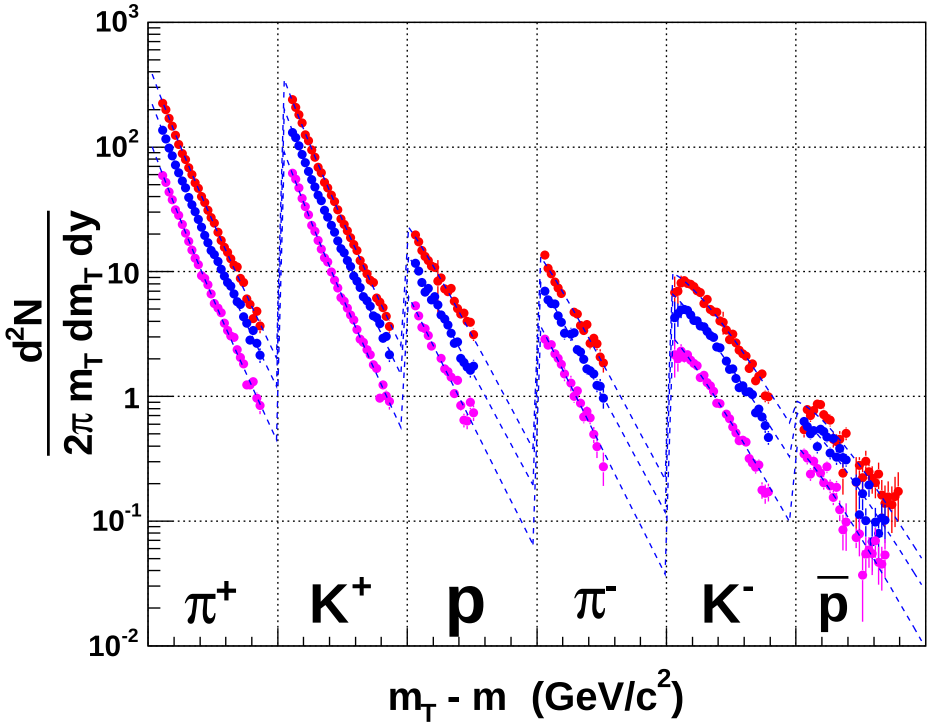

Figure 6.27. Blast wave fits to the midrapidity ($|y| < 0.1$) particle spectra. From top to bottom are top 10% central, 10-30% central, and 30-50% central collisions.

averaged β_T can be calculated from β_s and n,

$$\begin{aligned}
\langle\beta_T\rangle &= \frac{\int_0^R d^2r\,\beta_T}{\int_0^R d^2r} \\
&\quad \text{(in this model, } r \text{ lies in a 2-d plane)} \\
&= \frac{\int_0^{2\pi}\int_0^R dr\,r\,d\phi\beta_s(r/R)^n}{\int_0^{2\pi}\int_0^R dr\,r\,d\phi} \\
&= \frac{\beta_s}{R^n}\frac{\int_0^R dr\,r^{n+1}}{\int_0^R dr\,r} \\
&= \frac{\beta_s}{R^n}\frac{R^{n+2}/(n+2)}{R^2/2} = \frac{2\beta_s}{n+2} \qquad (6.38)
\end{aligned}$$

T_{kin} and $\langle\beta_T\rangle$, versus $dN_{\text{ch}}/d\eta$ are shown in Figure 6.29. The 200 GeV results from STAR [18] are also shown for comparison. Within the error bars, the results from the two energies are indistinguishable.

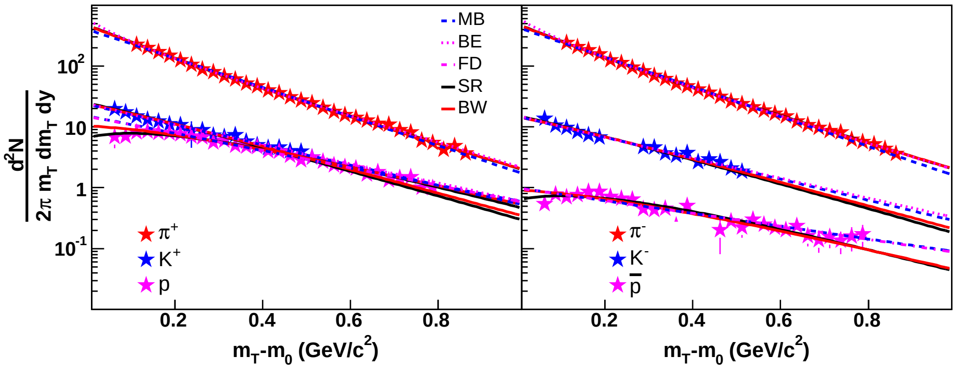

Figure 6.28. Functional fits to the midrapidity ($|y| < 0.1$), top 10% central events. The left panel are the positive species, the right are the negative. Legends: MB means Maxwell-Boltzmann, BE Bose-Einstein, FD Fermi-Dirac, SR Siemens and Rasmussen, and BW blast wave model.

The particle spectra can be described well by a single local freeze-out temperature

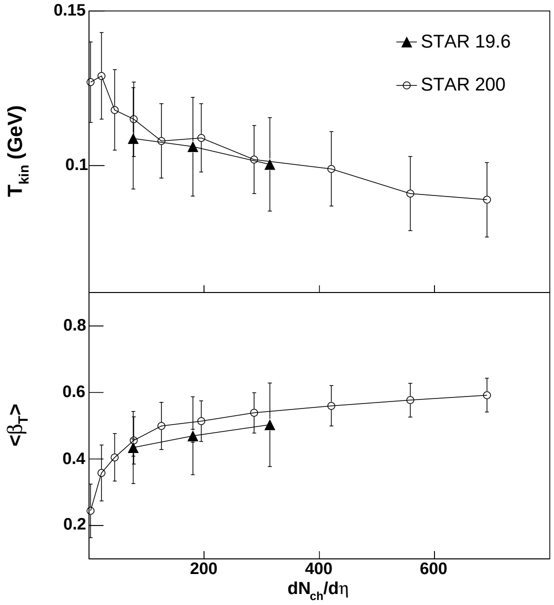

Figure 6.29. T_{kin} and $\langle\beta_T\rangle$ extracted from the blast wave fits versus $dN/d\eta$. Results are compared to STAR 200 GeV values.

and a single flow profile. This tells us that the system is dense enough that the particles rescattered and possibly thermalized.

From the results, we can see that in the more central collisions, particles freeze out at slightly lower temperatures and transverse flow becomes stronger. The increase in the flow velocity could be due to the central collisions having larger system size and higher internal pressure, therefore resulting in more violent outward expansions. These expansions take longer to achieve at lower density. As we go from top 10% central to 30-50% central events, the local kinetic freeze-out temperature T_{kin} increases by 8.4%, whereas the average transverse flow velocity $\langle\beta_T\rangle$ decreases by 13.7%. The same trend of centrality dependence was observed at 200 GeV by PHENIX [206, 207] and STAR [18]).

In the most central events, we found T_{kin} to be 100.4 ± 1.1 MeV, $\beta_s = 0.70 \pm 0.01$, and $\langle\beta_T\rangle = 0.50 \pm 0.02$. The n parameter has values near 1, varying from 0.78 ± 0.07 in central to 0.92 ± 0.14 in peripheral events. From the n values, the flow profiles of different centrality and rapidity cases can be plotted (Figure 6.30). As a test, when we fixed the T_{kin} to be the chemical freeze-out temperature ($T_{\text{ch}} \sim 165$ MeV), the fit completely failed.

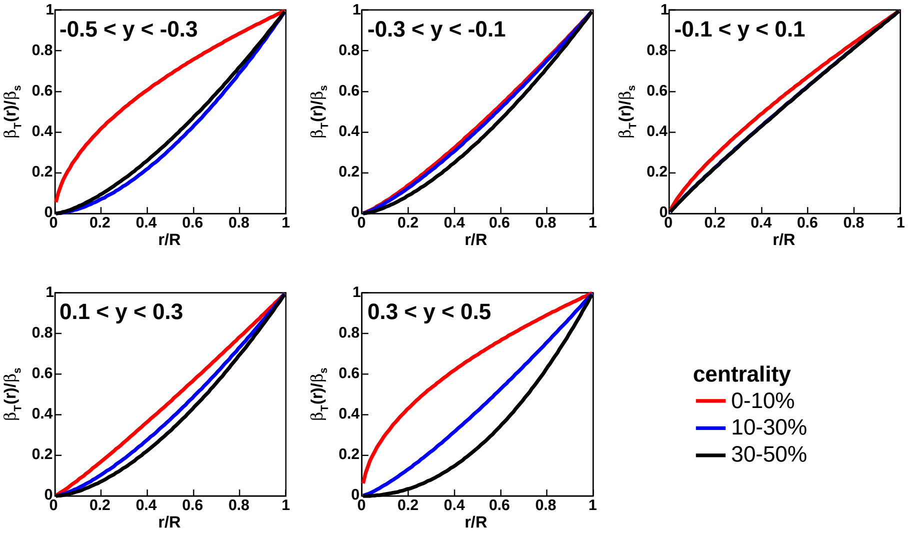

Figure 6.30. Ratio of radial to surface velocity as a function of radius for different centrality and rapidity classes.

The rapidity dependence of the kinetic freeze-out temperature and mean transverse flow velocity are shown in Figure 6.31.

The contour plot of the extracted flow velocity and temperature for the midrapidity spectra is shown in Figure 6.32. Other contour plots are in Appendix B.

From the range of rapidity studied, the relative systematic errors of the kinetic freeze-out temperature and the average flow velocity, determined from their variations, are estimated to be 10% for T_{kin} and 5% for $\langle \beta_T \rangle$.

To further estimate the systematic errors from the blast wave fits, we also studied the effects that the flow profile parameter, n, has on the values of T_{kin} and $\langle \beta_T \rangle$. For the case of top 10% centrality and $|y| < 0.1$, we fixed n at 0.5, 1.0, 1.5, 2.0, and 2.5. From the different values of n, while the fits to the spectra are still reasonable, we see that T_{kin} changes by as much as 15%, and $\langle \beta_T \rangle$ by 25% (Table C.19).

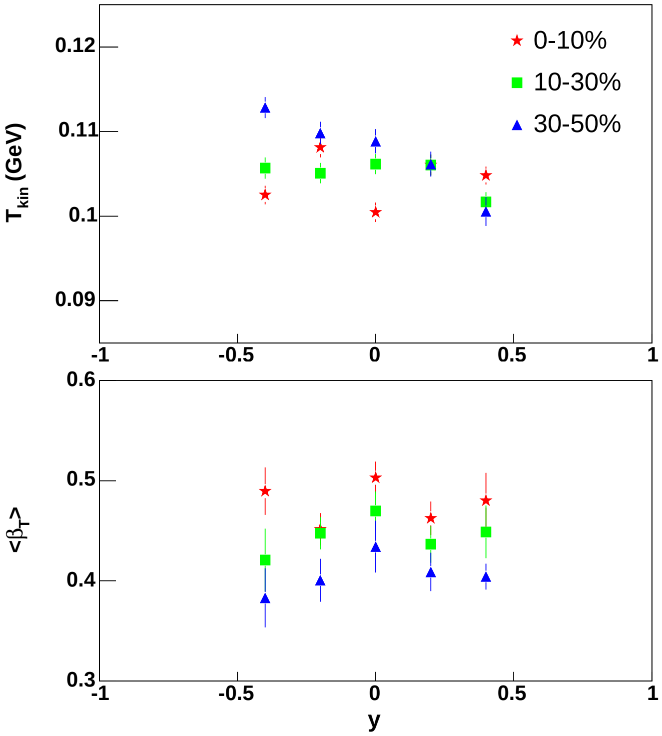

Figure 6.31. Blast wave fit parameters, T_{kin} and $\langle\beta_T\rangle$ as functions of rapidity.

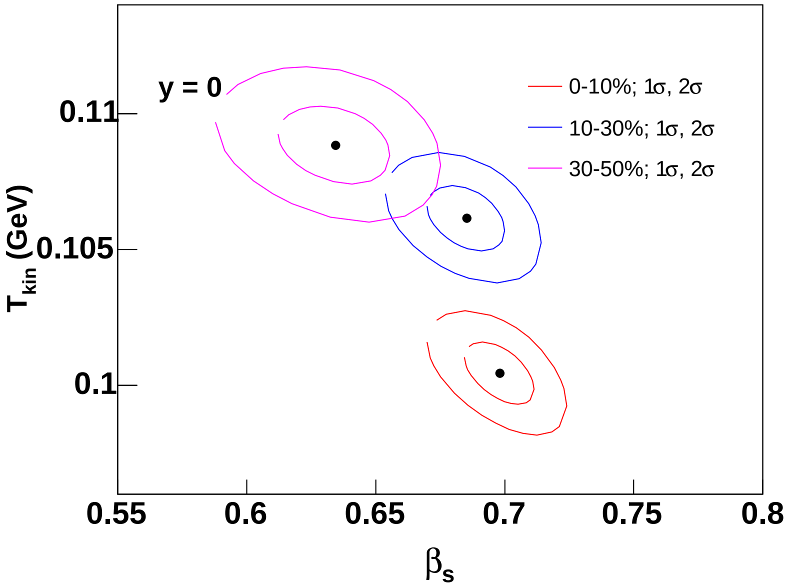

Figure 6.32. 1σ and 2σ contours of β_s and T_{kin} from blast wave fits for midrapidity spectra in three different centrality bins.

6.7.3 Kinetic Freeze-Out Comparison

As we have seen, a temperature and a collective flow velocity are two components which contribute to the shape of the transverse mass spectra. We found that the values from the two expansion models are slightly different. The spherical expansion model gives consistently higher flow velocities and smaller temperatures than the cylindrical model, as seen in Figure 6.33. However, as shown earlier (Figure 6.24, Figure 6.27, Table C.17, and Table C.18) both models fit equally well with our data in the measured rapidity region. The temperature and flow give information about the kinetic freeze-out conditions of the particles. In this section we compare those two parameters with other experiments at different energies.

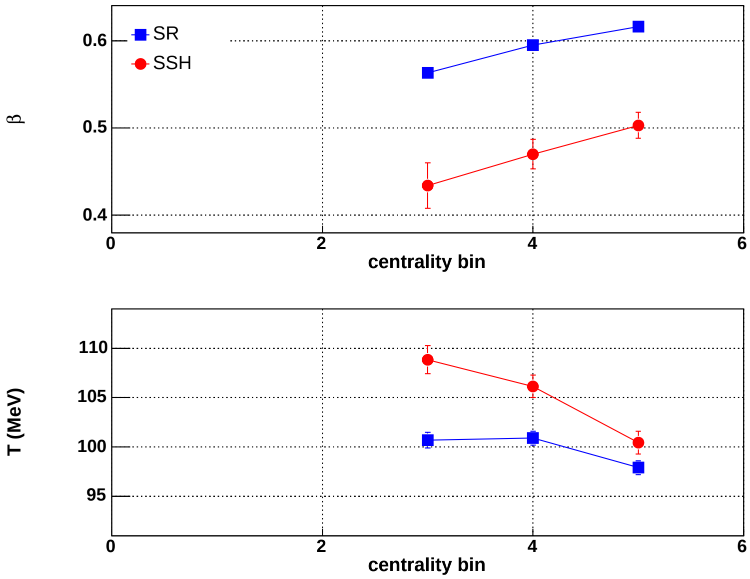

Figure 6.33. The comparison between the kinetic freeze-out parameters from two different model fits, for midrapidity ($|y| < 0.1$) spectra in three different centrality bins. In the figure, the centrality bins from left to right are 30-50%, 10-30%, and 0-10%, respectively. “SR” denotes the Siemens and Rasmussen model and “SSH” represents the Schnedermann, Sollfrank, and Heinz model.

In Figure 6.34, we show our blast-wave results along with other experiments [3]. The results are tabulated in Table C.20. One can see that both T_{kin} and $\langle\beta_T\rangle$ rapidly increase at low energy.

The temperature shows a sign of saturation around the SPS, or even the AGS, energies. The saturation of T_{kin} seems consistent with the notion that the freeze-out temperature has to be colder than the predicted transition temperature (T_{crit}). These plateau structures may suggest that the system is going through a phase transition. At a phase transition of matter, some state observables stay constant, such as the temperature of water while boiling. The flow velocity keeps increasing with the energy. RHIC flow velocity at $\sqrt{s_{\mathrm{NN}}} = 200$ GeV is approximately three times that at the AGS ($\sqrt{s_{\mathrm{NN}}} = 2$ GeV). The strong radial flow indicates that we have a dense system of particles that scatter frequently. Although the fact that T_{kin} and $\langle\beta_T\rangle$ can explain the data is not a sufficient evidence of thermalization, it supports such notion.

---

[3] Aside from the difference in centrality cuts (top 5% for EOS, top 1% for FOPI), EOS analyzed p, d, t, ^3He, and α, while FOPI looked at heavier fragments ($Z \leq 15$). This is probably the reason for the distinct difference between $\langle beta_T\rangle$ between EOS and FOPI.

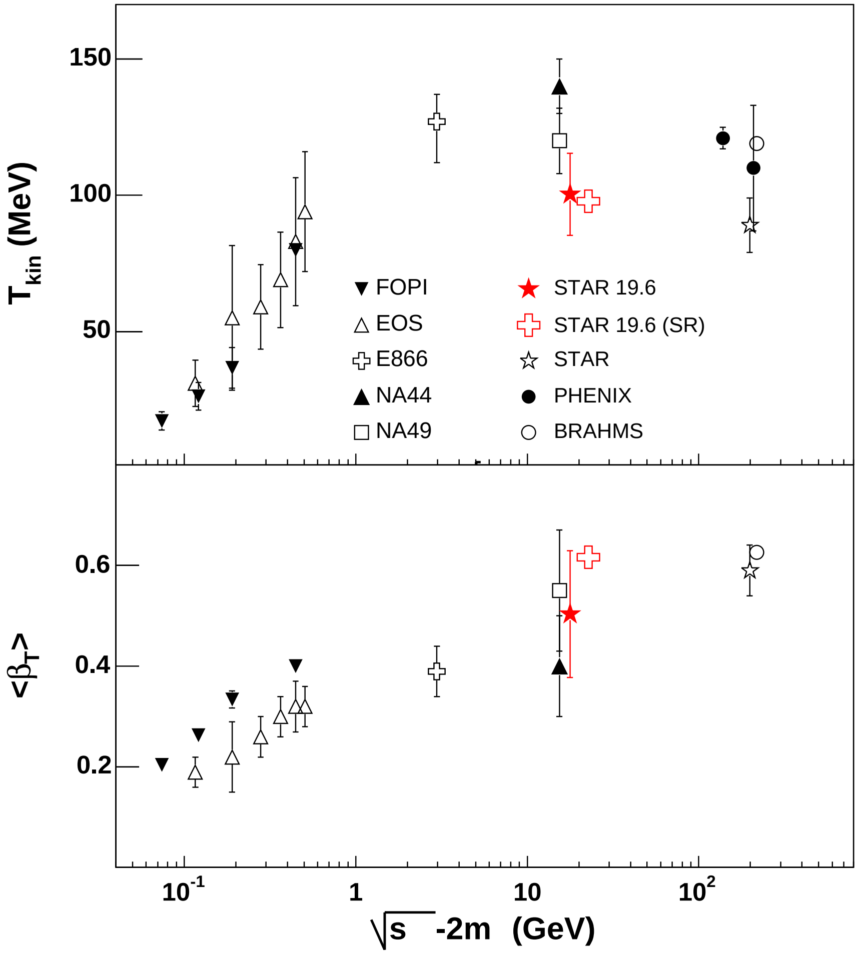

Figure 6.34. Excitation functions of the freeze-out temperature and radial flow velocity. The horizontal axis is $\sqrt{s_{\mathrm{NN}}}$ minus twice the bound nucleon mass. This scaling is meant to show the rise at low energy region more clearly than using simply $\sqrt{s_{\mathrm{NN}}}$ (For clarity, the Siemens-Rasmussen results (labelled SR) are shifted to the right by 5 GeV, and some of the 200 GeV data points are shifted to the right by 10-GeV increments.).

Chapter 7

Conclusion

In this analysis, we have looked at the particle production from the ^{197}Au+^{197}Au collisions at $\sqrt{s_{\mathrm{NN}}} = 19.6$ GeV, measured using the STAR detector during the second run of RHIC. The most abundantly produced hadrons, $\pi^{\pm}$, $K^{\pm}$, p, and $\bar{p}$, produced from the collisions have been analyzed. Their transverse mass distributions have been extracted using dE/dx and momentum in identifying the particles. The centrality and rapidity dependence of yields, particle ratios, and freeze-out conditions have been studied.

Both the statistical and the blast wave models apply well to the transverse mass spectra of the light mesons. For protons and antiprotons, both blast wave frameworks works well in fitting the low-m_T shoulders. This implies that collective motion plays an important role in the momentum distributions of the less energetic particles.

The fits to the spectra give the rapidity density (dN/dy) and the inverse slope parameter. Agreements are observed in the dN/dy comparisons with a slightly lower $\sqrt{s_{\mathrm{NN}}}$ at the SPS. The inverse slope parameter increases with mass–a signature of a collective expansion.

The midrapidity K^-/K^+ ratio is about 0.6 and varies very little among different centrality classes. The midrapidity antiproton yield is approximately 10% that of the protons at this collision energy. Within statistics, the $\bar{p}/p$ ratio is flat as a function of rapidity. It also shows a dependence on the centrality. The π^+/π^- ratio shows a $m_T - m_0$ dependence that quickly increases in low $m_T - m_0$ region and stabilizes as $m_T - m_0$ becomes larger. This behavior can be explained by the Coulomb effect. At midrapidity, $\langle p_T \rangle$ is in the order $p \sim \bar{p} > K^{\pm} > \pi^{\pm}$ and shows centrality dependence.

From the integrated spectra, we calculated the relative yields of various particle species. Using the available set of particle ratios, chemical freeze-out temperature (T_{ch}) came out to be 164.7 MeV and baryon chemical potential (μ_B) is 205.5 MeV. Compared to the results at high energies (130 and 200 GeV Au+Au), T_{ch} at 19.6 GeV is nearly identical to those measurements, while μ_B is much higher, indicating a higher baryon density at lower energy.

The fits to the spectra allow the extraction of kinetic freeze-out conditions of the particles. For the Au+Au collisions, the collective flow, which already existed at the AGS energies, shows up also at $\sqrt{s_{\rm NN}} = 19.6$ GeV, but not as strong as that at 200 GeV. The blast wave model shows that the kinetic freeze-out temperature (T_{kin}) decreases and the flow perpendicular to the beam axis ($\langle \beta_T \rangle$) becomes stronger in the more central collisions. For the most central events, T_{kin} of 100.4 ± 1.1 MeV and $\langle \beta_T \rangle$ of 0.50 ± 0.02 at midrapidity are obtained. Both parameters follow the smooth trends of the respective excitation functions established by other experiments.

The period between the chemical and kinetic freeze-outs is the phase where the emerged hadrons rescatter and some resonances decay into stable hadrons. Having extracted the conditions at both the chemical and kinetic freeze-outs, we draw the following picture of the post-collision dynamics at $\sqrt{s_{\rm NN}} = 19.6$ GeV. Different initial conditions, determined by collision centrality, led to a similar chemical freeze-out temperature, approximately 10 MeV colder than the $T_{\rm c}$ (critical temperature at the phase transition) predicted by lattice QCD. The baryon density seems to increase with centrality. The temperature of the pions, kaons, protons, and antiprotons dropped about 65 MeV before they froze out kinetically.

The STAR measurements in this short 19.6 GeV run complement the results from the higher energy RHIC collisions. Although the number of events is limited, the excellent coverage of the detector allows us to identify the particles and produce a set of well recorded inclusive spectra at midrapidity. The results are generally comparable to the CERN SPS findings, showing consistency between two different experimental setups.

Essentially, we smash the ions at a lower energy to systematically study the energy dependence of various observables. At higher energies, the deconfined state of quarks and gluons is more likely to occur. Still, the lower-energy data are useful to find the point where the transition is "turned on."

Have we discovered the quark gluon plasma? Even at the top RHIC energy, we do not have a definite answer yet. Discoveries come from matching signals. Almost a century ago, Rutherford discovered the nucleus from studying the paths of the alpha particles scattering off the gold foil. From the scattering angle distribution, Rutherford inferred the existence of the concentrated positively-charged nucleus. We eventually want to be able to infer the QGP from the data which come from many-body collisions at extremely high energies. Needless to say, this system is very complex. Before we can claim QGP discovery, we have to match many signals to different theories and models. Currently, there is no single signal which is sufficient. Past and present results have already supported the notion that the QGP has been created, but they are still not as conclusive as the alphas bouncing off the massive nucleus.

In any academic research, it is always crucial to keep in mind why we study what we study. What excites us in learning about the collisions of heavy ions? To me, relativistic heavy ion physics is exciting because of its astrophysical (Big Bang) implications. What we learn from this pursuit can help us understand how the universe originally evolved.

The search for the quark-gluon plasma is the main focus of the quickly developing field of relativistic heavy ion physics. Along the way of the QGP search, the physics community has come up with important and profound knowledge of strongly interacting nuclear matter at extreme conditions, and yet there is still much more to discover and understand. RHIC has expanded the range in which the nuclear matter can be studied, paving the way for the LHC to further explore the TeV scale in the near future.

Appendix A

Kinematics

In this appendix, various quantities related to the motions of the particles in nuclear collisions will be described.

Rapidity is a variable associated with energy and momentum of a particle. It is defined as

$$\begin{aligned} y &= \frac{1}{2}\ln\left(\frac{E+p_{\text{long}}}{E-p_{\text{long}}}\right) \\ &= \frac{1}{2}\ln\left(\frac{1+\beta_{\text{long}}}{1-\beta_{\text{long}}}\right) \\ &= \tanh^{-1}\beta_{\text{long}} \qquad \text{(A.1)} \end{aligned}$$

where E is the energy, p_{long} is the momentum along the longitudinal (beam or z) direction, and β_{long} $(= p_{\text{long}}/E)$ is the longitudinal velocity.

Rapidity is a useful variable in relativistic systems as it is additive under successive Lorentz transformations along the same direction. That is, let us say we have a reference frame F, and in that frame, a particle is moving with rapidity y_p. Then there is another reference frame F' moving, in the same direction as the particle, with a velocity $\beta_{F'}$ with respect to F. An observer at rest in F' will see the particle moving with a rapidity, conveniently, $y' = y_p + y_{F'}$, where $y_{F'}$ can be calculated from $\beta_{F'}$ from the definition in equation (A.1).

A particle whose total momentum is completely perpendicular to the beam will have $y = 0$. These nearly midrapidity particles are the primary focus of this study.

Pseudorapidity (η) is a variable related to the direction of the particle trajectory. η is defined as

$$\begin{aligned} \eta &= -\ln\left(\tan\frac{\theta}{2}\right) \\ &= \frac{1}{2}\ln\left(\frac{p+p_{\mathrm{long}}}{p-p_{\mathrm{long}}}\right) \end{aligned} \tag{A.2}$$

where θ is the polar angle between the particle's trajectory and the beam axis. Both the θ and ϕ angles are measured for the tangent of the track at the point of distance of closest approach to the primary vertex. The pseudorapidity is related to rapidity by

$$p\tanh\eta = E\tanh y \tag{A.3}$$

Therefore, for a massless particle such as photons, $\eta = y$. This equality is also applicable for highly relativistic ($\beta \rightarrow 1$) particles.

The quantity transverse mass (m_T) is defined as

$$m_T \equiv \sqrt{p_T^2 + m_0^2} \tag{A.4}$$

where p_T ($= \sqrt{{p_x}^2 + {p_y}^2}$) is the transverse momentum and m_0 is the rest mass of the particle. Under longitudinal boosts, both p_T and m_T stay constant.

The term "transverse mass" is sometimes used interchangebly with the quantity $m_T - m_0$. Energy can be expressed in terms of transverse mass and rapidity as $E = m_T\cosh y$. For a particle traveling at midrapidity ($y = 0$), it carries the total energy, $E = m_T\cosh(0) = m_T$. Thus $m_T - m_0$ represents the kinetic energy of the particle.

Appendix B

Blast Wave Contour Plots

These are the contour plots of β_s and T_{kin} from the blast wave model fits from Section 6.7.2.

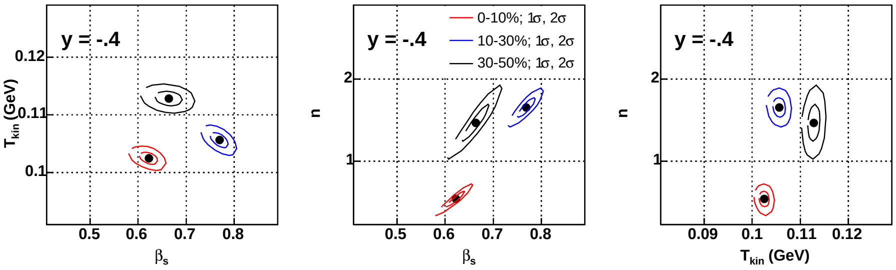

Figure B.1. Contour plots of the blast wave parameters, β_s, T_{kin}, and n extracted from fitting the spectra. Three centrality classes. Rapidity $-0.5 < y < -0.3$.

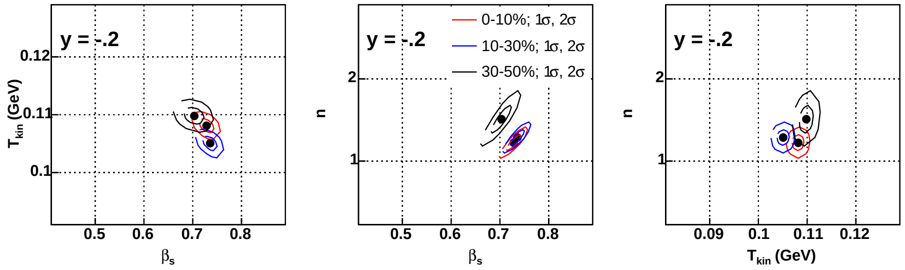

Figure B.2. Contour plots of the blast wave parameters, β_s, T_{kin}, and n extracted from fitting the spectra. Three centrality classes. Rapidity $-0.3 < y < -0.1$.

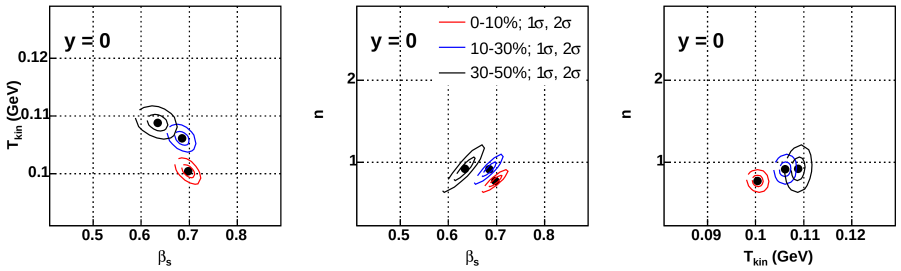

Figure B.3. Contour plots of the blast wave parameters, β_s, T_{kin}, and n extracted from fitting the spectra. Three centrality classes. Rapidity $-0.1 < y < 0.1$.

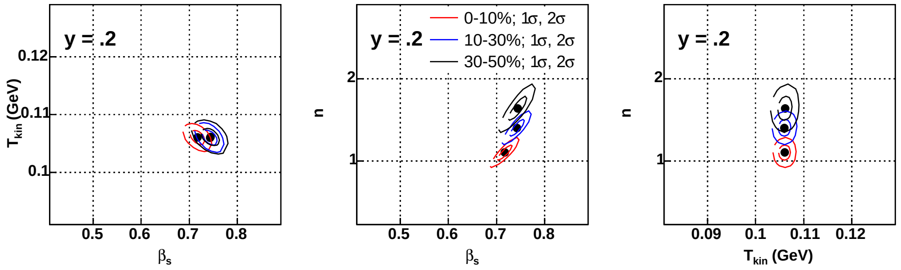

Figure B.4. Contour plots of the blast wave parameters, β_s, T_{kin}, and n extracted from fitting the spectra. Three centrality classes. Rapidity $0.1 < y < 0.3$.

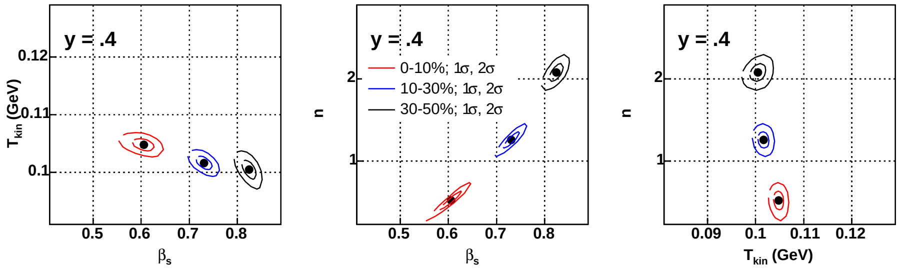

Figure B.5. Contour plots of the blast wave parameters, β_s, T_{kin}, and n extracted from fitting the spectra. Three centrality classes. Rapidity $0.3 < y < 0.5$.

Appendix C

Data Tables

top 10% central				
$m_T - m_0$	π^+		π^-	
(GeV/c^2)	yield	error	yield	error
0.1125	223.442	3.2369	240.082	3.33935
0.1375	199.973	2.65323	206.961	2.70775
0.1625	169.292	2.29575	181.421	2.35064
0.1875	147.271	2.03421	155.405	2.08954
0.2125	123.821	1.78944	124.951	1.79711
0.2375	104.442	1.58905	111.759	1.65008
0.2625	88.7085	1.42437	95.1115	1.45634
0.2875	79.4957	1.29685	82.6223	1.3106
0.3125	68.2889	1.16619	68.8973	1.16805
0.3375	59.9969	1.06188	61.8593	1.0785
0.3625	51.6967	0.963701	51.9613	0.962368
0.3875	46.7883	0.854021	46.8438	0.88521
0.4125	39.9422	0.803099	41.0429	0.818734
0.4375	35.7681	0.743265	36.5732	0.751508
0.4625	30.984	0.680547	31.4649	0.675652
0.4875	27.1029	0.625167	26.4482	0.615363
0.5125	24.54	0.57861	23.8427	0.579993
0.5375	20.7231	0.533543	21.2333	0.54472
0.5625	17.8433	0.491819	18.71	0.50064
0.5875	15.7236	0.461235	16.4974	0.47384
0.6125	14.2446	0.44122	14.8286	0.440962
0.6375	12.687	0.41834	12.2975	0.406199
0.6625	11.3166	0.384919	10.8283	0.382722
0.6875	10.8896	0.399045	9.64339	0.369303
0.7125	8.87182	0.375405	8.56324	0.36427
0.7375	8.20303	0.372782	8.18897	0.356622
0.7625	6.02408	0.355186	6.13361	0.337571
0.7875	5.47721	0.381189	5.70654	0.355237
0.8125	4.19475	0.377263	5.16	0.382175
0.8375	4.81972	0.408639	4.3935	0.404963
0.8625	3.6738	0.464314	3.64896	0.418821

Table C.1. Charged pion invariant yields $\left(\dfrac{d^2N}{2\pi m_T\, dm_T\, dy}\right)$ for the top 10% central events at midrapidity $-0.1 < y < 0.1$.

top 10% central				
$m_T - m_0$	K^+		K^-	
(GeV/c^2)	yield	error	yield	error
0.0625	19.6735	0.971331	13.6075	0.794786
0.0875	17.4111	0.748575	10.5953	0.57634
0.1125	14.7906	0.625375	9.62267	0.503299
0.1375	13.2864	0.559964	8.23381	0.443189
0.1625	12.3107	0.53472	7.40303	0.425749
0.1875	11.1306	0.531702	6.7048	0.440935
0.2875	7.26555	0.504215	4.71815	0.368777
0.3125	6.90667	0.387189	4.58697	0.325762
0.3375	7.33981	0.37513	3.71467	0.290068
0.3625	5.80225	0.34185	3.38514	0.275495
0.3875	5.05631	0.330628	3.75205	0.289055
0.4125	4.557	0.322543	2.66286	0.266419
0.4375	4.64899	0.345231	2.92468	0.287566
0.4625	4.00072	0.345896	2.64681	0.295209
0.4875	3.92532	0.36026	2.076	0.303219
0.5125	3.13775	0.365159	1.85193	0.298665

Table C.2. Charged kaon invariant yields $\left(\dfrac{d^2N}{2\pi m_T\, dm_T\, dy}\right)$ for the top 10% central events at midrapidity $-0.1 < y < 0.1$.

top 10% central				
$m_T - m_0$	p		$\bar{p}$	
(GeV/c^2)	yield	error	yield	error
0.0625	8.55341	0.322937	0.541247	0.07378
0.0875	7.87394	0.285219	0.784692	0.0819785
0.1125	8.61069	0.275109	0.701635	0.0783982
0.1375	8.64244	0.264537	0.770616	0.0804073
0.1625	8.08897	0.252041	0.864517	0.0822125
0.1875	7.83833	0.240338	0.857129	0.0812376
0.2125	7.49471	0.238697	0.716719	0.0776644
0.2375	6.90081	0.222455	0.669043	0.0654915
0.2625	6.66856	0.216504	0.644263	0.0694051
0.2875	5.47801	0.195397	0.451221	0.0619555
0.3125	5.90728	0.205309	0.434928	0.0608046
0.3375	4.88579	0.200935	0.454232	0.0704872
0.3625	4.71294	0.173885	0.241883	0.0791322
0.3875	4.66191	0.168386	0.504824	0.0600496
0.4875	2.83161	0.135588	0.280127	0.0459878
0.5125	3.13545	0.164532	0.223383	0.0703871
0.5375	2.67066	0.145929	0.302242	0.0639974
0.5625	2.33746	0.129653	0.248726	0.0557762
0.5875	2.17933	0.125842	0.220488	0.0547833
0.6125	2.091796	0.123482	0.202914	0.0501257
0.6375	1.67039	0.110958	0.237971	0.0574178
0.6625	1.81867	0.116242	0.160891	0.0527834
0.6875	1.33671	0.110095	0.139347	0.0532405
0.7125	1.44527	0.112478	0.155555	0.0533541
0.7375	1.50743	0.119908	0.135386	0.0551053
0.7625	1.00925	0.108612	0.157626	0.0682053
0.7875	0.990054	0.107079	0.17247	0.0737974

Table C.3. Proton and antiproton invariant yields $\left(\dfrac{d^2N}{2\pi m_T\, dm_T\, dy}\right)$ for the top 10% central events at midrapidity $-0.1 < y < 0.1$.

10-30% central				
$m_T - m_0$	π^+		π^-	
(GeV/c^2)	yield	error	yield	error
0.1125	135.71	1.83415	131.061	1.92823
0.1375	116.084	1.53921	119.398	1.5762
0.1625	98.1886	1.33216	102.283	1.36949
0.1875	84.6434	1.18085	87.2122	1.19045
0.2125	71.7984	1.04525	74.5105	1.06675
0.2375	62.2735	0.937241	63.4496	0.946802
0.2625	53.2512	0.839052	54.9376	0.853537
0.2875	46.9537	0.763248	47.9687	0.772256
0.3125	39.2686	0.676544	41.0992	0.695499
0.3375	34.4967	0.623583	36.9721	0.636152
0.3625	30.2437	0.565689	30.9764	0.570574
0.3875	26.2012	0.513297	27.3139	0.517288
0.4125	22.8344	0.46878	23.4657	0.472105
0.4375	19.4991	0.421495	20.7759	0.435966
0.4625	17.1297	0.389414	17.6914	0.392479
0.4875	14.7961	0.355871	15.2461	0.35726
0.5125	13.6489	0.336632	14.1973	0.342219
0.5375	12.0676	0.312323	12.2558	0.315413
0.5625	10.4437	0.289142	10.9693	0.296503
0.5875	9.22835	0.271854	9.18711	0.271441
0.6125	8.19435	0.257993	8.41431	0.262415
0.6375	7.63254	0.249938	7.43589	0.246169
0.6625	6.61722	0.229678	6.2891	0.229944
0.6875	5.73832	0.220955	5.84682	0.222588
0.7125	5.45607	0.229529	5.27734	0.22246
0.7375	4.33162	0.214541	4.4396	0.221331
0.7625	3.8548	0.217089	4.26586	0.206399
0.7875	2.82726	0.218124	3.84089	0.217343
0.8125	3.37823	0.235706	2.91785	0.216725
0.8375	2.66862	0.24846	3.02632	0.248683
0.8625	2.13685	0.282912	2.15068	0.259194

Table C.4. Charged pion invariant yields $\left(\dfrac{d^2N}{2\pi m_T\, dm_T\, dy}\right)$ for the 10-30% central events at midrapidity $-0.1 < y < 0.1$.

10-30% central				
$m_T - m_0$	K^+		K^-	
(GeV/c^2)	yield	error	yield	error
0.0625	11.7212	0.572675	6.97396	0.480299
0.0875	10.1151	0.445972	5.95769	0.345289
0.1125	8.21357	0.364271	5.54588	0.303603
0.1375	6.84395	0.315212	5.4851	0.280995
0.1625	7.35815	0.323788	4.43961	0.251925
0.1875	5.92739	0.324611	3.9194	0.264141
0.2875	4.15297	0.238155	3.23226	0.177701
0.3125	3.72972	0.215105	2.37667	0.181308
0.3375	3.21873	0.195451	2.27067	0.165703
0.3625	2.65918	0.181009	1.97924	0.15886
0.3875	2.73109	0.186845	1.66177	0.155242
0.4125	2.01184	0.174185	1.60304	0.15823
0.4375	1.8754	0.174535	1.51215	0.158799
0.4625	1.71329	0.176991	1.22682	0.144667
0.4875	1.61572	0.198896	1.20257	0.174782
0.5125	1.74995	0.216864	0.971211	0.177129

Table C.5. Charged kaon invariant yields $\left(\dfrac{d^2N}{2\pi m_T\, dm_T\, dy}\right)$ for the 10-30% central events at midrapidity $-0.1 < y < 0.1$.

10-30% central				
$m_T - m_0$	p		$\bar{p}$	
(GeV/c^2)	yield	error	yield	error
0.0625	5.16627	0.201663	0.627868	0.063393
0.0875	4.9586	0.18225	0.574225	0.0558519
0.1125	5.00059	0.166495	0.499356	0.0502295
0.1375	4.86039	0.158817	0.529639	0.051068
0.1625	4.7037	0.152147	0.394224	0.0450392
0.1875	4.29477	0.142948	0.546909	0.0530607
0.2125	3.86902	0.132494	0.520443	0.0486269
0.2375	3.82503	0.12831	0.473656	0.04662
0.2625	3.49253	0.124747	0.351954	0.0399944
0.2875	3.45433	0.122221	0.460444	0.0474834
0.3125	3.18343	0.117478	0.324476	0.0431098
0.3375	2.97695	0.120726	0.382244	0.0489522
0.3625	2.8853	0.105404	0.322809	0.0535089
0.3875	2.41824	0.0952145	0.308823	0.0352072
0.4875	1.62026	0.113383	0.112831	0.0432074
0.5125	1.63203	0.0948454	0.165449	0.0433399
0.5375	1.3781	0.0833888	0.10051	0.0256228
0.5625	1.16512	0.0735442	0.194395	0.0376157
0.5875	1.20796	0.0749207	0.0680648	0.0285377
0.6125	1.07842	0.0718641	0.097757	0.0300574
0.6375	1.08162	0.0660254	0.0792121	0.0284569
0.6625	1.02583	0.0683514	0.105922	0.0316045
0.6875	0.736135	0.0592601	0.101152	0.0345947
0.7125	0.784987	0.0672785	0.0326564	0.0359324
0.7375	0.681945	0.0590177	0.045541	0.036592
0.7625	0.581665	0.0681957	0.0880555	0.0358536
0.7875	0.466499	0.0554061	0.0638923	0.0411701

Table C.6. Proton and antiproton invariant yields $\left(\dfrac{d^2N}{2\pi m_T\, dm_T\, dy}\right)$ for the 10-30% central events at midrapidity $-0.1 < y < 0.1$.

30-50% central				
$m_T - m_0$	π^+		π^-	
(GeV/c^2)	yield	error	yield	error
0.1125	58.9525	1.00119	61.4042	1.00689
0.1375	51.9854	0.820713	55.2448	0.845542
0.1625	43.5009	0.706593	46.9389	0.72878
0.1875	37.7298	0.628513	38.7684	0.635677
0.2125	31.3218	0.549276	33.3031	0.563724
0.2375	28.2727	0.503718	28.4898	0.500601
0.2625	24.0171	0.44908	23.5525	0.44367
0.2875	20.4363	0.401858	21.1245	0.405561
0.3125	17.5391	0.360702	17.7936	0.36578
0.3375	14.9466	0.328005	15.1263	0.321819
0.3625	12.8186	0.292575	12.885	0.293284
0.3875	11.405	0.265932	11.9999	0.277055
0.4125	9.29472	0.237873	9.95484	0.24587
0.4375	8.83708	0.227552	8.57472	0.223124
0.4625	7.87597	0.209877	7.40814	0.2016
0.4875	6.65075	0.193725	6.20175	0.183195
0.5125	5.5519	0.170387	5.7716	0.174298
0.5375	5.1104	0.161159	5.10182	0.162982
0.5625	4.6771	0.153536	4.50191	0.14988
0.5875	3.87487	0.13702	4.08729	0.141068
0.6125	3.38894	0.129002	3.4228	0.127062
0.6375	3.04368	0.121632	2.86962	0.11865
0.6625	2.97095	0.12157	2.70148	0.113454
0.6875	2.36188	0.112487	2.36833	0.107681
0.7125	2.04414	0.109154	2.15701	0.107982
0.7375	1.81819	0.105931	1.79652	0.102106
0.7625	1.23136	0.0975863	1.67333	0.103925
0.7875	1.23773	0.105992	0.964821	0.0877972
0.8125	1.3118	0.11212	1.23563	0.100941
0.8375	0.968224	0.115344	1.01069	0.112144
0.8625	0.843219	0.12368	0.908195	0.124887

Table C.7. Charged pion invariant yields $\left(\dfrac{d^2N}{2\pi m_T\, dm_T\, dy}\right)$ for the 30-50% central events at midrapidity $-0.1 < y < 0.1$.

30-50% central				
$m_T - m_0$ (GeV/c^2)	K^+		K^-	
	yield	error	yield	error
0.0625	5.34563	0.316389	2.86259	0.23177
0.0875	4.40585	0.243335	2.57164	0.186717
0.1125	3.59274	0.199357	2.59612	0.167491
0.1375	3.47937	0.181534	2.18534	0.149803
0.1625	3.06595	0.169792	2.01903	0.134767
0.1875	2.53734	0.167573	1.81174	0.140742
0.2875	1.66424	0.127632	0.999653	0.113699
0.3125	1.58272	0.109307	1.10488	0.0977269
0.3375	1.42624	0.101586	0.885204	0.0842659
0.3625	1.05566	0.0905811	0.681818	0.0728179
0.3875	1.34178	0.100205	0.756597	0.0792474
0.4125	0.845884	0.0837576	0.674028	0.0785035
0.4375	0.645222	0.0832527	0.495956	0.0743872
0.4625	0.634553	0.0886282	0.395185	0.0745078
0.4875	0.895935	0.103659	0.65195	0.094474
0.5125	0.741393	0.105724	0.272328	0.0805361

Table C.8. Charged kaon invariant yields $\left(\dfrac{d^2N}{2\pi m_T\, dm_T\, dy}\right)$ for the 30-50% central events at midrapidity $-0.1 < y < 0.1$.

30-50% central				
$m_T - m_0$	p		$\bar{p}$	
(GeV/c^2)	yield	error	yield	error
0.0625	2.41814	0.122438	0.346438	0.0400002
0.0875	2.11659	0.0981973	0.321342	0.0359983
0.1125	2.3597	0.0922911	0.23815	0.0286969
0.1375	2.07553	0.0818216	0.300646	0.0321933
0.1625	2.15099	0.0818915	0.262604	0.030027
0.1875	1.9332	0.0751056	0.241279	0.0289497
0.2125	1.83279	0.0715468	0.203496	0.024437
0.2375	1.74425	0.0683423	0.271793	0.0292411
0.2625	1.40061	0.0602773	0.190878	0.024271
0.2875	1.46733	0.0612833	0.154598	0.0209747
0.3125	1.27777	0.0574377	0.185749	0.0239068
0.3375	1.20515	0.057085	0.122875	0.0231992
0.3625	1.09079	0.0512651	0.0852309	0.0269711
0.3875	0.876579	0.0623529	0.0985719	0.0407377
0.4875	0.660498	0.0374884	0.0786342	0.0263388
0.5125	0.565898	0.0573433	0.0368671	0.0212349
0.5375	0.508527	0.0440981	0.0543272	0.0196679
0.5625	0.440028	0.0397938	0.0584171	0.0161044
0.5875	0.446275	0.0372105	0.0548032	0.0180171
0.6125	0.431542	0.0351873	0.0695622	0.0186038
0.6375	0.317785	0.029975	0.0467091	0.0157664
0.6625	0.292754	0.0274503	0.0450557	0.0173071
0.6875	0.270287	0.0289819	0.0535084	0.0183363
0.7125	0.281755	0.0285584	0.0206697	0.0191548
0.7375	0.177877	0.0250559	0.0293232	0.0157733
0.7625	0.166612	0.0275325	0.0434592	0.0165511
0.7875	0.171695	0.0267582	0.0229235	0.0196572

Table C.9. Proton and antiproton invariant yields $\left(\dfrac{d^2N}{2\pi m_T\, dm_T\, dy}\right)$ for the 30-50% central events at midrapidity $-0.1 < y < 0.1$.

	π^+	π^-
$0-10\%$	0.181885 ± 0.000802564	0.177779 ± 0.000754993
$10-30\%$	0.179356 ± 0.00079868	0.180427 ± 0.000785571
$30-50\%$	0.17545 ± 0.000908642	0.171566 ± 0.00086171
$50-70\%$	0.164493 ± 0.00128545	0.165905 ± 0.00125957
$70-100\%$	0.171911 ± 0.00563811	0.159375 ± 0.00548098
	K^+	K^-
$0-10\%$	0.261314 ± 0.00724888	0.251832 ± 0.00905137
$10-30\%$	0.223254 ± 0.00566986	0.241724 ± 0.00823833
$30-50\%$	0.211983 ± 0.00639128	0.214152 ± 0.0084023
$50-70\%$	0.173471 ± 0.00837778	0.171283 ± 0.0118419
	p	$\bar{p}$
$0-10\%$	0.305229 ± 0.00566806	0.413802 ± 0.0265831
$10-30\%$	0.29169 ± 0.00525424	0.324412 ± 0.017509
$30-50\%$	0.256214 ± 0.00513952	0.281676 ± 0.0174853

Table C.10. The inverse slope parameters from Maxwell-Boltzmann fits to $m_T - m_0$ spectra for various centrality bins at midrapidity ($|y| < 0.1$).

centrality	particle	dN/dy				
		$y = -0.4$	$y = -0.2$	$y = 0.0$	$y = 0.2$	$y = 0.4$
0-10%	π^+	141.41 ± 1.75	147.00 ± 1.83	144.04 ± 1.83	148.27 ± 1.89	142.01 ± 1.70
	π^-	147.58 ± 1.81	152.26 ± 1.89	148.89 ± 1.88	152.87 ± 1.94	149.10 ± 1.78
	K^+	22.87 ± 1.13	24.50 ± 0.94	26.73 ± 1.05	24.54 ± 0.97	23.69 ± 1.19
	K^-	14.85 ± 0.90	14.32 ± 0.68	16.36 ± 0.79	15.15 ± 0.73	13.82 ± 0.87
	p	33.97 ± 1.45	33.84 ± 1.45	32.43 ± 1.48	33.54 ± 1.49	33.60 ± 1.40
	$\bar{p}$	2.75 ± 0.30	2.75 ± 0.27	3.08 ± 0.24	2.51 ± 0.26	2.64 ± 0.33
10-30%	π^+	81.78 ± 1.07	84.03 ± 1.04	83.47 ± 1.04	84.31 ± 1.12	83.56 ± 1.07
	π^-	84.81 ± 1.10	86.52 ± 1.06	85.80 ± 1.06	87.87 ± 1.17	86.05 ± 1.10
	K^+	13.81 ± 0.65	13.73 ± 0.55	13.73 ± 0.53	14.46 ± 0.59	14.19 ± 0.68
	K^-	8.19 ± 0.51	8.83 ± 0.43	9.29 ± 0.43	8.63 ± 0.44	8.54 ± 0.52
	p	19.14 ± 0.90	19.05 ± 0.84	18.74 ± 0.83	19.14 ± 0.90	19.53 ± 0.88
	$\bar{p}$	1.51 ± 0.21	1.74 ± 0.16	1.94 ± 0.15	1.62 ± 0.17	1.58 ± 0.24
30-50%	π^+	36.14 ± 0.48	36.29 ± 0.52	36.50 ± 0.53	36.89 ± 0.56	36.66 ± 0.63
	π^-	38.09 ± 0.50	37.41 ± 0.53	37.41 ± 0.55	38.23 ± 0.58	38.01 ± 0.66
	K^+	5.53 ± 0.31	5.48 ± 0.27	5.77 ± 0.27	5.98 ± 0.29	5.79 ± 0.35
	K^-	3.06 ± 0.22	3.49 ± 0.21	3.68 ± 0.21	3.68 ± 0.22	3.33 ± 0.26
	p	7.84 ± 0.37	7.43 ± 0.38	7.32 ± 0.39	7.39 ± 0.41	7.96 ± 0.51
	$\bar{p}$	0.83 ± 0.10	0.84 ± 0.09	0.88 ± 0.09	0.86 ± 0.09	0.76 ± 0.13
50-70%	π^+	13.28 ± 0.23	13.64 ± 0.24	13.45 ± 0.23	13.90 ± 0.24	13.30 ± 0.22
	π^-	13.54 ± 0.23	13.99 ± 0.24	13.68 ± 0.23	14.22 ± 0.25	13.85 ± 0.22
	K^+	1.45 ± 0.26	1.59 ± 0.25	1.64 ± 0.23	1.89 ± 0.27	1.46 ± 0.32
	K^-	0.89 ± 0.25	1.13 ± 0.22	1.08 ± 0.23	1.17 ± 0.21	1.02 ± 0.26
70-100%	π^+	3.34 ± 0.20	3.29 ± 0.22	3.22 ± 0.22	3.51 ± 0.24	3.68 ± 0.22
	π^-	3.44 ± 0.21	3.19 ± 0.22	3.21 ± 0.24	3.58 ± 0.24	3.70 ± 0.22

Table C.11. Rapidity density of the particles.

centrality	particle	$\langle p_T \rangle$				
		$y = -0.4$	$y = -0.2$	$y = 0.0$	$y = 0.2$	$y = 0.4$
0-10%	π^+	0.38 ± 0.00	0.39 ± 0.00	0.39 ± 0.00	0.39 ± 0.00	0.38 ± 0.00
	π^-	0.37 ± 0.00	0.39 ± 0.00	0.38 ± 0.00	0.39 ± 0.00	0.37 ± 0.00
	K^+	0.58 ± 0.03	0.57 ± 0.02	0.62 ± 0.02	0.57 ± 0.02	0.58 ± 0.03
	K^-	0.55 ± 0.03	0.57 ± 0.03	0.61 ± 0.03	0.57 ± 0.03	0.56 ± 0.03
	p	0.83 ± 0.04	0.84 ± 0.04	0.86 ± 0.04	0.85 ± 0.04	0.82 ± 0.03
	$\bar{p}$	0.82 ± 0.09	0.84 ± 0.08	0.97 ± 0.08	0.86 ± 0.09	0.82 ± 0.10
10-30%	π^+	0.38 ± 0.00	0.38 ± 0.00	0.39 ± 0.00	0.38 ± 0.01	0.37 ± 0.00
	π^-	0.38 ± 0.00	0.38 ± 0.00	0.39 ± 0.00	0.38 ± 0.01	0.37 ± 0.00
	K^+	0.56 ± 0.03	0.57 ± 0.02	0.57 ± 0.02	0.57 ± 0.02	0.57 ± 0.03
	K^-	0.54 ± 0.03	0.58 ± 0.03	0.59 ± 0.03	0.58 ± 0.03	0.57 ± 0.03
	p	0.80 ± 0.04	0.83 ± 0.04	0.83 ± 0.04	0.83 ± 0.04	0.81 ± 0.04
	$\bar{p}$	0.79 ± 0.11	0.81 ± 0.07	0.86 ± 0.07	0.78 ± 0.08	0.80 ± 0.12
30-50%	π^+	0.37 ± 0.00	0.38 ± 0.01	0.37 ± 0.01	0.37 ± 0.01	0.37 ± 0.01
	π^-	0.37 ± 0.00	0.37 ± 0.01	0.37 ± 0.01	0.37 ± 0.01	0.37 ± 0.01
	K^+	0.52 ± 0.03	0.56 ± 0.03	0.55 ± 0.03	0.56 ± 0.03	0.55 ± 0.03
	K^-	0.51 ± 0.04	0.54 ± 0.03	0.55 ± 0.03	0.55 ± 0.03	0.51 ± 0.04
	p	0.74 ± 0.03	0.77 ± 0.04	0.77 ± 0.04	0.78 ± 0.04	0.80 ± 0.05
	$\bar{p}$	0.74 ± 0.09	0.73 ± 0.08	0.79 ± 0.08	0.77 ± 0.08	0.77 ± 0.13
50-70%	π^+	0.35 ± 0.01	0.36 ± 0.01	0.35 ± 0.01	0.35 ± 0.01	0.35 ± 0.01
	π^-	0.35 ± 0.01	0.35 ± 0.01	0.35 ± 0.01	0.35 ± 0.01	0.35 ± 0.01
	K^+	0.46 ± 0.08	0.49 ± 0.08	0.48 ± 0.07	0.51 ± 0.07	0.51 ± 0.11
	K^-	0.43 ± 0.12	0.45 ± 0.09	0.47 ± 0.10	0.49 ± 0.09	0.41 ± 0.10
70-100%	π^+	0.35 ± 0.02	0.36 ± 0.02	0.37 ± 0.03	0.35 ± 0.02	0.35 ± 0.02
	π^-	0.34 ± 0.02	0.36 ± 0.02	0.34 ± 0.03	0.34 ± 0.02	0.36 ± 0.02

Table C.12. Mean transverse momentum for particles with $|y| < 0.1$.

centrality	$dN_{\text{ch}}/d\eta$				
	$y = -0.4$	$y = -0.2$	$y = 0.0$	$y = +0.2$	$y = +0.4$
0-10%	313.1 ± 3.8	316.7 ± 4.1	311.1 ± 4.1	318.5 ± 4.1	314.4 ± 3.8
10-30%	180.0 ± 2.5	180.3 ± 2.3	178.0 ± 2.2	182.0 ± 2.4	183.5 ± 2.3
30-50%	78.6 ± 0.9	76.4 ± 1.0	76.2 ± 1.0	78.2 ± 1.1	79.5 ± 1.4

Table C.13. $dN_{\text{ch}}/d\eta$ of charged hadrons, calculated from yields of $\pi^{\pm}$, $K^{\pm}$, p, and $\bar{p}$.

species	data ($\lvert y\rvert < 0.5$)	model
π^+/π^-	0.9608 ± 0.0146	1.0
K^-/K^+	0.6054 ± 0.0063	0.6054
$\bar{p}/p$	0.08242 ± 0.00004	0.08242
K^-/π^-	0.0980 ± 0.0012	0.980
$\bar{p}/\pi^-$	0.0173 ± 0.0002	0.0173

Table C.14. Particle ratios from the data versus from statistical model calculations.

centrality	T_{ch} (MeV)	μ_q (MeV)	μ_s (MeV)	γ_s
0-10%	164.7 ± 0.5	68.5 ± 0.2	27.2 ± 0.9	0.58 ± 0.01
10-30%	167.3 ± 0.9	66.8 ± 1.0	26.8 ± 1.3	0.58 ± 0.01
30-50%	168.2 ± 0.9	60.6 ± 0.9	18.8 ± 1.1	0.53 ± 0.01

Table C.15. Chemical freeze-out parameters from the statistical model fit for three centrality bins.

experiment	$\sqrt{s_{\mathrm{NN}}}$ (GeV)	μ_B (MeV)	T_{ch} (MeV)	reference
SIS	2.31	825 ± 8	49 ± 3	[187]
AGS	4.8	540 ± 7	125^{+3}_{-6}	[185]
SPS	8.83	410 ± 30	143 ± 5	[208]
SPS	17.3	255 ± 10	170 ± 5	[209]
STAR	19.6	206 ± 1	164.7 ± 0.5	(this work)
RHIC	130	46 ± 5	174 ± 7	[209]
RHIC	200	29 ± 6	177 ± 7	[209]

Table C.16. Collected data on baryon chemical potentials and chemical freeze-out temperatures from various experiments. The facility names are used here because the particle ratios were compiled across experiments at same energies.

centrality	T (MeV)	β	χ^2/d.o.f.
0-10%	97.9 ± 0.7	0.616 ± 0.004	263.9/147
10-30%	100.9 ± 0.7	0.595 ± 0.004	229.1/144
30-50%	100.7 ± 0.008	0.563 ± 0.006	243.0/141

Table C.17. Fit parameters from the Siemens and Rasmussen spherical expansion model fit to midrapidity ($|y| < 0.1$) data.

centrality	T_{kin} (MeV)	β_s	n	$\langle\beta_T\rangle$	χ^2/d.o.f.
0-10%	100.44 ± 1.14	0.698 ± 0.014	0.78 ± 0.07	0.503 ± 0.015	279.9/146
10-30%	106.14 ± 1.20	0.685 ± 0.015	0.92 ± 0.09	0.470 ± 0.017	240.3/143
30-50%	108.84 ± 1.44	0.634 ± 0.022	0.92 ± 0.14	0.434 ± 0.026	239.0/140

Table C.18. Blast wave (Schnedermann, Sollfrank, and Heinz) fit parameters for midrapidity ($|y| < 0.1$) data from three centrality bins.

fixed n	T_{kin} (MeV)	$\langle\beta_{\mathrm{T}}\rangle$
0.5	101.26 ± 1.08	0.516 ± 0.005
1.0	100.53 ± 1.26	0.488 ± 0.005
1.5	103.77 ± 1.22	0.447 ± 0.004
2.0	109.42 ± 1.14	0.403 ± 0.004
2.5	114.78 ± 1.03	0.365 ± 0.003

Table C.19. Values of the kinetic freeze-out temperature and the average transverse flow velocity extracted from the blast wave (Schnedermann, Sollfrank, and Heinz) fits. At different fixed values of the flow profile parameter n. Data from top 10% centrality and $|y| < 0.1$ were used.

experiment	model	$\sqrt{s_{\mathrm{NN}}}$ (GeV)	T_{kin} (MeV)	$\langle\beta_T\rangle$	reference
FOPI	SR	1.94	17.2 ± 3.4	0.204 ± 0.011	[210]
EOS	SR	1.98	31.0 ± 8.5	0.19 ± 0.03	[211]
FOPI	SR	1.98	26.2 ± 5.1	0.263 ± 0.014	[210]
FOPI	SR	2.05	36.7 ± 7.5	0.334 ± 0.017	[210]
EOS	SR	2.05	55.0 ± 26.5	0.22 ± 0.07	[211]
EOS	SR	2.14	59.0 ± 15.5	0.26 ± 0.04	[211]
EOS	SR	2.23	69.0 ± 17.5	0.30 ± 0.04	[211]
FOPI	SR	2.31	80	0.40	[212]
EOS	SR	2.31	83.0 ± 23.5	0.32 ± 0.05	[211]
EOS	SR	2.37	94.0 ± 22.0	0.32 ± 0.04	[211]
E866	SSH	4.8	127^{+10}_{-15}	0.39 ± 0.05	[213]
NA44	SSH	17.3	140	0.4	[214]
NA49	—	17.3	120 ± 12	0.55 ± 0.12	[215]
STAR	SR	19.6	98.1 ± 0.7	0.615 ± 0.004	(this work)
STAR	SSH	19.6	100.4 ± 1.1	0.50 ± 0.02	(this work)
STAR	—	130 (minbias)	101 ± 24	0.54 ± 0.05	[85]
PHENIX	SSH	130	121 ± 4	—	[207]
STAR	SSH	200	89 ± 10	0.59 ± 0.05	[18]
PHENIX	SSH	200	110 ± 23	—	[206, 207]
BRAHMS	SSH	200 (top 5%)	127 ± 2	0.57 ± 0.01	[216]
BRAHMS	SSH	200 (top 10%)	119 ± 1	0.626 ± 0.005	[217]

Table C.20. Collected data on kinetic freeze-out temperatures and average collective radial flow velocities (including those not in Fig. 6.34) from various experiments. Studies have used different approaches in getting the flow velocity and the freeze-out temperature. We indicate the Siemens and Rasmussen approach by SR, and the Schnedermann, Sollfrank, and Heinz blast wave moel by SSH.

Appendix D

Energy Loss Correction

Particles lose their energy when they traverse detector gas and material. For example, a proton with $p_T = 300$ MeV/c would be detected as a 280 MeV/c proton. Monte Carlo simulations can be used to estimate this energy loss effect, which will depend on particle charge and velocity, as well as type of material. In the raw data, default correction has been done by assuming the pion mass. Further corrections are needed for kaons, protons, and antiprotons. Unlike other corrections discussed in this study, where the change is in the invariant yield in each transverse mass bin, the energy loss correction shifts horizontally the transverse mass centroids.

Since the correction is based on geometry, we can estimate this correction from a previous STAR study (in this case, the 130 GeV study [30]).

The corrections were done at the top level as dE/dx histograms were created. The p_T values were corrected using the calculated dp_T with the 130 GeV parameters. dp_T is calculated as a function of p_T as

$$dp_T = -\frac{a}{\beta^b} \tag{D.1}$$

where β is the velocity; a and b are the fit parameters. For kaons, $a = 0.00128$ and $b = 2.31$. For protons and antiprotons, $a = 0.00145$ and $b = 2.31$.

The comparisons between the histograms are shown in Figures D.1, D.2, D.3, and

D.4. First, note the regions of interest in these figures. For the kaon mass assumption, we only compare the kaon peaks (second from right). For a proton assumption, only the rightmost peaks are relevant. Consider the $m_T - m_0$ region where the spectra begin, which is $m_T - m_0 = 0.0625$ GeV/c^2 for kaons and protons. The differences are barely noticeable within the errors. Therefore, corrections were considered small and were not applied to the data.

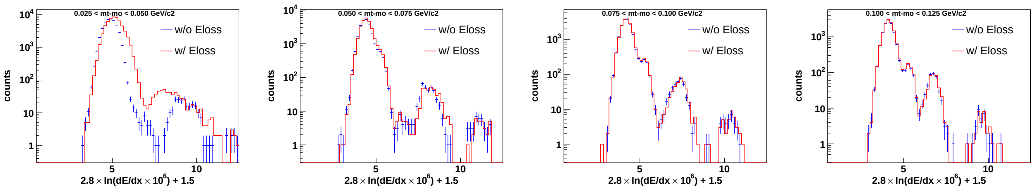

Figure D.1. Comparisons between current dE/dx distributions (blue) and ones with energy loss corrections (red), for negative kaons and protons at midrapidity ($|y| < 0.1$) from top 10% central events. Four figures represent four consecutive evenly-divided $m_T - m_0$ regions, from 0.0375 to 0.1125 GeV/c^2.

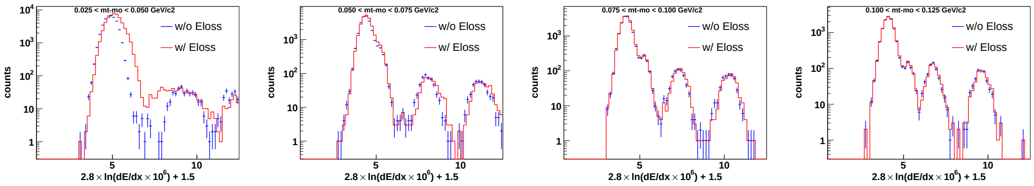

Figure D.2. Comparisons between current dE/dx distributions (blue) and ones with energy loss corrections (red), for positive kaons at midrapidity ($|y| < 0.1$) from top 10% central events. Four figures represent four consecutive evenly-divided $m_T - m_0$ regions, from 0.0375 to 0.1125 GeV/c^2.

Then the histograms were refitted using re-calibrated dE/dx values as a function of $\beta\gamma$. Finally, the yields were extracted and compared with the yields before the correction. The final spectra obtained from this method are found to be qualitatively the same as the spectra used in this analysis (Figure D.5).

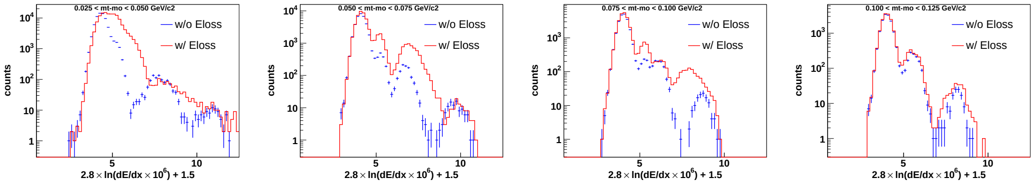

Figure D.3. Comparisons between current dE/dx distributions (blue) and ones with energy loss corrections (red), for antiprotons at midrapidity ($|y| < 0.1$) from top 10% central events. Four figures represent four consecutive $m_T - m_0$ regions, from 0.0375 to 0.1125 GeV/c^2.

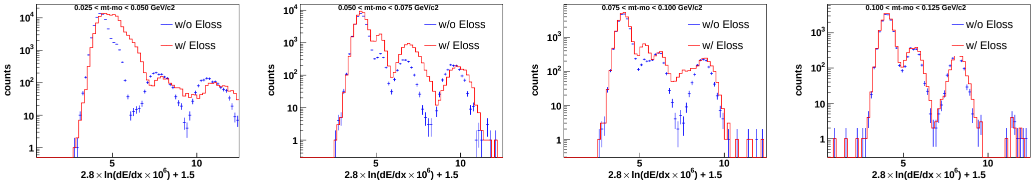

Figure D.4. Comparisons between current dE/dx distributions (blue) and ones with energy loss corrections (red), for protons at midrapidity ($|y| < 0.1$) from top 10% central events. Four figures represent four consecutive $m_T - m_0$ regions, from 0.0375 to 0.1125 GeV/c^2.

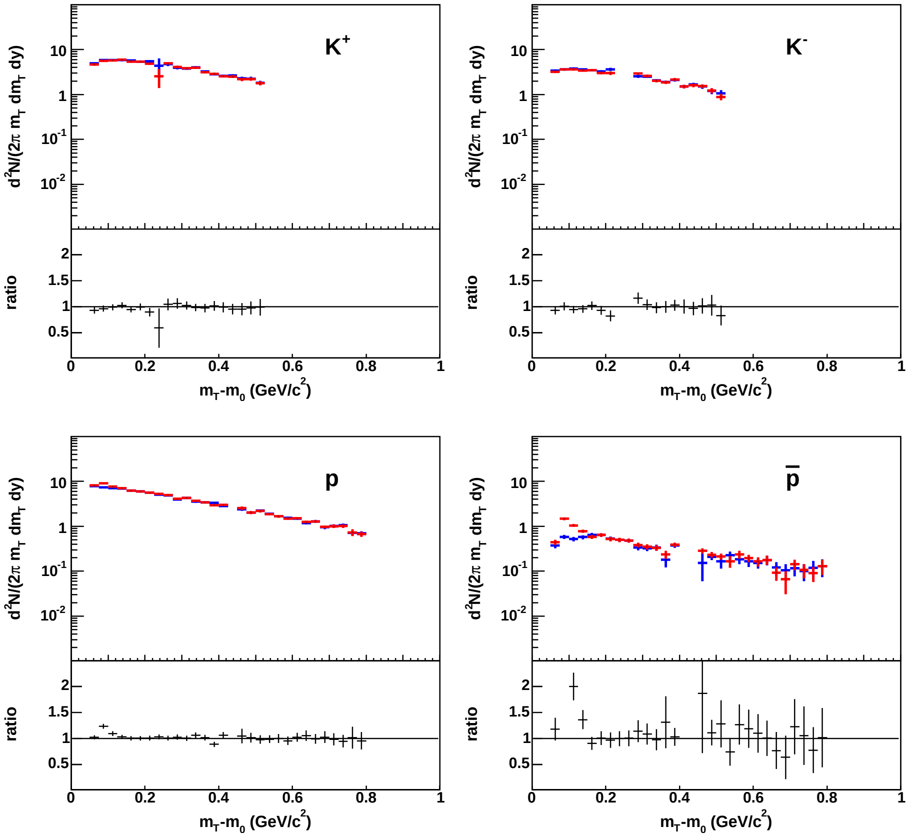

Figure D.5. Spectra comparisons between the one with (red) and without (blue) energy loss correction, for four particle species at midrapidity ($|y| < 0.1$) from most central collisions. The ratios of (with)/(without) are also shown The ratio = 1 line is drawn for reference.

Appendix E

Glauber Model of Nuclear Collisions

The Glauber model is a geometrical model which calculates nucleus-nucleus cross section based on a nuclear density profile and the nucleon-nucleon inelastic cross section, $\sigma_{\mathrm{NN}}^{\mathrm{inel}}$. The model, which can be applied to heavy ion collisions over a wide range of energy, allows the determination of centrality based on number of binary collisions and/or number of participants.

The Woods-Saxon nuclear density gives the density of the nucleus at distance r from the center,

$$\rho(r) = \frac{\rho_0}{1 + \exp((r - r_0)/c)} \tag{E.1}$$

where ρ_0 is the density parameter in nucleons/fm^3, r_0 the radius parameter, and c the surface thickness (fuzziness). Typical parameter values, as used in [30], are $c = 0.535 \pm 0.027$ fm, $r_0 = 6.5 \pm 0.1$, and ρ_0 is normalized to 0.16052 to gives $\int d^3r\, \rho(r) = 197$ for Au.

The nuclear thickness function at distance s from the center, in the unit of nucleons per fm^2,

$$T_A(\vec{s}) = \int dz\, \rho(r) \tag{E.2}$$

where $\vec{s}$ is a vector perpendicular to the beam axis ($\hat{z}$) and along the impact parameter direction (center of one nucleus to the other). The magnitude $r = \sqrt{s^2 + z^2}$

The nuclear overlap function between two nuclei at impact parameter b,

$$T_{AB}(\vec{b}) = \int d^2s\, T_A(\vec{s}) T_{AB}(\vec{s} - \vec{b}) \tag{E.3}$$

From T_A and T_{AB} we can calculate the number of participating nucleons (N_{part}) and the number of binary collisions (N_{coll}).

$$N_{\text{part}}(\vec{b}) = \int d^2s \left(T_A(\vec{s}) \left[1 - e^{-\sigma_{\text{NN}} T_B(\vec{s}-\vec{b})}\right] + T_B(\vec{s} - \vec{b}) \left[1 - e^{-\sigma_{\text{NN}} T_A(\vec{s})}\right] \right) \tag{E.4}$$

$$N_{\text{coll}}(\vec{b}) = \sigma_{\text{NN}} T_{AB}(\vec{b}) \tag{E.5}$$

For a value of $\sigma_{\text{NN}}^{\text{inel}} \sim \sigma_{\text{pp}} \approx 32$ mb [43], we obtain N_{part} and N_{coll} as functions of impact parameter, shown in Figure E.1.

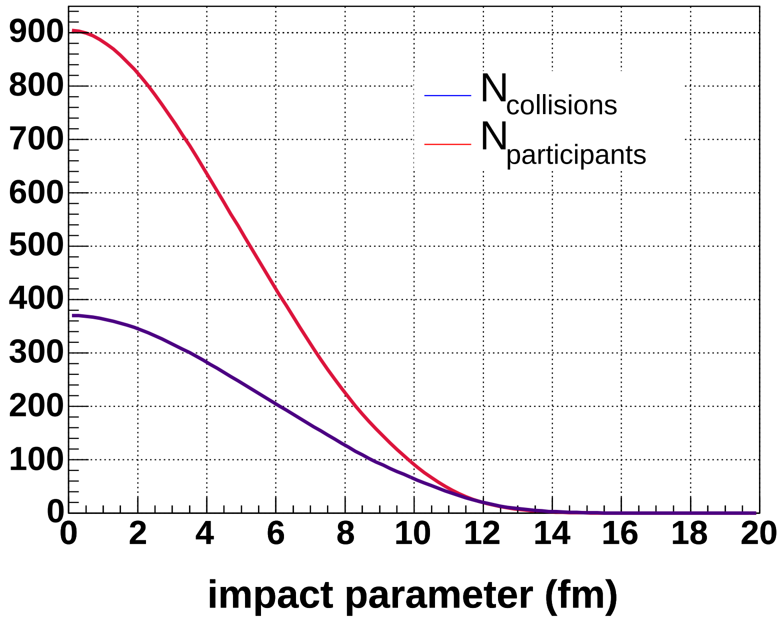

Figure E.1. The numbers of participants and binary collisions as functions of the impact parameter from the Glauber model calculation.

To relate N_{part} and N_{coll} to centrality, we have to calculate the cross section σ at random b and plot this $d\sigma/db$ distribution. The area under the distribution curve will give the number of events. A region of σ which corresponds to the top 10% centrality, for example, means that 10% of the events fall under such region. Then from the impact parameter b we can calculate the numbers of participants and binary collisions.

Appendix F

Bessel Functions

Some of the Bessel functions are used in describing physical measurements such as transverse mass spectra and particle density. They also play important roles in physics problems involving cylindrical or spherical symmetry. Here we look at their mathematical definitions [218].

The Bessel functions are the solutions of the Bessel's differential equation, which is one of the special cases of the Sturm-Liouville boundary value problem. The general Sturm-Liouville differential equation has the form

$$\frac{d}{dx}\left(r(x)\frac{dy(x)}{dx}\right) + (q(x) + \lambda p(x))y(x) = 0 \tag{F.1}$$

defined in a given interval $x \in [a, b]$. The boundary values, $y(a)$, $y'(a)$, $y(b)$, and $y'(b)$, are specified.

For $a = 0$, $b = \infty$, $r(x) = p(x) = x$, $q(x) = \dfrac{x^2 - n^2x^2 - n^2}{x}$, and $\lambda = n$, the Sturm-Liouville equation becomes the Bessel's differential equation

$$x^2\frac{d^2y}{dx^2} + x\frac{dy}{dx} + (x^2 - n^2)y = 0 \tag{F.2}$$

Bessel functions are the solutions (y) to the equation. The order of the solution is n, which is a constant but not necessarily an integer. The solution can be written as a linear combination of two independent functions: $y_n(x) = aJ_n(x) + bY_n(x)$, where a and b are arbitrary constants. $J_n(x)$ and $Y_n(x)$, defined as infinite series in equations (F.3) and (F.4), are called the Bessel functions of the first and second kinds, respectively.

$$\begin{aligned} J_n(x) &= x^n \sum_{m=0}^{\infty} \frac{(-1)^m x^{2m}}{m!(m+n)!} && \text{(F.3)} \\ Y_n(x) &= \frac{\cos(\pi n) J_n(x) - J_{-n}(x)}{\sin(\pi n)} && \text{(F.4)} \end{aligned}$$

If we have instead

$$x^2 \frac{d^2y}{dx^2} + x\frac{dy}{dx} - (x^2 + n^2)y = 0 \tag{F.5}$$

the solutions are called the modified Bessel functions, and can be written as $y_n(x) = aI_n(x) + bK_n(x)$.

$I_n(x)$ is the modified Bessel function of the first kind. It is defined in terms of $J_n(x)$ as

$$I_n(x) = i^{-n} J_n(ix) \tag{F.6}$$

$K_n(x)$ is the modified Bessel function of the second kind. It is defined as

$$\begin{aligned} K_n(x) &= \frac{\pi}{2}\left(\frac{I_{-n}(x) - I_n(x)}{\sin(n\pi)}\right) && \text{(F.7)} \\ &= \frac{\pi}{2} i^{n+1}(J_n(ix) + iY_n(ix)) && \text{(F.8)} \end{aligned}$$

The plots of $I_n(x)$ and K_n vs. x are shown in Fig. F.1

We use $I_0(x)$ and $K_1(x)$ in the blast wave formula (equation (6.37)) and $K_2(x)$ in the statistical model (equation (6.31)) to extract chemical freeze out parameters.

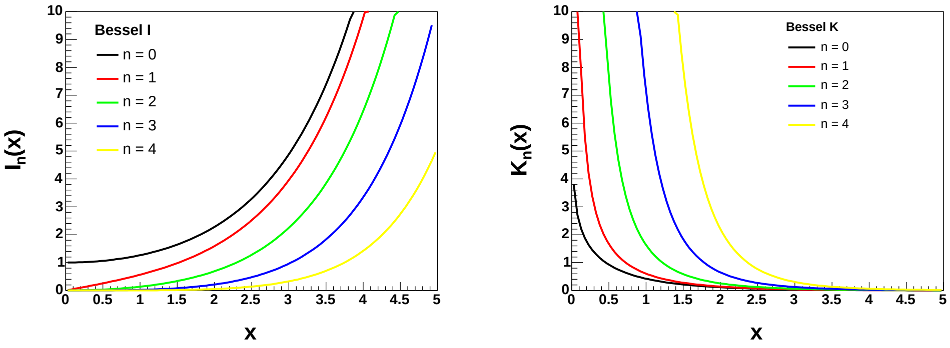

Figure F.1. Modified Bessel functions of the first and second kinds.

Bibliography

[1] V. V. Ezhela, S. B. Lugovsky and O. V. Zenin, hep-ph/0312114.

[2] S. Bethke, Nucl. Phys. Proc. Suppl. **121**, 74 (2003), [hep-ex/0211012].

[3] P. Braun-Munzinger, Nucl. Phys. **A681**, 119 (2001), [nucl-ex/0007021].

[4] H. Hahn *et al.*, Nucl. Instrum. Meth. **A499**, 245 (2003).

[5] H. S. Matis *et al.*, Nucl. Instrum. Meth. **A499**, 802 (2003), [nucl-ex/0205008].

[6] STAR, K. H. Ackermann *et al.*, Nucl. Instrum. Meth. **A499**, 624 (2003).

[7] M. Anderson *et al.*, Nucl. Instrum. Meth. **A499**, 659 (2003), [nucl-ex/0301015].

[8] STAR, H. J. Crawford *et al.*, Nucl. Instrum. Meth. **A499**, 766 (2003).

[9] C. Adler *et al.*, Nucl. Instrum. Meth. **A470**, 488 (2001), [nucl-ex/0008005].

[10] WA98, L. Rosselet *et al.*, Nucl. Phys. **A698**, 647 (2002).

[11] NA44, I. G. Bearden *et al.*, Phys. Rev. **C66**, 044907 (2002), [nucl-ex/0202019].

[12] E866, L. Ahle *et al.*, Phys. Lett. **B490**, 53 (2000), [nucl-ex/0008010].

[13] NA49, S. V. Afanasiev *et al.*, Phys. Rev. **C66**, 054902 (2002), [nucl-ex/0205002].

[14] PHENIX, S. S. Adler *et al.*, Phys. Rev. **C69**, 034909 (2004), [nucl-ex/0307022].

[15] STAR, C. Adler *et al.*, Phys. Lett. **B595**, 143 (2004), [nucl-ex/0206008].

[16] STAR, C. Adler *et al.*, Phys. Rev. Lett. **86**, 4778 (2001), [nucl-ex/0104022].

[17] STAR, J. Adams *et al.*, Phys. Lett. **B567**, 167 (2003), [nucl-ex/0211024].

[18] STAR, J. Adams *et al.*, Phys. Rev. Lett. **92**, 112301 (2003), [nucl-ex/0310004].

[19] E866, L. Ahle *et al.*, Phys. Lett. **B476**, 1 (2000), [nucl-ex/9910008].

[20] E895, J. L. Klay *et al.*, Phys. Rev. **C68**, 054905 (2003), [nucl-ex/0306033].

[21] E802, L. Ahle *et al.*, Phys. Rev. **C58**, 3523 (1998).

[22] PHENIX, K. Adcox *et al.*, Phys. Rev. Lett. **88**, 242301 (2002), [nucl-ex/0112006].

[23] E802, C. Muentz, Acta Phys. Polon. **B29**, 3253 (1998), [nucl-ex/9807001].

[24] A. Wagner *et al.*, Phys. Lett. **B420**, 20 (1998), [nucl-ex/9712004].

[25] PHOBOS, B. B. Back *et al.*, Phys. Rev. Lett. **85**, 3100 (2000), [hep-ex/0007036].

[26] PHOBOS, B. B. Back *et al.*, Phys. Rev. Lett. **88**, 022302 (2002), [nucl-ex/0108009].

[27] PHOBOS, P. A. Steinberg *et al.*, Nucl. Phys. **A715**, 490 (2003), [nucl-ex/0211002].

[28] PHENIX, K. Adcox *et al.*, Phys. Rev. Lett. **86**, 3500 (2001), [nucl-ex/0012008].

[29] STAR, C. Adler *et al.*, Phys. Rev. Lett. **87**, 112303 (2001), [nucl-ex/0106004].

[30] STAR, J. Adams *et al.*, nucl-ex/0311017.

[31] D. Kharzeev, E. Levin and M. Nardi, hep-ph/0111315.

[32] CDF, F. Abe *et al.*, Phys. Rev. **D41**, 2330 (1990).

[33] UA5, G. J. Alner *et al.*, Phys. Rept. **154**, 247 (1987).

[34] W. Fischer, Run overview at the Relativistic Heavy Ion Collider, `http://www.agsrhichome.bnl.gov/RHIC/Runs/`.

[35] STAR, R. Bellwied *et al.*, Nucl. Instrum. Meth. **A499**, 640 (2003).

[36] I. Sick, Phys. Lett. **B576**, 62 (2003), [nucl-ex/0310008].

[37] M. S. Dewey *et al.*, Phys. Rev. Lett. **91**, 152302 (2003), [nucl-ex/0311006].

[38] G. Zweig, (1981), In *Lichtenberg, D. B. (Ed.), Rosen, S. P. (Ed.): Developments In The Quark Theory Of Hadrons, Vol. 1*, 22-101 and CERN Geneva - TH. 401.

[39] G. Zweig, (1964), CERN-TH-412.

[40] C. Y. Wong, *Introduction to High-Energy Heavy-Ion Collisions* (World Scientific, Singapore, 1994).

[41] S. Weinberg, Eur. Phys. J. **C34**, 5 (2004), [hep-ph/0401010].

[42] S. Weinberg, Phys. Rev. Lett. **19**, 1264 (1967).

[43] Particle Data Group, S. Eidelman *et al.*, Phys. Lett. **B592**, 1 (2004).

[44] D. Griffiths, *Introduction to Elementary Particles* (John Wiley & Sons, Inc., 1987).

[45] R. K. Ellis, W. J. Stirling and B. R. Webber, *QCD and Collider Physics* (Cambridge University Press, Cambridge, 1996).

[46] S. Bethke, J. Phys. **G26**, R27 (2000), [hep-ex/0004021].

[47] T. van Ritbergen, J. A. M. Vermaseren and S. A. Larin, Phys. Lett. **B400**, 379 (1997), [hep-ph/9701390].

[48] J. C. Collins, hep-ph/9510276, Lectures given at Theoretical Advanced Study Institute in Elementary Particle Physics (TASI 95): QCD and Beyond, Boulder, CO, 4-30 Jun 1995.

[49] H. D. Politzer, Phys. Rept. **14**, 129 (1974).

[50] D. J. Gross and F. Wilczek, Phys. Rev. Lett. **30**, 1343 (1973).

[51] F. Karsch, Lect. Notes Phys. **583**, 209 (2002), [hep-lat/0106019].

[52] F. Karsch, E. Laermann and A. Peikert, Phys. Lett. **B478**, 447 (2000), [hep-lat/0002003].

[53] F. Karsch, Nucl. Phys. **A698**, 199 (2002), [hep-ph/0103314].

[54] STAR, J. Adams *et al.*, nucl-ex/0501009.

[55] D. Diakonov, hep-ph/9802298, Lectures given at Advanced Summer School on Nonperturbative Quantum Field Physics, Peniscola, Spain, 2-6 Jun 1997.

[56] B. R. Holstein, hep-ph/9510344, Lectures given at 7th Summer School in Nuclear Physics Symmetries, Seattle, WA, 18-30 Jun 1995.

[57] J. Chadwick, Nature **129**, 312 (1932).

[58] S. A. Bonometto and O. Pantano, Phys. Rept. **228**, 175 (1993).

[59] H. Satz, Nucl. Phys. **A715**, 3 (2003), [hep-ph/0209181].

[60] P. Huovinen, nucl-th/0305064, In *Hwa, R.C. (ed.) et al.: Quark gluon plasma* 600-633.

[61] STAR, J. Adams *et al.*, Phys. Rev. Lett. **92**, 182301 (2004), [nucl-ex/0307024].

[62] STAR, C. Adler *et al.*, Phys. Rev. Lett. **89**, 092301 (2002), [nucl-ex/0203016].

[63] J. I. Kapusta and A. Mekjian, Phys. Rev. **D33**, 1304 (1986).

[64] X. N. Wang and M. Gyulassy, Phys. Rev. Lett. **68**, 1480 (1992).

[65] STAR, C. Adler *et al.*, Phys. Rev. Lett. **89**, 202301 (2002), [nucl-ex/0206011].

[66] STAR, J. Adams *et al.*, Phys. Rev. Lett. **91**, 172302 (2003), [nucl-ex/0305015].

[67] PHENIX, K. Adcox *et al.*, Phys. Rev. Lett. **88**, 022301 (2002), [nucl-ex/0109003].

[68] PHENIX, S. S. Adler *et al.*, Phys. Rev. Lett. **91**, 072301 (2003), [nucl-ex/0304022].

[69] D. d'Enterria, Phys. Lett. **B596**, 32 (2004), [nucl-ex/0403055].

[70] M. Gyulassy and M. Plumer, Phys. Lett. **B243**, 432 (1990).

[71] STAR, C. Adler *et al.*, Phys. Rev. Lett. **90**, 082302 (2003), [nucl-ex/0210033].

[72] STAR, F. Wang, J. Phys. **G30**, S1299 (2004), [nucl-ex/0404010].

[73] STAR, A. H. Tang, J. Phys. **G30**, S1235 (2004), [nucl-ex/0403018].

[74] L. L. Frankfurt and M. I. Strikman, Phys. Rept. **160**, 235 (1988).

[75] A. H. Mueller, Nucl. Phys. **B335**, 115 (1990).

[76] S. R. Klein and R. Vogt, Phys. Rev. **C67**, 047901 (2003), [nucl-th/0211066].

[77] STAR, J. Adams *et al.*, Phys. Rev. Lett. **91**, 072304 (2003), [nucl-ex/0306024].

[78] PHOBOS, B. B. Back *et al.*, Phys. Rev. Lett. **91**, 072302 (2003), [nucl-ex/0306025].

[79] PHENIX, S. S. Adler *et al.*, Phys. Rev. Lett. **91**, 072303 (2003), [nucl-ex/0306021].

[80] BRAHMS, I. Arsene *et al.*, Phys. Rev. Lett. **91**, 072305 (2003), [nucl-ex/0307003].

[81] J. Y. Ollitrault, Phys. Rev. **D46**, 229 (1992).

[82] H. Sorge, Phys. Rev. Lett. **78**, 2309 (1997), [nucl-th/9610026].

[83] H. Sorge, Phys. Lett. **B402**, 251 (1997), [nucl-th/9701012].

[84] STAR, K. H. Ackermann *et al.*, Phys. Rev. Lett. **86**, 402 (2001), [nucl-ex/0009011].

[85] STAR, C. Adler *et al.*, Phys. Rev. Lett. **87**, 182301 (2001), [nucl-ex/0107003].

[86] STAR, C. Adler *et al.*, Phys. Rev. **C66**, 034904 (2002), [nucl-ex/0206001].

[87] STAR, C. Adler *et al.*, Phys. Rev. Lett. **90**, 032301 (2003), [nucl-ex/0206006].

[88] STAR, J. Adams *et al.*, Phys. Rev. Lett. **92**, 052302 (2004), [nucl-ex/0306007].

[89] STAR, J. Castillo, J. Phys. **G30**, S1207 (2004), [nucl-ex/0403027].

[90] M. Kaneta, J. Phys. **G30**, S1217 (2004), [nucl-ex/0404014].

[91] E. Shuryak, J. Phys. **G30**, S1221 (2004).

[92] R. Vogt, Heavy Ion Phys. **18**, 11 (2003), [hep-ph/0205330].

[93] M. Gyulassy and X. N. Wang, Nucl. Phys. **B420**, 583 (1994), [nucl-th/9306003].

[94] U. A. Wiedemann, Nucl. Phys. **B588**, 303 (2000), [hep-ph/0005129].

[95] M. Gao, Phys. Rev. **D41**, 626 (1990).

[96] H. Satz, Nucl. Phys. **A418**, 447c (1984).

[97] T. Matsui and H. Satz, Phys. Lett. **B178**, 416 (1986).

[98] S. Kelly, J. Phys. **G30**, S1189 (2004), [nucl-ex/0403057].

[99] L. J. Ruan, J. Phys. **G30**, S1197 (2004), [nucl-ex/0403054].

[100] PHENIX, R. G. de Cassagnac, J. Phys. **G30**, S1341 (2004), [nucl-ex/0403030].

[101] A. A. P. Suaide, J. Phys. **G30**, S1179 (2004), [nucl-ex/0404019].

[102] PHENIX, S. S. Adler *et al.*, Phys. Rev. **C69**, 014901 (2004), [nucl-ex/0305030].

[103] PHENIX, S. S. Adler, Phys. Rev. Lett. **94**, 082301 (2005), [nucl-ex/0409028].

[104] V. Greco, C. M. Ko and R. Rapp, Phys. Lett. **B595**, 202 (2003), [nucl-th/0312100].

[105] PHENIX, J. Frantz, J. Phys. **G30**, S1003 (2004), [nucl-ex/0404006].

[106] X. N. Wang and Z. Huang, Phys. Rev. **C55**, 3047 (1997), [hep-ph/9701227].

[107] M. Harrison, T. Ludlam and S. Ozaki, Nucl. Instrum. Meth. **A499**, 235 (2003).

[108] G. Bunce, N. Saito, J. Soffer and W. Vogelsang, Ann. Rev. Nucl. Part. Sci. **50**, 525 (2000), [hep-ph/0007218].

[109] W. Vogelsang, Pramana **63**, 1251 (2004), [hep-ph/0405069].

[110] L. C. Bland, AIP Conf. Proc. **675**, 98 (2003), [hep-ex/0212013].

[111] M. Stratmann, hep-ph/0211317.

[112] CRC Handbook of Chemistry and Physics, `http://www.hbcpnetbase.com/`, 2004, Online edition.

[113] J. Benjamin *et al.*, Prepared for IEEE Particle Accelerator Conference (PAC99), New York, New York, 29 Mar - 2 Apr 1999.

[114] L. Ahrens *et al.*, Presented at IEEE Particle Accelerator Conference (PAC2001), Chicago, Illinois, 18-22 Jun 2001.

[115] E. D. Courant and H. S. Snyder, Ann. Phys. **3**, 1 (1958).

[116] M. Anerella *et al.*, Nucl. Instrum. Meth. **A499**, 280 (2003).

[117] L. Ahrens, J. L. Mi and W. Zhang, Prepared for 8th European Particle Accelerator Conference (EPAC 2002), Paris, France, 3-7 Jun 2002.

[118] R. Fernow, *Introduction to Experimental Particle Physics* (Cambridge University Press, Cambridge, 1986).

[119] BRAHMS, M. Adamczyk *et al.*, Nucl. Instrum. Meth. **A499**, 437 (2003).

[120] PHOBOS, B. B. Back *et al.*, Nucl. Instrum. Meth. **A499**, 603 (2003).

[121] PHENIX, K. Adcox *et al.*, Nucl. Instrum. Meth. **A499**, 469 (2003).

[122] NA49, H. Appelshauser *et al.*, Eur. Phys. J. **A2**, 383 (1998).

[123] A. Drees, J. Phys. **G30**, S1109 (2004).

[124] J. W. Harris *et al.*, nucl-ex/0407021.

[125] R. G. Milner, AIP Conf. Proc. **698**, 806 (2004).

[126] STAR, H. Matis, STAR coordinate system, `http://www.star.bnl.gov/STAR/sno/sno.html`, 1993, STAR Note C0121.

[127] STAR, F. Bergsma *et al.*, Nucl. Instrum. Meth. **A499**, 633 (2003).

[128] STAR, L. Kochenda *et al.*, Nucl. Instrum. Meth. **A499**, 703 (2003).

[129] M. Anderson *et al.*, Nucl. Instrum. Meth. **A499**, 679 (2003), [nucl-ex/0205014].

[130] STAR, J. M. Landgraf *et al.*, Nucl. Instrum. Meth. **A499**, 762 (2003).

[131] R. Burns *et al.*, Nucl. Instrum. Meth. **A499**, 349 (2003).

[132] STAR, W. B. Christie, Requirements for STAR Global Interlock System, `http://www.star.bnl.gov/STAR/sno/sno.html`, 1999, STAR Note C0351B.

[133] STAR, S. Margetis and D. Cebra, Main vertex reconstruction in STAR, `http://www.star.bnl.gov/STAR/sno/sno.html`, 1994, STAR Note 89.

[134] STAR, J. T. Mitchell and I. M. Sakrejda, Tracking for the STAR TPC: Documentation and user's guide, `http://www.star.bnl.gov/STAR/sno/sno.html`, 1995, STAR Note 190.

[135] STAR, D. Hardtke, Nucl. Phys. **A698**, 671 (2002), [nucl-ex/0104007].

[136] J. S. Lange *et al.*, Nucl. Instrum. Meth. **A453**, 397 (2000).

[137] STAR, J. Abele *et al.*, Nucl. Instrum. Meth. **A499**, 692 (2003).

[138] H. Fanchiotti, C. A. G. Canal and M. D. Marucho, hep-ph/0305310.

[139] STAR, A. Tang, 2000, private communication.

[140] STAR, O. Barannikova, 2002, private communication.

[141] STAR, K. Schweda, 2002, private communication.

[142] H1, D. Ozerov, Acta Phys. Polon. **B33**, 3293 (2002), [hep-ph/0207048].

[143] K. S. Krane, *Introductory Nuclear Physics* (John Wiley & Sons, Inc., 1988).

[144] W. Busza and A. S. Goldhaber, Phys. Lett. **B139**, 235 (1984).

[145] NA49, H. Appelshauser *et al.*, Phys. Rev. Lett. **82**, 2471 (1999), [nucl-ex/9810014].

[146] E. Wang and X. N. Wang, Phys. Rev. **C64**, 034901 (2001), [nucl-th/0104031].

[147] STAR, R. Witt, nucl-ex/0403021, Poster paper presented at 17th International Conference on Ultra Relativistic Nucleus-Nucleus Collisions (Quark Matter 2004), Oakland, California, 11-17 Jan 2004.

[148] NA44, I. G. Bearden *et al.*, Phys. Lett. **B388**, 431 (1996).

[149] NA49, M. van Leeuwen, 2002, private communication.

[150] NA49, G. E. Cooper, Nucl. Phys. **A661**, 362 (1999).

[151] NA49, G. I. Veres, Nucl. Phys. **A661**, 383 (1999).

[152] J. D. Bjorken, Phys. Rev. **D27**, 140 (1983).

[153] J. Zimanyi, T. S. Biro, T. Csorgo and P. Levai, hep-ph/9904501.

[154] A. Bialas, Phys. Lett. **B442**, 449 (1998), [hep-ph/9808434].

[155] F. Wang, Phys. Lett. **B489**, 273 (2000), [nucl-ex/9911004].

[156] E802, L. Ahle *et al.*, Phys. Rev. **C60**, 044904 (1999), [nucl-ex/9903009].

[157] C. L. Kunz, *Charged kaon ratios and yields measured with the STAR detector at the Relativistic Heavy Ion Collider*, PhD thesis, Carnegie Mellon University, 2003.

[158] A. M. Rossi *et al.*, Nucl. Phys. **B84**, 269 (1975).

[159] S. Soff *et al.*, Phys. Lett. **B471**, 89 (1999), [nucl-th/9907026].

[160] J. Rafelski and B. Müller, Phys. Rev. Lett. **48**, 1066 (1982).

[161] H. C. Eggers and J. Rafelski, Int. J. Mod. Phys. **A6**, 1067 (1991).

[162] STAR, O. Barannikova and F. Wang, Nucl. Phys. **A715**, 458 (2003), [nucl-ex/0210034].

[163] T. Alexopoulos *et al.*, Phys. Rev. Lett. **64**, 991 (1990).

[164] BRAHMS, I. G. Bearden *et al.*, Phys. Rev. Lett. **90**, 102301 (2003).

[165] P. Braun-Munzinger, J. Cleymans, H. Oeschler and K. Redlich, Nucl. Phys. **A697**, 902 (2002), [hep-ph/0106066].

[166] S. A. Bass *et al.*, Prog. Part. Nucl. Phys. **41**, 225 (1998), [nucl-th/9803035].

[167] M. Bleicher *et al.*, J. Phys. **G25**, 1859 (1999), [hep-ph/9909407].

[168] F. Wang, H. Liu, H. Sorge, N. Xu and J. Yang, Phys. Rev. **C61**, 064904 (2000), [nucl-th/9909001].

[169] E. L. Bratkovskaya *et al.*, Prog. Part. Nucl. Phys. **53**, 225 (2004), [nucl-th/0312048].

[170] NA49, M. Gazdzicki *et al.*, J. Phys. **G30**, S701 (2004), [nucl-ex/0403023].

[171] E. L. Bratkovskaya *et al.*, Phys. Rev. **C69**, 054907 (2004), [nucl-th/0402026].

[172] E. L. Bratkovskaya *et al.*, nucl-th/0401031, Invited talk at NATO Advanced Study Institute: Structure and Dynamics of Elementary Matter, Kemer, Turkey, 22 Sep - 2 Oct 2003.

[173] M. Gazdzicki and M. I. Gorenstein, Acta Phys. Polon. **B30**, 2705 (1999), [hep-ph/9803462].

[174] R. Stock, Phys. Rept. **135**, 259 (1986).

[175] NA44, H. Bøggild *et al.*, Phys. Lett. **B372**, 339 (1996).

[176] J. W. Harris *et al.*, Phys. Rev. **C41**, 147 (1990).

[177] B. Li, Phys. Lett. **B346**, 5 (1995), [nucl-th/9501001].

[178] H. W. Barz, J. P. Bondorf, J. J. Gaardhoje and H. Heiselberg, Phys. Rev. **C57**, 2536 (1998), [nucl-th/9711064].

[179] E895, D. Cebra *et al.*, Coulomb effect in Au+Au collisions at 2-8 AGeV, paper in preparation, 2003.

[180] H. Heiselberg, Phys. Rept. **351**, 161 (2001), [nucl-th/0003046].

[181] STAR, D. Cherney, 2004, private communication.

[182] A. H. Mueller and J. W. Qiu, Nucl. Phys. **B268**, 427 (1986).

[183] D. Kharzeev and E. Levin, Phys. Lett. **B523**, 79 (2001), [nucl-th/0108006].

[184] D. E. Soper, Nucl. Phys. Proc. Suppl. **53**, 69 (1997), [hep-lat/9609018].

[185] P. Braun-Munzinger, I. Heppe and J. Stachel, Phys. Lett. **B465**, 15 (1999), [nucl-th/9903010].

[186] J. Sollfrank, U. Heinz, H. Sorge and N. Xu, Phys. Rev. **C59**, 1637 (1999), [nucl-th/9811011].

[187] J. Cleymans, H. Oeschler and K. Redlich, J. Phys. **G25**, 281 (1999), [nucl-th/9809031].

[188] M. Kaneta and N. Xu, nucl-th/0405068, A write-up of a poster presented in the 17th International Conference on Ultra Relativistic Nucleus-Nucleus Collisions (Quark Matter 2004), Oakland, California, 11-17 Jan 2004.

[189] J. Rafelski, Phys. Lett. **B262**, 333 (1991).

[190] J. Sollfrank, J. Phys. **G23**, 1903 (1997), [nucl-th/9707020].

[191] J. Cleymans, D. Elliott, A. Keranen and E. Suhonen, Phys. Rev. **C57**, 3319 (1998), [nucl-th/9711066].

[192] J. Cleymans and K. Redlich, Phys. Rev. Lett. **81**, 5284 (1998), [nucl-th/9808030].

[193] K. Redlich, hep-ph/0406250, Talk given at International Workshop on Hot and Dense Matter in Relativistic Heavy Ion Collisions (BP 2004), Budapest, Hungary, 24-27 Mar 2004.

[194] P. B.-M. J. Stachel, J. Phys. **G28**, 1971 (2002), [nucl-th/0112051].

[195] F. Becattini, A. Giovannini and S. Lupia, Z. Phys. **C72**, 491 (1996), [hep-ph/9511203].

[196] F. Becattini and U. W. Heinz, Z. Phys. **C76**, 269 (1997), [hep-ph/9702274].

[197] V. Koch, Nucl. Phys. **A715**, 108 (2003), [nucl-th/0210070].

[198] F. Becattini, hep-ph/0410403, Prepared for International Workshop on Particle Multiplicity in Relativistic Heavy Ion Collisions, Bari, Italy, 17-19 Jun 2004.

[199] B. Tomasik and U. A. Wiedemann, Phys. Rev. **C68**, 034905 (2003), [nucl-th/0207074].

[200] P. J. Siemens and J. O. Rasmussen, Phys. Rev. Lett. **42**, 880 (1979).

[201] E. Schnedermann, J. Sollfrank and U. Heinz, Phys. Rev. **C48**, 2462 (1993), [nucl-th/9307020].

[202] NA35, J. Baechler *et al.*, Phys. Rev. Lett. **72**, 1419 (1994).

[203] E. Schnedermann and U. W. Heinz, Phys. Rev. **C47**, 1738 (1993).

[204] P. F. Kolb and U. Heinz, nucl-th/0305084, In *Hwa, R.C. (ed.) et al.: Quark gluon plasma* 634-714.

[205] E. Schnedermann and U. W. Heinz, Phys. Rev. **C50**, 1675 (1994), [nucl-th/9402018].

[206] PHENIX, T. Chujo, Nucl. Phys. **A715**, 151 (2003), [nucl-ex/0209027].

[207] PHENIX, J. M. Burward-Hoy, Nucl. Phys. **A715**, 498 (2003), [nucl-ex/0210001].

[208] CERES, W. Schmitz *et al.*, J. Phys. **G28**, 1861 (2002), [nucl-ex/0201002].

[209] A. Andronic and P. Braun-Munzinger, hep-ph/0402291, Based on lectures given by P. Braun-Munzinger at the VIII Hispalensis International Summer School, Oromana (Seville, Spain), June 9-21, 2003.

[210] FOPI, W. Reisdorf *et al.*, Nucl. Phys. **A612**, 493 (1997), [nucl-ex/9610009].

[211] EOS, M. A. Lisa *et al.*, Phys. Rev. Lett. **75**, 2662 (1995), [nucl-ex/9502001].

[212] FOPI, N. Herrmann, Nucl. Phys. **A610**, 49c (1996), [nucl-ex/9610007].

[213] E802, C. Muntz, nucl-ex/9806002, Talk given at 25th International Workshop on Gross Properties of Nuclei and Nuclear Excitation: QCD Phase Transitions (Hirschegg 97), Hirschegg, Austria, 13-18 Jan 1997.

[214] NA44, I. G. Bearden *et al.*, Phys. Rev. Lett. **78**, 2080 (1997).

[215] NA49, H. Appelshauser *et al.*, Eur. Phys. J. **C2**, 661 (1998), [hep-ex/9711024].

[216] BRAHMS, R. Debbe, AIP Conf. Proc. **698**, 690 (2004), [nucl-ex/0308004].

[217] BRAHMS, A. Jipa, nucl-ex/0404011, Talk given at 3rd Budapest Winter School on Heavy Ion Physics (RHIC School 2003), Budapest, Hungary, 8-11 Dec 2003.

[218] M. L. Boas, *Mathematical Methods in the Physical Sciences*, Second ed. (John Wiley & Sons, Inc., 1983).